Development and Validation of High-Sensitivity Analytical Frameworks for Low-Abundance Pathological Cargo in Human Biofluids.

By
Jennifer Pollock

B.S. Chemical Engineering, University of California - Santa Barbara, 2022

A dissertation submitted in partial fulfillment of the requirements for the degree of Doctor of Philosophy in Biomedical Engineering at Brown University

PROVIDENCE, RHODE ISLAND

May 24, 2026

This dissertation by Jennifer Pollock is accepted in its present form by Biomedical Engineering program, a joint program in the Division of Biology and Medicine and the School of Engineering is satisfying the dissertation requirement for the degree of Doctor of Philosophy

Date: 04/15/2026

Anubhav Tripathi, Ph.D , Advisor

Recommended to the Graduate Council

Date: 4/15/26

Tejal Desai, Ph.D., Reader

Date: 4/15/26

Jill Kreiling, Ph.D., Reader

Date: 4/15/26

Robert Hurt, Ph.D., Reader

Approved by the Graduate Council

Date: _____

David Lindstrom, Ph.D., Dean of the Graduate School

Abstract of "Development and Validation of High-Sensitivity Analytical Frameworks for Low-Abundance Pathological Cargo in Human Biofluids", by Jennifer Pollock, Ph.D., Brown University, May 2026.

Liquid biopsies offer immense potential for non-invasive disease monitoring, yet their clinical adoption is hindered by the analytical difficulty of detecting scarce biomarkers within complex biofluids. While extracellular vesicles (EVs) and proteopathic aggregates like amyloid-beta (Aβ) provide a window into systemic and central nervous system (CNS) pathologies, traditional isolation-based workflows suffer from low recovery and poor reproducibility. This dissertation describes the development of high-sensitivity analytical frameworks designed to bypass these hurdles through direct, digital quantification of pathological cargo.

The first phase of this research addresses ultra-low-abundance protein monomers. By developing a dual-functionalized microparticle interface—utilizing magnetic capture beads and DNA-tagged detection beads coupled with qPCR amplification—we achieved a femtomolar limit of detection (0.05 pg/mL) for Aβ (1-42). This provides a highly sensitive tool for the early detection of Alzheimer's pathology. Building on this, we established a robust digital Single Molecule Array (SiMoA) platform for the direct detection of intact EVs in human plasma and serum. By implementing a continuous piecewise mathematical model for Average Enzymes per Bead (AEB) determination, we successfully addressed EV polyvalency. This framework maintained a dynamic range over four orders of magnitude and achieved a limit of detection of 1.61×10^7 particles/mL, outperforming commercial assays in both reproducibility and sensitivity.

Finally, we extended this SiMoA framework to neuro-diagnostics to quantify brain-derived EVs (bdEVs). By targeting CNS-specific markers, our findings identified ATP1A3 and NCAM as superior, stable alternatives to L1CAM for longitudinal monitoring. Proteomic characterization revealed that NCAM+ populations exhibit a significantly higher loading density for neurodegenerative biomarkers, such as NfL and GFAP, compared to canonical populations. This suggests that subtype-specific targeting can enhance the resolution of CNS signals in peripheral biofluids. Collectively, this research provides a scalable, high-throughput toolbox that shifts the liquid biopsy paradigm from tedious sample preparation to direct, high-precision molecular profiling. These frameworks offer a standardized path forward for early disease detection and treatment monitoring across oncology and neurology.

Curriculum Vitae

Jennifer Pollock

Education

PhD, Biomedical Engineering August 2022 - May 2026
Brown University, Providence RI

B.S., Chemical Engineering September 2018 - June 2022
University of California - Santa Barbara

Publications

1. Miller J.; **Pollock J**.; Tripathi A. "Synthetic EV Calibrators for the Standardization of EV Quantification Assays" *(In Preparation)*
2. Miller J.; **Pollock J.;** Tripathi A. "Functionalizing Microparticles with Poly-Glutamic Acid to increase Flow Cytometry Sensitivity" *(In Preparation)*
3. **Pollock J.;** Yew, C.; Gutterman-Johns, E.; Miller, J.; Friedbauer, A.; Malyavantham, K.; and Tripathi A. "Ultrasensitive Single Molecular Array Quantification Assays for the Measurement of Brain-Derived Extracellular Vesicles" (*Submitted)*
4. **Pollock J.;** Yew, C.; Gutterman-Johns, E.; Miller, J.; Friedbauer, A.; Malyavantham, K.; and Tripathi A. "The Next Generation of Biomarkers: Direct Detection and Quantification of Extracellular Vesicles in Biofluids" (*Ready For Submission)*
5. **Pollock J.;** Yew, C.; Gutterman-Johns, E.; Miller, J.; Friedbauer, A.; Zhao, M.; Malyavantham, K.; and Tripathi A. "Going Beyond Plasma: Brain-Derived Extracellular Vesicles as Concentrated Carriers of GFAP, NfL, and Amyloid-beta" *(Submitted)*
6. **Pollock J.;** Yew, C.; Tripathi A. "Utilizing Functionalized Dual-Microbead Interfaces for Measurements of Amyloid-beta (1-42) with Femtomolar

Sensitivity" *Langmuir : the ACS journal of surfaces and colloids* vol. 41,9 (2025): 5870-5876. doi:10.1021/acs.langmuir.4c04261

7. H. L. van de Wouw, S.-T. Yen, M. Valet, J. A. Garcia, C. O. Gomez, A. Vian, Y. Liu, **J. Pollock**, P. Pospísil, O. Campa s, E. M. Sletten, Non-Ionic Fluorosurfactants for Droplet-Based in vivo Applications. Angew. Chem. Int. Ed. 63, (2024) https://doi.org/10.1002/anie.202404956
8. Vian, A., Pochitaloff, M., Yen, ST. et al. In situ quantification of osmotic pressure within living embryonic tissues. Nature Commun 14, 7023 (2023). https://doi.org/10.1038/s41467-023-42024-9

Conference Presentations

1. **Pollock J.;** Yew, C.; Gutterman-Johns, E.; Miller, J.; Friedbauer, A.; Malyavantham, K.; and Tripathi A. Ultrasensitive Single Molecular Array Quantification Assays for Brain-Derived Extracellular Vesicles, AD/PD 2026 (Poster Presentation) – March 2026
2. **Pollock J.;** Yew, C.; Gutterman-Johns, E.; Miller, J.; Friedbauer, A.; Malyavantham, K.; and Tripathi A. Characterizing Neuronal-Derived Derived Extracellular Vesicles Using Single Molecular Array Technology, AAIC 2025 (Poster Presentation) – July 2025
3. **Pollock J.;** Yew, C.; Gutterman-Johns, E.; Miller, J.; Friedbauer, A.; Malyavantham, K.; and Tripathi A. Fast Immune Phenotyping of Extracellular Vesicles, PEGS Boston (Oral Presentation) - May 2025
4. **Pollock J.;** Yew, C.; Gutterman-Johns, E.; Miller, J.; Friedbauer, A.; Malyavantham, K.; and Tripathi A. Unlocking The Diagnostic and Therapeutic Potential of Ultrasensitive Extracellular Vesicle and Biomarker Detection Using Single Molecular Detection Assay (SIMOA), AD/PD 2025 (Poster Presentation) - April 2025
5. **Pollock J.;** Yew, C.; Gutterman-Johns, E.; Friedbauer, A.; Malyavantham, K.; and Tripathi A. Methods for Fast Immune Phenotyping of Extracellular Vesicles in Human Biofluids, SLAS 2025 (Oral Presentation) - February 2025
6. **Pollock J.;** Yew, C.; Tripathi A. Development of a micro bead-based immunoassay for the detection of amyloid-beta (1-42), Tri-Con Precision Medicine (Poster Presentation) - March 2024

7. **Pollock J.;** Yew, C.; Tripathi A. Development of functionalized microbead-based immunoassay by qPCR for the detection of amyloid-beta(1-42) monomer in plasma, PEGS Boston (Poster Presentation) - March 2023

Research Experience

Graduate Researcher September 2022 - May 2026
Center for Biomedical Engineering, School of Engineering
Brown University, Providence, RI
Advisor: Professor Anubhav Tripathi, Ph.D.
Skills: qPCR; Microfluidics; Surface Chemistry and Bioconjugation; Proteomics; Genomics; Next Generation Sequencing; Electrophoresis; Thermodynamic and Kinetic Modeling; Microsoft Offices / Google Sheets / Adobe / MATLAB / Python; Specimen Collection and Handling; HIPAA Compliance
Thesis: *Development and Validation of High-Sensitivity Analytical Frameworks for Low-Abundance Pathological Cargo in Human Biofluids.*

- Developed a microbead based immunoassay for the detection of monomeric amyloid-beta (1-42) in human plasma using qPCR readout with atto molar sensitivity.
- Developed and validated Single Molecular Array Assays for detecting and quantifying brain-derived and tumor-derived EVs in biofluids using a wide variety of cell surface markers (CD9, CD63, CD81, NCAM, L1CAM, ATP1A3, EGFR, EpCAM, CD133, and CD44). Positively identified available binding regions on EV surface for GFAP, amyloid-beta, and brain-derived tau in plasma.
- Facilitated interdisciplinary collaborations with multiple professors and clinicians in the School of Biology and Medicine to develop custom assays and analyze patient samples to identify biomarkers associated with poor patient prognosis for glioblastoma and Alzheimer's disease.
- Isolated and characterized changes in CD133, CD44, and EGFR expression on EVs over time: pre and post drug treatment in patient-derived glioblastoma spheroids.

Undergraduate Research Assistant March 2020 - June 2022
Department of Bioengineering
University of California - Santa Barbara, CA
Principal Investigator: Professor Otger Campas, Ph.D.
Skills: Microfluidics; Surface Functionalization; Analytical Chemistry; Encapsulation Science; Animal handling; Confocal Microscopy; Nanoparticle Production

- Supported principal investigators during research developing microdroplet-based mechanical probes for mechanobiology applications. Measured the shear force in regenerating zebra fish tissue.
- Utilized microfluidics to produce double emulsion water-oil-water droplets that were then injected into zebra fish embryos to measure osmotic pressure changes during development.
- Evaluated the interfacial tension of various experimental surfactants and substances using the pendant drop and contact angle method. Analyzed NMR results of substances to identify potential contaminants and degradation.
- Processed data and generated reports to distribute to appropriate team members across 3 different research groups and 3 universities. Led meetings with external collaborators to coordinate research efforts and identify key research questions.

Quality Management Intern November 2019 - March, 2020
Vascular Biosciences
Goleta, CA
Skills: FDA Compliance; Quality Management Systems; Cleanroom; Medical Devices; Animal Studies; Product Packaging; Humanitarian Use Designation (HUD); Orphan Drug Designation; Preclinical Studies

- Prepared and signed off on standard operating procedures for medical device production and testing. Directly oversaw and managed the exchange of trigger springs across multiple lots—this included ensuring all proper documentation and quality assurance tests were performed and submitted.
- Attended weekly management meetings to discuss plans for future increased production and progress checks for FDA preclinical approval. This included working with R&D to redesign animal studies to fit FDA standards with proper controls.
- Identified inconsistencies and proposed new/additional tests for preclinical studies. Designed and implemented a benchtop testing method to measure trigger force and fluid flow.
- Inspected final products for quality concerns or to identify issues with equipment setup and calibration. Oversaw sterilization and product packaging for clinical studies.

Chemical Engineering Teaching Lab Assistant January 2019 – November 2019
Department of Chemical Engineering
University of California - Santa Barbara, CA
Professor: Joseph Chada

Skills: Spectrometry; Distillation; Reaction Engineering; Chromatography; Process Control; Python; LabView; Fluid Mechanics; 3-D Printing; Machining

- Assisted Lab Manager in designing, building, and operating experiments exploring fundamental chemical engineering phenomena for academic use.
- Operated equipment fundamental to chemical engineering processes such as gas chromatographs, refractometers, batch distillation columns, process control, centrifugal pumps, and nickel-catalyst reactors.
- Completed equipment maintenance and calibration tasks according to standards.

Teaching and Mentorship

ENGN 0930L Teaching Assistant – Biomedical Engineering Design and Innovation Fall 2024

Research Mentor, Brown University September 2022 - May 2026

• Connor Yew (Fall 2022 – Spring 2025) – Thesis: Brain-Derived EVs as Concentrated Carriers of Neuronal-Derived Derived Cargo

•Awarded: *Neuroscience Award For Excellence in Academics and Research*

• Everett Gutterman-Johns (Spring 2024 – Spring 2025) – Thesis: Isolation Methods for Brain-Derived EVs

• Anji Friedbauer (Fall 2024 – Spring 2026) – Thesis: "Extracellular Vesicles as Drug Delivery Vehicles"

• Ava Simons (Summer 2024)

• Giada Giuliani (Fall 2025 – Spring 2026)

• Brooke Wangenheim (Fall 2025 – Spring 2026)

Awards and Grants

Zimmerman Innovation Award for Brain Sciences - Carney Institute (2024)

- $50,000 award to support the development assays to quantify and characterize brain-derived extracellular vesicles. The award is intended for novel, high risk projects with the potential to advance science and benefit society in enduring ways.

SLAS Tony B. Travel Award - Society for Laboratory Automation and Screening (2025)

- Awarded full funding to travel to San Diego to give a Podium Presentation titled “Methods for Fast Immune Phenotyping of Extracellular Vesicles in Human Biofluids” for the “Algorithmic Patient Based Care” session at SLAS 2025 conference.

Acknowledgements

First, I would like to express my gratitude to my advisor, Dr. Anubhav Tripathi, for his invaluable guidance, technical expertise, and unwavering support throughout this journey. His mentorship has been instrumental in my development as a scientist and professional throughout my time at Brown University. One of the things I have valued most is the way he treated me as an equal and a colleague from the very beginning. That level of respect was a powerful motivator for me; it pushed me to rise to the occasion and strive to match the standard of excellence and professionalism he modeled every day.

I would also like to thank my dissertation committee for their insightful feedback and expertise. Their flexibility in planning and consistent encouragement was vital in navigating the complexities of this work, and I appreciate the time they dedicated to my professional growth.

I need to give a big thanks to all of my current labmates - Jenna Rutberg, Kathryn Whitehead, Sarah Planchak, Ells Mine Saint Paul, and Julia Miller. You've made the lab feel like so much more than just a place of work. Thank you for your constant help, your kindness, and for building the kind of collaborative, welcoming environment that made even the toughest days manageable. A very special thank you goes to Julia. Your incredible dedication and willingness to step in and take over my work gave me the headspace and peace of mind I truly needed to focus on finishing this degree. I honestly don't know if I could have crossed the finish line without that support, and for that, I am beyond grateful.

I also owe a huge debt of gratitude to the lab members who came before me—Adriana Coll de Pena, Duuluu Naranbhat, and Ramisa Fariha. Your mentorship during my early years really set the foundation for everything I've done since.

To my undergraduate students: thank you for all the hard work and energy you brought to the lab. It's been such a pleasure working alongside you, and I'll be rooting for you as you head into your post-grad studies and whatever adventures come next.

The smooth operation of my research would not have been possible without Lori Basset, John Lee, and Andy Flores. Thank you for your tireless help with administration duties and ordering. Your hard work allows us all to give our full attention to our research. I would also like to extend an additional thank you to John Murphy for his time and valuable insights into lab automation.

I am also grateful to Kishore Malyavantham, Mingwei Zhao, and Masoud Toloue from Quanterix Corporation for sharing their time and extensive knowledge of Simoa technology, which was crucial to the success of this project.

Beyond the lab, I found a much-needed sanctuary at Burke's Martial Arts. A huge thank you to Coaches Num and Jamieson for creating such a welcoming space to decompress; you both helped me keep my martial arts journey moving forward right alongside my academic one, which kept me grounded through it all. During my time there I was also introduced to many new friends, including Anna and Calista. To you both, thank you for the memories and the much-needed breaks. To my best friend, Samra Zaheer, thank you

for enduring friendship and for being a constant pillar of support through every high and low.

Finally, I want to thank my parents. None of this would have been possible without your unconditional love and support. Thank you for always believing in me and listening to my late Sunday night rants.

Contents

List of Figures

List of Tables

List of Supporting Information Figures

SiMoA EV quantification assay to calculate the concentration of vesicles in normal and breast cancer serum. The average reported diameter is 132.0 nm +/- 69.8 nm.

Figure S4.1 The total yield of EVs isolated via overnight immunoaffinity isolation was compared between NCAM and a mouse IgG isotype control bead. Beads were incubated overnight with 1 mL of plasma prior to the EVs being eluted off the surface and analyzed using an NCAM capture and CD9 detection assay. The AEB produced by both eluents was analyzed. NCAM capture beads depleted the plasma of any detectable NCAM EVs. In contrast, the isotype control eluent yielded no detectable signal.

Figure S4.2 A Malvern ZetaView instrument was used to measure the yield of EVs isolated from pooled normal human serum via ultracentrifugation. The resulting pellet was resuspended in EV sample diluent and aliquoted prior to storage.

Figure S4.3 The specificity of the assay for intact, membrane-enclosed EVs and not solubilized protein was tested by comparing the signal between untreated plasma (4X dilution) and plasma treated with 1% Triton X-100. The resulting AEB is reported here using a pan-tetraspanin detector. The significant decrease in AEB after lysis indicates that solubilized protein does form a detectable immunocomplex.

Figure S5.1 Calibration curves generated for CD9 capture and interchanging detector probes to target CD9, CD63, and CD81. EVs isolated from normal EDTA plasma via ultracentrifugation were utilized as the calibration material.

Figure S5.2 The specificity of the assay for whole EVs, and not free floating tetraspanins, was tested by comparing the signal of untreated EVs to EVs treated with 1% Triton X-100. Significant reduction in signal indicates that both CD63 and CD9 must be present on the EV for detection. No signal is observed if the EV is lysed because the sandwich complex cannot form.

Figure S5.3 Nanoparticle tracking analysis results for normal EDTA plasma EVs isolated via ultracentrifugation. EVs were used as standards for the SiMoA EV quantification assay.

Figure S5.4 Correlation plot between reported NTA concentration and reported SiMoA concentration of 3 EV eluent samples.

Figure S5.5 Nanoparticle tracking analysis results for glioblastoma cell conditioned media EVs isolated via ultracentrifugation. EVs were used as standards for the SiMoA EV quantification assay and spiked into normal plasma for proteomic analysis.

Figure S5.6 Correlation plot between PanTet/CD9 and NCAM/CD9 assay for the normal plasma cohort (n = 10). One plasma sample fell below the limit of detection for the NCAM/CD9 configuration and is not shown. Analysis was done using the correlation function on GraphPad version 10.0.2.

Figure S5.7 Correlation plot between PanTet/CD9 and ATP1A3/CD9 assay for the normal plasma cohort (n = 10). One plasma sample fell below the limit of detection for the

ATP1A3/CD9 configuration and is not shown. Analysis was done using the correlation function on GraphPad version 10.0.2.

Figure S5.8 Correlation plot between PanTet/CD9 and L1CAM/CD9 assay for the normal plasma cohort (n = 10). One plasma sample fell below the limit of detection for the L1CAM/CD9 configuration and is not shown. Analysis was done using the correlation function on GraphPad version 10.0.2.

Figure S5.9 EV immunoaffinity isolation was performed on 1 mL of normal EDTA plasma using 150 μL of beads. The EVs were subsequently eluted and then lysed prior to measurement using Neurology 4-Plex E from Quanterix. The protein concentration was measured in duplicate. For the isotype control, the concentrations of both Aβ-42 and GFAP were below the limit of quantification (LOQ).

Figure S5.10 Results of testing 2X dilutions of normal EDTA plasma using anti-ATP1A3 beads as the capture and anti-NCAM as the detector. Both plasma samples tested indicated colocalization of ATP1A3 and NCAM on the surface of the vesicle.

Figure S5.11 Results of testing 2X dilutions of normal EDTA plasma and glioblastoma cell media using anti-NCAM beads as the capture and anti-L1CAM as the detector. Both plasma samples tested indicated high colocalization of L1CAM and NCAM on the surface of the vesicle.

List of Supporting Information Tables

CHAPTER 1: Background

1.1 Motivation

Our fundamental understanding of health relies on a wide variety of biomarkers - from nucleic acids to lipids and proteins. Over the past two decades, the transition from viewing biological systems through a single lens to a multi-omics perspective represents a fundamental shift in how we monitor and understand human health (Figure 1.1).[1-3] While genomics provides the foundational blueprint of an individual's genetic risk, it is inherently static and often does not account for the dynamic influences of aging, environment, or lifestyle. The multi-omic perspective bridges this gap by integrating data from various biological layers, including the transcriptome, proteome, and metabolome, to create a holistic, high-definition map of a patient's physiological state. This integrated approach is the foundation of precision medicine, providing clinicians the ability to move beyond generalized treatments and pushing them toward interventions tailored to a patient's unique molecular phenotype and enabling the disease detection prior to the onset of clinical symptoms.[4]

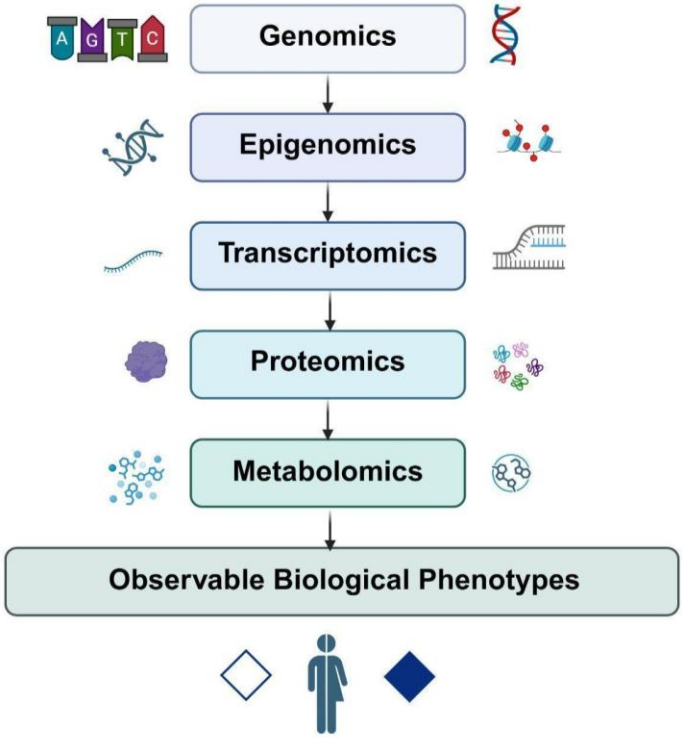

Figure 1.1 A visual representation of the multi-omic hierarchy. (Image created with Biorender.com)

Within this hierarchy, proteomics occupies a central role as the primary driver of cellular function.[5] While the genome defines the range of all potential biological outcomes, the proteome is a direct reflection of what is actually happening in real time. Proteins are the primary effectors of cellular function, serving as catalysts, structural components, and signaling molecules.[6] Because protein expression and post-translational modifications change rapidly in response to disease or therapeutic intervention, the proteome serves as a snapshot of the current molecular state.[7,8] Consequently, most modern drug discovery efforts focus on the proteome, as proteins make up the vast majority of actionable therapeutic targets.[9,10]

The study of Extracellular Vesicles (EVs) is closely integrated with proteomics, acting as a distinct and specialized component of the larger proteomic landscape. EVs are membrane-bound lipid nanoparticles shed by cells into biofluids, carrying a selective cargo of proteins reflective of their cellular origin.[11] By encapsulating these proteins within a protective membrane, EVs preserve molecular integrity and enable the recovery of proteomic signals that would otherwise be obscured in complex matrices such as blood. In the context of liquid biopsy, EV-based proteomic analysis supports tissue-specific monitoring; by targeting vesicles expressing defined surface markers, including those derived from the central nervous system (CNS), it becomes possible to non-invasively assess the molecular state of otherwise inaccessible tissues.[12,13]

Liquid biopsies are minimally invasive diagnostic approaches used to assess biological markers for disease detection and monitoring.[14,15] Among available biofluids, blood is most commonly utilized due to its role as the body's primary transport network and its function as a systemic reservoir of circulating biomarkers. It circulates through almost every organ in the body and contains a wide variety of potential analytes. In the context of oncology, blood samples have high potential for detecting and monitoring metastatic sites, as it can be used to catch the presence of circulating tumor cells (CTCs) and circulating tumor DNA (ctDNA).[16] Other biofluids such as cerebral spinal fluid (CSF), urine, and saliva are more limited in their applications, but are also used under special circumstances. In neurological contexts, CSF is especially informative because the brain is separated from peripheral circulation by the blood-brain-barrier, a highly selective interface that's primary role is to regulate molecular transport between the brain and periphery. It limits the amount of

molecular information we are able to gather via traditional blood draws. In contrast, CSF bypasses this barrier as it has direct contact with the interstitial fluid of the brain and spinal cord, providing a more proximal representation of CNS activity, and in many cases, greater diagnostic specificity.[17-19] Despite these advantages, CSF collection via lumbar puncture is invasive and can often be uncomfortable for patients, thus limiting its suitability for routine or large-scale screening. As a result, blood-based biomarkers continue to be the preferred standard in clinical practice, offering a balance of between accessibility, scalability, and diagnostic utility.[20,21]

1.2 Extracellular Vesicles

EVs are increasingly being recognized for their involvement in a broad range of physiological and pathological processes, spanning roles in cellular homeostasis to the dissemination of disease-associated cargo. They have consequently gained attention as promising components in emerging diagnostic and therapeutic strategies.[22-24] EVs are lipid bilayer-enclosed particles generated through multiple biogenesis pathways and can carry diverse molecular constituents, including nucleic acids, lipids, metabolites, and proteins (Figure 1.2).[25] These components may be associated with the vesicle surface, embedded within the membrane, or enclosed in the luminal space.[26] EV diagnostics primarily focus on identifying disease specific signatures during early disease pathogenesis. Vesicles originating from specific tissues can be recovered in peripheral biofluids, offering a far less invasive alternative to traditional tissue biopsies used to diagnose cancer and some

inflammatory diseases.[27,28] By isolating EVs from fluids such as blood, urine, and saliva, it is possible to monitor dynamic, cell-type-specific responses over time.

In oncology, EVs have been extensively investigated due to their potential to capture tumor heterogeneity more comprehensively than localized biopsy samples. Ongoing research has examined how EV-associated proteins, nucleic acids, and overall vesicle concentration vary with disease progression. Distinct EV signatures have also been reported across a range of conditions such as cardiovascular, infectious, and neurodegeneration.[29-31] Notably, brain-derived EVs (bdEVs) have been identified to carry biomarkers of relevant to neurodegenerative disorders such as Alzheimer's and Parkinson's disease.[32-35]

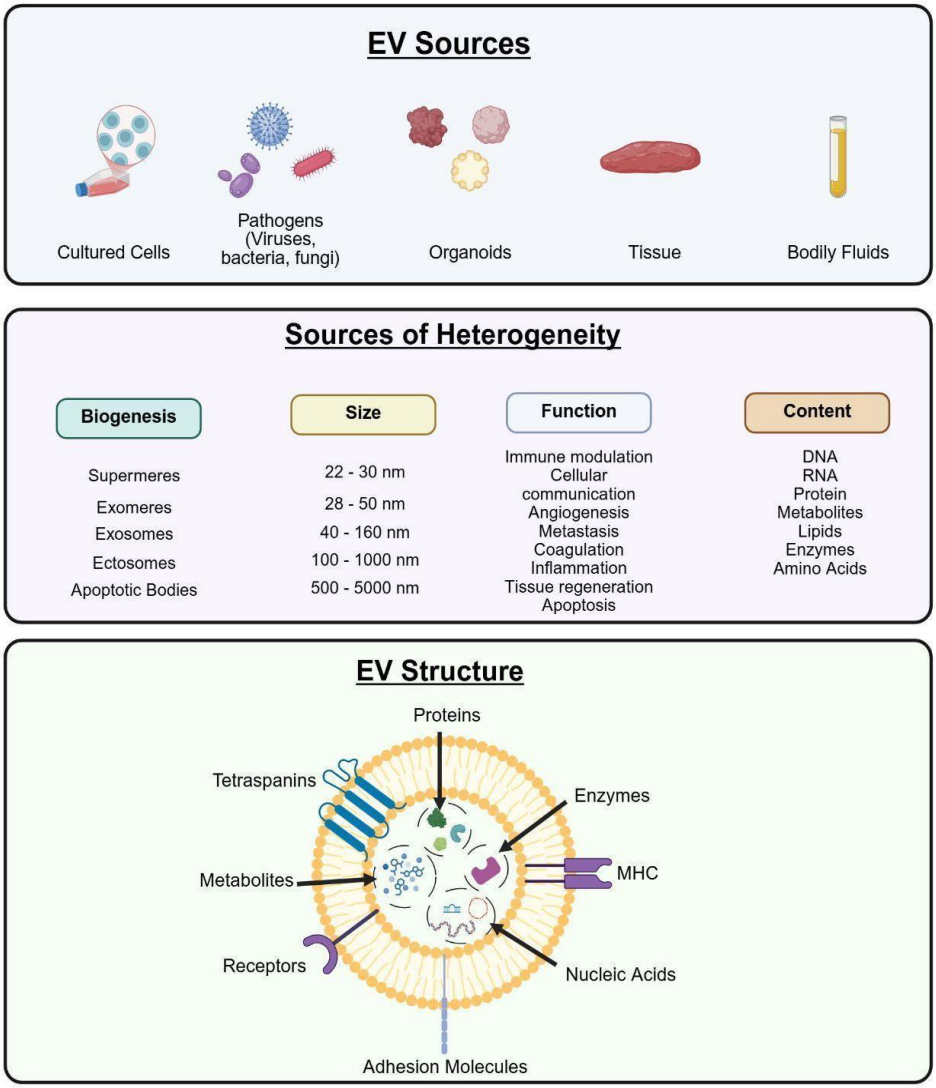

Figure 1.2 EV heterogeneity is a result of multiple factors. This schematic showcases the different sources of EVs and how biogenesis contributes to the overall population heterogeneity seen in nature. The EV structure diagram is a simplified representation of EVs in general. (Image created with Biorender.com)

EVs have also gained traction as therapeutic platforms for treating a multitude of diseases, owing to their natural role as intercellular communicators. They are increasingly being explored as alternatives to lipid nanoparticles (LNPs) largely due to their low

immunogenicity, higher stability, and capacity to traverse the blood-brain-barrier.[36] Natural EVs, such as those derived from mesenchymal stem cells (MSCs), have been found in preclinical models to have regenerative and anti-inflammatory effects.[37] In parallel, engineered EVs are being developed to selectively target diseased cells and transport therapeutic payloads, including small molecules, siRNA, and enzymatic cargo. At present, there are over 240 clinical trials registered worldwide involving EVs, with several candidates having reached late stage development (Phase II/III).[38-40] Despite this progress, translation from preclinical models to human application remains limited by several key challenges: scalability, standardization, and regulatory ambiguity.[41] These barriers stem from the intrinsic complexity and heterogeneity of EV populations. EVs do not fit neatly within existing regulatory frameworks, underscoring the need for new methods and strategies to properly regulate production.

1.3 EV Isolation Methods

Due to the heterogeneous nature of EVs and the lack of a universal marker, isolation from biofluids and tissues is a recurring source of tension within the community. There is no single perfect method for isolation as it depends on the downstream purpose for the vesicles. Balancing purity and yield is an art form, and many labs have developed their own methods best suited for their studies. The lack of standardization has made reproducibility difficult. To combat this, the Minimal Information for Studies of Extracellular Vesicles (MISEV) guidelines have been developed and are regularly updated by the International Society for Extracellular Vesicles. A summary of the most popular isolation methods is detailed in Table 1.1.

Table 1.1 Summary of popular EV isolation techniques that compares yield and purity.[42,43]

Method	**Principle**	**Yield**	**Purity**
Ultracentrifugation	density/size (sedimentation)	High	Moderate
Size-exclusion chromatography	Size (porous resin)	Moderate	High
Ultrafiltration	Size (filter membrane)	High	High
Polymer Precipitation	Solubility (e.g. PEG)	Highest	Lowest
Immunoaffinity Capture	Surface markers (antibodies)	Low	Highest
Microfluidics	Physical/chemical (on a chip)	Low	High

Methods that yield the greatest number of vesicles for a low cost (i.e. ultracentrifugation and precipitation) are optimal for discovery and investigational use. These methods offer wide spread yield for initial mapping and enable novel target discovery. For functional and therapeutic studies, high purity is a necessity to ensure that no contaminants are transferred. SEC and TFF are great options for these types of validation phases since they offer high purity and moderate to high yields. For clinical diagnostic applications, immunoaffinity offers the highest purity and greatest target specificity to measure a few key targets.

1.4 Current Analytical Methods

One of the contributing factors to the recent rise in popularity of EVs has been the evolution of the analytical landscape for nano-sized specimens.[44] Tools have evolved from enabling basic discovery into sophisticated technologies designed to address the inherent

heterogeneity of EV populations (Table 1.2). Their vast size range (30 - 1000 nm) within complex biofluids poses a significant analytical challenge, as there is no single "gold standard" method similar to isolation methods. Instead, multi-modal approaches are best suited to characterize the physical properties, concentration, and molecular cargo of EVs. Western Blot (WB) and ELISA remain as the anchors in the field for traditional protein analysis. Western blotting is a qualitative tool utilized by researchers to confirm the presence of EV-specific markers such as CD63, CD81, and CD9 on the surface and internal markers like TSG101 and Alix.[45] Traditional plate-based ELISAs are used in a similar context to quantify total protein concentration. However, both methods typically require a significant volume of sample to perform a bulk analysis and do not provide any insight into single vesicle morphology.

Table 1.2 A summary of popular EV analytical methods that compares yield and purity.[46-48]

Method	**Benefits**	**Potential Drawbacks**
Nanoparticle Tracking	Provides size distribution and concentration	Cannot measure particles < 30 nm Potentially measures non-EV contaminants such as lipoproteins
Flow Cytometry	Simultaneously measure multiple surface markers High sensitivity to measure EV subpopulations Fast data acquisition	Often misses EVs < 150 nm Susceptible to the "swarm effect" - miscounting groups of small EVs
Nanoscale Flow Cytometry	Can simultaneously measure size and protein markers Individual EV resolution Fast data acquisition	Struggles to measure small EVs < 30nm Complex sample preparation and calibration

Traditional ELISA	Measure concentration Cost-effective and accessible High specificity	Low sensitivity Cannot detect sample heterogeneity No size information
Western Blot	Confirm the presence of multiple EV markers / proteins	Time consuming Not suited for low abundant markers
Electron Microscopy	Highest resolution for direct visualization Measure EV size and integrity	Low throughout / expensive Cannot reliably measure concentration Artifacts can arise from dehydration

The "gold standard" analytical tool for visualizing vesicles with the highest fidelity to ensure that what has been isolated is not just "cellular dust" is Electron Microscopy (EM).[49] In particular, Transmission Electron Microscopy (TEM) or Cryo-EM, remain as indispensable tools to verify the "cup-shaped" morphology of EVs to distinguish them from potential non-membranous protein aggregates and lipoproteins.[50] Cryo-EM is considered the best method for preserving the vesicle's native state because it avoids potential artifacts that arise from the process of dehydrating the sample. Both methods, however, are extremely time-consuming and low-throughput. They also cannot be used to accurately provide statistically significant data on the total concentration due to spotting effects.[51] Nanoparticle Tracking Analysis (NTA) is used to fill this gap. NTA bridges the gap between high-resolution imaging and quantification by utilizing the properties of Brownian motion and light scattering to determine the size and concentration of a sample. It tracks the movement of individual particles through a microfluidics channel to provide a high-resolution size profile that is more accurate than Dynamic Light Scattering (DLS) for

such polydisperse samples.[52,53] The major limitation of NTA is that it cannot distinguish EVs from similarly sized contaminants.

The most significant shift in recent years has been the push towards single-vesicle analysis. This move has been dominated by the development of flow cytometry and nano flow cytometry (nFCM). Traditional flow cytometers were designed for the analysis of micron-sized cells and would often miss the dim signal of small, sub-100nm EVs. The invention of nFCM, a tool dedicated to small-particle flow cytometry, has revolutionized the field. With its high resolution, nFCM is capable of measuring size, concentration, and multi-marker protein expression of individual particles.[54,55] Researchers can use fluorescently tagged antibodies to label specific EV subpopulations - such as targeting $L1CAM^{+}$ neuron derived vesicles - within a sample. Unfortunately, this method is not without its drawbacks, as it is subject to a few major technical hurdles such as the swarm effect, limits of light scattering, high-cost, and a lack of proper standardized reference materials.[56,57] As the field continues to grow and move forward, the integration of these methods combining structural validation using EM and the molecular specificity of nano flow cytometry enables a new era of high-precision liquid biopsy frameworks.

1.5 Digital Single Molecule Array Technology

Single molecule array technology (SiMoA) has revolutionized precision medicine by increasing the sensitivity up to 1000-fold over traditional methods and redefining our approach to quantifying low abundance biomarkers in biofluids.[58-61] It was created out of the need to detect biomarkers whose concentrations are far below the reach of conventional

enzyme-linked immunosorbent assays (ELISA). A standard plate-based ELISA has a limit of detection around 10^{-12} M (1 pM). Many critical biomarkers for early-stage cancer and neurodegenerative diseases are present at femtomolar and even attamolar concentrations. The primary innovation of SiMoA is its ability to isolate individual immunocomplexes within femtoliter-sized reaction chambers, effectively concentrating the signal generation to enable a digital readout.[58]

The fundamental working principle of SiMoA starts with a modified sandwich assay that is performed on the surface of microscopic beads. Magnetic microbeads (2.7 μm) are functionalized with specific capture antibodies against the desired analyte. Next, the beads are incubated with a sample (such as serum or plasma) to capture the target protein molecules. The sample is run in the presence of an excess of beads, typically 500,000, in order to ensure that following the laws of probability that a bead will either capture one molecule or none at all. Post-capture, a biotinylated detection antibody and enzyme label, such as streptavidin-β-galactosidase (SβG), are added to the solution. The result is a sandwich immunocomplex on the bead surface. SiMoA's true innovation then occurs during the detection and analysis step that follows.

The beads are then loaded onto a specialized microarray that contains approximately 215,000 micro-wells that are 4.25 μm in diameter (40 femtoliters). The confinement of each bead to its own individual well is what enables SiMoA's high sensitivity. In a conventional plate-based ELISA, the signal that is generated by the enzyme is diluted into

a significantly larger amount of surrounding buffer. Therefore, it takes a significantly greater amount of enzyme to produce a detectable signal. In contrast, SiMoA isolates the beads into single wells and seals them using oil. The product of the enzymatic reaction is then confined to that single, femtoliter sized space. Within a few minutes, the concentration of the fluorescent product reaches a detectable concentration by standard optical imaging.[59]

The next important step in turning the signal generated into a quantifiable concentration is utilizing Poisson Distribution to calculate the average enzymatic activity per bead. Going back, one of the first key assumptions and working principles of the assay is that the sample is run with an excess of beads. In a well-mixed system, this ensures that the distribution of molecules across the beads follows a Poisson Distribution. That is, the probability, *P(n)*, that a bead will capture *n* molecules is given by the formula:[62,63]

$$P(n) = \frac{\mu^n e^{-\mu}}{n!} \qquad \textbf{Equation 1.1}$$

Where μ represents the average number of molecules per bead. At low concentrations, μ is less than 1, meaning that a majority of beads will capture zero molecules ($n = 0$), and only a small fraction will capture exactly one molecule. A negligible amount will capture more than one molecule. Here, the number of "on" wells is counted versus "off" wells to determine the concentration of the analyte. This is known as digital detection, because the results are binary - the well is either on or off (1 or a 0).

As concentration increases, the probability that multiple molecules will bind to a single bead increases. At significantly high concentrations, the digital approach begins to saturate as μ approaches 1. At this point, SiMoA transitions to analog measurements. The instrument then measures the total intensity of the fluorescent signal across the array. This dual mode increases the sensitivity and dynamic range of the assay across four or five orders of magnitude.

These changes have resulted in a massive shift in perspective from focusing on late-stage monitoring to early-stage disease detection. It has enabled the detection of key biomarkers such as NfL and tau proteins in peripheral blood.[64,65] Markers that previously could only be measured via invasive lumbar punctures to collect CSF. In oncology, the ultrasensitivity has allowed for the detection of low levels of prostate-specific antigen (PSA) to provide an early detection system for cancer recurrence.[66] This system combines the specificity of antibody-based target recognition with a novel application of femtoliter sized reactors and Poisson statistics to enhance protein detection. This has created a new frontier for preventative care and precision medicine.

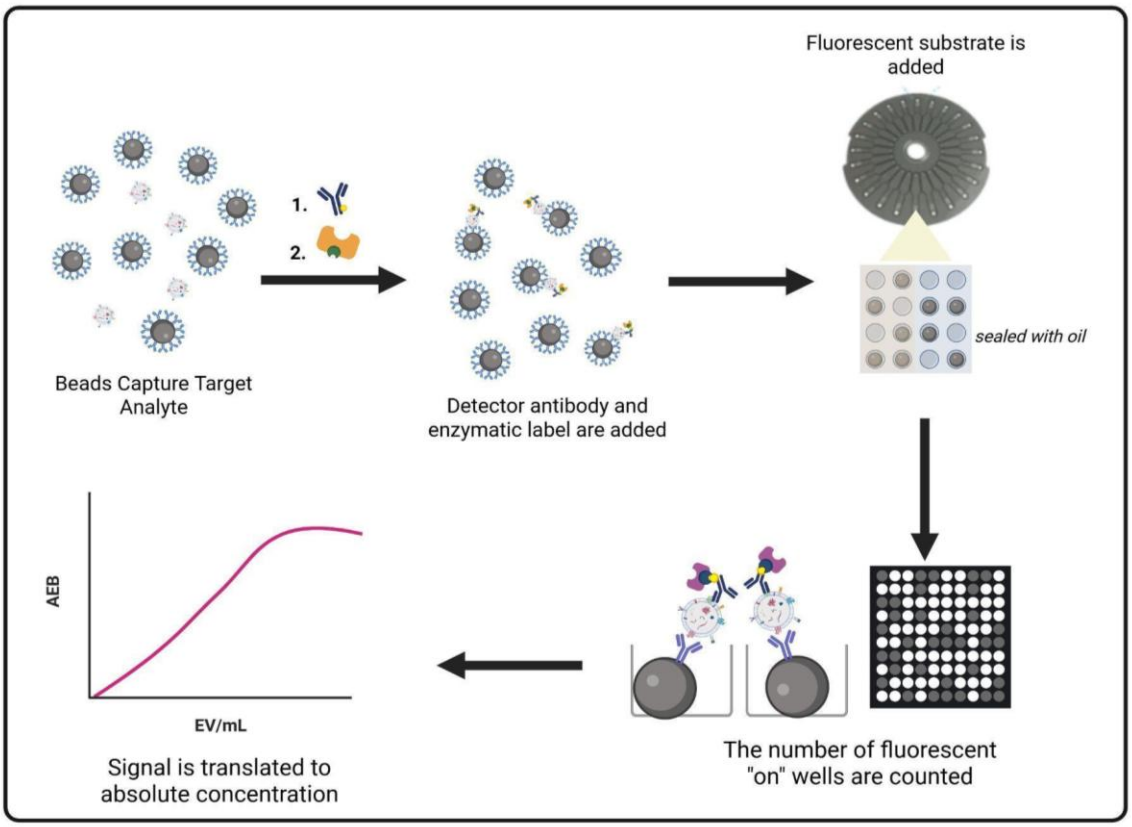

Figure 1.3 A simplified visual representation of Single Molecule Array Technology for the detection of EVs in biofluids. (Image created using Biorender.com)

1.6 Neurology Applications

The diagnostic landscape for neurodegenerative diseases, such as Alzheimer's (AD) and Parkinson's disease (PD), has witnessed a historic turning point within the past decade due to the introduction of ultrasensitive analyte detection platforms like SiMoA.[67-69] The field has shifted from a reactive, symptom-based approach to a more proactive, molecular-driven framework. Conditions like AD and PD are now identified by the presence of pathological plaques and tangles in the brain, rather than the onset of cognitive decline. This is primarily due to the increased availability of tools used to measure high-performance blood-based biomarkers. The previous gold standard diagnosis techniques

required invasive lumbar punctures and expensive PET imaging. The formal integration of plasma biomarkers by the 2024 NIA-AA Revised Criteria has made widespread testing more available.[70]

This shift has led scientists and clinicians to identify multiple powerful biomarkers for monitoring patient neurological health such as amyloid-beta (Aβ), neurofilament light (NfL), glial fibrillary acidic protein (GFAP), alpha-synuclein (SAA), and some tau isoforms. The most prominent novel biomarker being p-tau217, which has achieved a diagnostic accuracy exceeding 90%.[68] It is used often as a benchmark to determine if a patient qualifies for new disease-modifying therapies (DMTs). By measuring this specific isoform, clinicians can identify AD pathology up to 15 years prior to clinical symptom onset.

Multi-modal diagnostic frameworks, such as the AT(N)I framework used for AD, are now used to map a patient's unique molecular fingerprint.[71-73] Clinicians monitor multiple biomarkers over time to assess patient health and identify early disease pathology. Aβ levels are used as an early indicator of plaque formation, tau progression is used to correlate with cognitive decline, and NfL is used to monitor general neurodegeneration. Additionally, GFAP offers itself as a good indicator of inflammation by signaling astrocyte reactivity. These sorts of multi-modal frameworks help break down an individual's biotype and eligibility for potential DMTs by ruling out other forms of dementia.[74]

Brain-derived extracellular vesicles are on the frontier of neurodegeneration research as they allow researchers to sample the brain's internal environment non-invasively. BdEVs

can be isolated using cell specific surface markers to capture EVs in plasma. All the biomarkers previously mentioned have been positively identified in circulating EVs. In particular, bdEVs may play a vital role in transporting pathological tau and SAA from diseased to healthy neurons, effectively seeding these proteins throughout the brain.[54,75,76]

1.7 Oncology Applications

SiMoA's ability to push the limits of biomarker quantification into the femtomolar range has also pushed the field of cancer diagnostics towards a more proactive perspective. It can be used to measure ultra-low concentrations of tumor-derived proteins, including tumor-derived EVs (tEVs). These markers can appear in blood long before the tumor is large enough to be captured by conventional CT or MRI scans.[77,78] This provides a pre-symptomatic detection tool to enable early clinical intervention at stages I or II when survival rates are exponentially higher for many cancers. Cell-free DNA (ctDNA) has long been the focus of liquid biopsies to monitor cancer, but tEVs now offer a more robust and functionally relevant snapshot of tumor microenvironment. Unlike ctDNA, which is often released during cell death, tEVs are secreted by living, metabolically active tumor cells. These vesicles carry important DNA, RNA, and protein cargo that can be further used to characterize the tumor's metabolic and functional status.[79] SiMoA's high sensitivity enables the detection of small tEV subpopulations obscured by the vast majority of EV secreted by platelets and healthy immune cells. Utilizing dual-targeted sandwich assays - for instance capturing vesicles using a universal EV marker like CD63 and detecting it via a tumor-specific marker like EGFR or EpCAM - SiMoA can be used to quantify the presence of circulating cancer-specific EVs.

SiMoA's multiplex capability also enables a more comprehensive multi-omic approach. Systemic inflammation markers (IL-6, TNF-α, and IL-1β) can be measured alongside tEVs to get a more holistic view of the patient's health and monitor their body's response to treatment. Previous work has established the potential of EVs to be used as a marker for cancer recurrence and metastasis. For example, the presence of PD-L1 on circulating EVs has been found to enable the prediction of how patients will respond to checkpoint inhibitors. Researchers were able to utilize these vesicles to monitor patients for signs of immune related adverse effects.[80] Ultimately, the synergy between ultra-sensitive digital detection and the important biological cargo transported within tEVs is enabling a new standard of care, where cancer is managed as a chronic, monitorable condition rather than an unpredictable crisis.

1.8 Summary and Research Overview

This thesis focuses on applying fundamental principles of engineering to forward the development of ultrasensitive analytical methods and frameworks for detecting and quantifying low-abundance biomarkers in biofluids. To achieve these objectives, a great significance was placed on understanding the limitations of current biochemical methods and applying novel signal amplification and analysis techniques to increase assay sensitivity. This thesis also explored fundamental principles of biochemistry in order to conjugate capture and detector probes as well as evaluate the impact of intermolecular forces on assay performance.

A visual overview of this thesis and its scientific outcomes are shown in Figure 1.4.

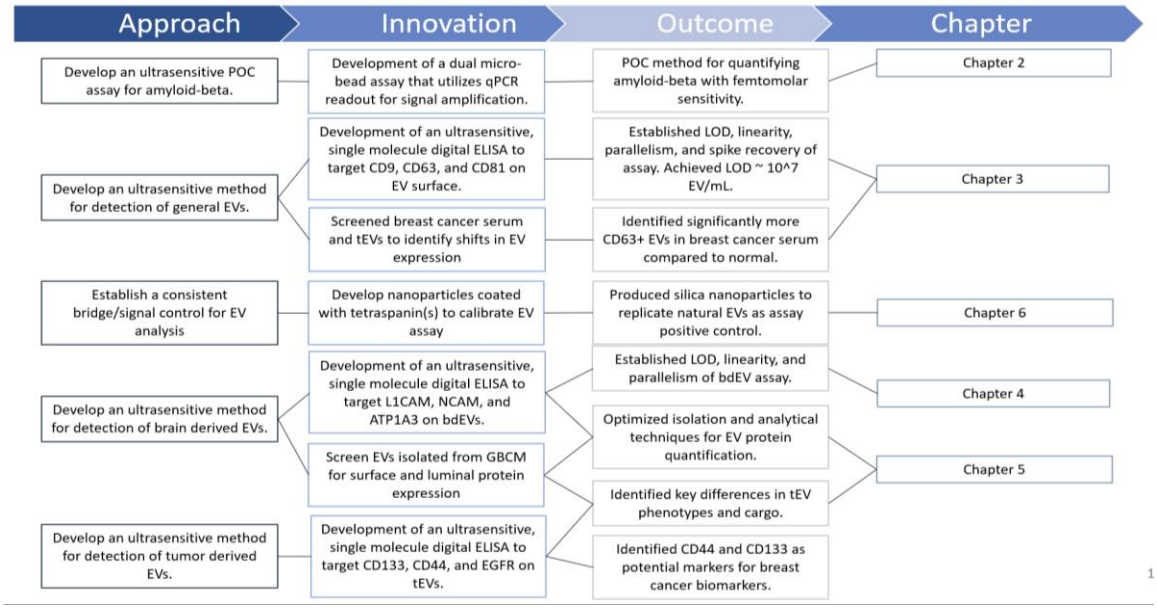

Figure 1.4 Outline of the contributions of this thesis to developing and optimizing analytical methods for EV isolation and characterization.

Chapter 2 of this thesis describes the development of a novel, ultrasensitive method for the decentralized quantification of Aβ (1-42). Traditional detection methods like ELISA lack the sensitivity required to measure ultra-low concentration of Aβ (1-42) found in plasma. Additionally, commercially available ultrasensitive methods require expensive reagents and machines for readouts. To overcome these limitations, this work explores a unique dual-microbead sandwich assay integrated with quantitative polymerase chain reaction (qPCR). The mechanism employs two types of functionalized microparticles: magnetic microparticles (MMPs) for target capture and polystyrene beads (PSNPs) carrying both a detection antibody and unique ssDNA tag. In the presence of Aβ (1-42), both beads form an immunocomplex around the analyte. This complex is then detected using qPCR to exponentially amplify the ssDNA on the PSNP. This unique approach achieved a limit of detection of 0.05 pg/mL (12.5 fM) which is significantly more sensitive than most

commercially available kits. The key innovation of this work is the optimization of surface functionalization and streamlined protocol, which allows for qPCR to be performed directly on the bead surface with no need for decoupling. This reduces hands-on processing time to only 20 minutes. By utilizing the superior binding kinetics of microparticles to overcome the limits of diffusion and the high signal amplification of PCR, this technology provides a robust platform for protein quantification.

Chapter 3 outlines the development of an ultra-sensitive SiMoA assay for the direct quantification of EVs in complex biofluids (such as serum and plasma). EVs are promising biomarkers for oncology and neurology, but their clinical use has been limited by the need for tedious sample preparation. This major technical hurdle is addressed by implementing a continuous mathematical model to calculate the average enzymes per bead to maintain a large dynamic range suitable for measuring EV concentrations over four orders of magnitude. This proves that under the correct conditions, the large size and polyvalency of EVs compared to normal proteins does not violate Poisson statistics and the digital logic framework still applies. In total, this study evaluated the sensitivity of 12 assay configurations targeting the three tetraspanins CD9, CD63, and CD81. It identified CD63 capture and CD9 detection as a promising capture and detector pair due to its superior sensitivity and strong clinical applications for cancer detection. Furthermore, the assay demonstrated superior inter-plate reproducibility compared to commercial assays. Ultimately, this work provides a scalable, high-throughput framework that shifts the

paradigm from labor-intensive EV isolation to a direct quantification method for early disease detection and monitoring.

Chapter 4 presents the development of 3 digital SiMoA assays for the direct quantification of brain-derived extracellular vesicles (bdEVs) in plasma and serum. It applies the same continuous piecewise mathematical model based on Poisson statistics to calculate the AEB. Currently, diagnosing neurological disorders via blood is extremely difficult due to the presence of the blood-brain-barrier and dilution of brain-specific signals when they reach the bloodstream. BdEVs offer a potential solution due to their ability to cross the blood-brain-barrier. This chapter evaluates the performance of SiMoA technology alongside three neuron specific EVmarkers - L1CAM, NCAM, and ATP1A3 - to quantify bdEVs in plasma and serum. This work presents NCAM as a potentially superior choice to L1CAM for EV quantification. NCAM achieved the highest sensitivity of 1.03×10^7 particles/mL. Additionally, ATP1A3 demonstrated the greatest clinical utility by successfully quantifying bdEVs in over 92% of samples tested. NCAM and ATP1A3's superior performance to L1CAM is attributed to L1CAM's tendency to "shed" isoforms. By enabling the direct profiling of CNS-specific vesicles from blood, this digital detection tool offers a more standardized and scalable method for monitoring neurodegenerative diseases and neuro-oncology.

Chapter 5 utilizes the assays developed in chapters 3 and 4 to provide a methodological framework for the proteomic characterization of bdEVs and glioblastoma-derived EVs. A key finding of the study was that all three neuronal markers yielded similar quantities of

bdEVs from normal plasma. Furthermore, EVs isolated using NCAM capture beads demonstrated a significantly higher average loading density of neurodegenerative biomarkers, Aβ, NfL, and GFAP, compared to EVs isolated using generic CD9 capture. These results suggest that subtyping EVs by cellular origin may drastically enhance diagnostic sensitivity by reducing peripheral noise. The study also identified a distinct EV phenotype in glioblastoma-derived EVs that is characterized by elevated CD63 and GFAP expression. Though these in-vitro results require more thorough clinical validation, the study establishes a powerful proof-of-concept to using SiMoA-based phenotyping to detect CNS pathologies via a non-invasive blood draw.

Chapter 6 showcases the foundation of the development of novel biomimetic silica nanoparticles as an alternative to using naturally derived ones to create standard curves for EV quantification. This chapter addresses concerns over reproducibility between studies and different research platforms that stem from the extreme biological heterogeneity of EVs. The presented solution is the utilization of silica nanoparticles co-conjugated with CD9 and BSA to replace natural EV standards. These particles can produce a standard curve that spans five orders of magnitude and have a limit of detection of 2.0×10^6 particles/mL.

Chapter 7 presents the final concluding thoughts along with a summary of the impact of the work described. Considerations for future work and directions are also provided.

CHAPTER 2:

Utilizing Functionalized Dual-Microbead Interfaces for Measurements of Amyloid-beta(1-42) with FemtoMolar Sensitivity

---

Chapter 2 has been published as an original research article.

Pollock J.[1]; Yew, C.[1]; Tripathi A.[1] "Utilizing Functionalized Dual-Microbead Interfaces for Measurements of Amyloid-beta (1-42) with Femtomolar Sensitivity" *Langmuir : the ACS journal of surfaces and colloids* vol. 41,9 (2025): 5870-5876.

1. Center for Biomedical Engineering, School of Engineering, Brown University, Providence, RI, USA

2.1 Abstract

The presence of amyloid-beta (1-42) in CSF and plasma has been implicated as pathological hallmarks of Alzheimer's disease. Here, we demonstrate a high sensitivity method of detection and quantification for Aβ42 utilizing two-antibody functionalized microparticles interfaces. Our method of biomarker detection utilizes two types of microbeads: (1) magnetic particles functionalized with monoclonal antibodies and (2) polystyrene particles dual functionalized with monoclonal antibodies and a unique DNA "tag". The bead complex that forms in the presence of the target analyte is detected using qPCR to determine the analyte concentration. To demonstrate our method, we tested the presence of amyloid-beta (1-42) in Tris buffer. The established limit of detection for this assay is 0.05 pg mL^{-1}(12.5 femto-molar) in purified samples This study provides an improved method of protein detection that could be used for early diagnosis of Alzheimer's Disease.

2.2 Introduction

Alzheimer's disease (AD) is a fatal neurodegenerative disorder that is associated with cognitive, functional, and behavioral impairments.[81,82] It affects approximately 10% of people over the age of 65 years and threatens to place a large burden on healthcare systems around the world.[81] AD death rates continue to steadily increase as rates for cardiovascular disease and strokes have decreased,[81] and the number of patients diagnosed with AD is predicted to reach 152 million people globally by the year 2050.[81,83] AD is classically characterized by the accumulation of intracellular neurofibrillary tangles (NFTs) and

extracellular amyloid plaques in the brain.[82,83,84,85] According to the amyloid cascade hypothesis, amyloid beta (Aβ) can begin to deposit in the brain as early as 20 years before cognitive impairment, eventually forming toxic plaques that induce tau phosphorylation and neuronal death.[86,87,88,99] Specifically, Aβ peptides ending at position 42 (Aβ42) have been implicated as a precursor for amyloid plaque formation and AD pathology.[99,90,91] Neuropathological changes in Aβ42 concentration are detectable earlier in fluids like cerebrospinal fluid (CSF) and plasma than physiological changes in other portions of the brain, making fluid-based diagnostic techniques attractive for diagnosing preclinical AD.[85,87,90,91]

Current AD diagnostic techniques include amyloid PET scans, CSF assays, and other plasma-based assays that track the relative concentrations or presence of characteristic AD biomarkers like Aβ42, phosphorylated-Tau (p-Tau), and NFTs.[87] While amyloid PET scans have a high degree of selectivity and sensitivity for Aβ deposition in the brain, high costs and lack of widespread accessibility make them impractical for preclinical AD diagnosis or screening.[86,87] Similarly, CSF assays require a relatively invasive lumbar puncture procedure that can make sample collection more difficult than plasma-based alternatives.[86,87] This leaves plasma-based assays as a promising field of development for increasing diagnostic accessibility and prescreening capabilities for clinical trials. However, Aβ concentrations in plasma are 10-fold lower than those in CSF, and AD's neuropathological changes in Aβ42 concentration are much more minute within

plasma.[87,90,92] This means that in order for a plasma-based assay to be clinically useful, it must have a high degree of sensitivity or utilize a sufficiently large blood sample.[90,91]

Here, we demonstrate a high sensitivity method of detection and quantification for Aβ42 utilizing two antibody functionalized microparticles. Quantitative real-time polymerase chain reaction (qPCR) is used to detect the presence of the target after hybridization. The exponential amplification of the ssDNA tag during qPCR increases the sensitivity of this assay compared to traditional enzyme-linked immunosorbent assays (ELISA). qPCR is a method of quantification that is available in many labs and can be performed relatively quickly with minimal hands-on preparation.[92] This work builds upon previous studies to reduce the amount of hands-on time required for sample processing as well as explore alternative surface functionalization strategies.[93,94] The improved sensitivity of this assay compared to more traditional methods has the potential to be used for preclinical AD diagnosis with further testing.

2.3 Materials and Methods

2.3.1 Materials

Superparamagnetic streptavidin coated Dynabeads M-270® (2.8 um, 10 mg mL^{-1}), Taqman® MGB Probe and EZ-Link™ NHS-PEG4 Biotinylation Kit were purchased from Thermo Fisher. Human APP/Protease Nexin II (amyloid beta) antibodies, human amyloid beta (aa1-42) antibodies, and amyloid β-peptide (1-42) (human) were obtained from R&D Systems. The custom ssDNA template and primers were purchased from Millipore Sigma.

2.3.2 Antibody Biotinylation

The lyophilized antibodies were reconstituted in 1X phosphate buffered saline (PBS) to a concentration of 0.5 mg mL^{-1}. The NHS-PEG_4-Biotin was reconstituted to a 20mM concentration using nuclease-free water. A 20-fold molar excess of biotin was added to the antibodies and allowed to react at room temperature for 30 minutes. Excess biotin was removed using an Amicon Ultra-0.5 Centrifugal Filter Unit to remove the supernatant. The final antibody concentration was measured using a NanoDrop 1000.

2.3.3 Magnetic Capture Bead (MMP) Functionalization

3 mg of 2.8 µM superparamagnetic streptavidin coated Dynabeads M-270® (~1.3 x 10^8 beads) were manually washed three times with a wash buffer solution (1X PBS, 3% BSA, 0.01% Tween 20). After the final aspiration and wash, the solution was resuspended to a concentration of 5 mg mL^{-1} in PBS. Biotinylated Human APP/Protease Nexin II antibodies were then added in 1.5 times molar excess to the solution and incubated at room temperature for 45 minutes with end-over-end mixing. The functionalized magnetic microparticles (MMPs) were then washed with the wash buffer solution to remove excess antibodies. The MMPs were then blocked with a solution of 5 mg mL^{-1} of biotin to occupy any remaining streptavidin sites. Post blocking, the MMPs were washed three times with the wash buffer and resuspended to a final concentration of 11.5 mg mL^{-1} (~500,000 beads uL^{-1}).

2.3.4 Polystyrene Detection Bead (PSNP) Functionalization

0.2 mg of 200 nm streptavidin coated polystyrene beads (~1.56 x 10^9 beads) were cleaned with the wash buffer and centrifuged for 10 minutes at 13100 rpm three times. After washing, the solution was resuspended to 1 mg mL^{-1} in PBS. Biotinylated human Aβ42 antibody was then added to the solution and incubated at room temperature for 45 minutes with end-over-end mixing. The solution was centrifuged for 10 minutes at 13100 rpm, the supernatant removed, and resuspended as 4 mg mL^{-1} in PBS. Then, 5 µL of biotinylated ssDNA tag (50 uM) was added and the solution was incubated at room temperature for 20 minutes with end-over-end mixing before centrifugation and washed. The beads were then resuspended in a blocking solution with 5 mg mL^{-1} biotin and incubated again with end-over-end mixing for 45 minutes. Finally, the beads were centrifuged and washed three more times. The beads were treated with sonication in between each wash as needed to break up visible aggregation. The final concentration of the aliquoted beads was 6 ug mL^{-1} (~1,600,000 beads/uL).

2.3.5 Amyloid-beta (1-42) Preparation

Aβ42 was reconstituted using Tris buffer solution (50 mM) to a stock concentration of 3.3 x 10^6 pg mL^{-1}. Experimental samples were then prepared by diluting the stock solution of peptide to the desired concentration.

2.3.6 Assay Protocol

To begin, 20 µL of Aβ42 solution was diluted with 200 µL of sample diluent (1X PBS + 2% BSA + 0.01% Tween 20). Next, 3 µL of antibody-functionalized magnetic beads was added to the sample and incubated for 45 minutes at room temperature with end-over-end mixing. After incubation, the sample was aspirated once to remove any unbound protein and resuspended in 100 µL of sample diluent along with 170 µL of the dual-functionalized polystyrene beads. The sample was then incubated for another 30 minutes with end-over-end mixing to allow for hybridization and was subsequently washed 3 times with the wash buffer. This was followed by one "bead transfer" (Figure 2.1) to remove excess polystyrene beads before the cleaned beads were resuspended in 12 µL of nuclease-free water.

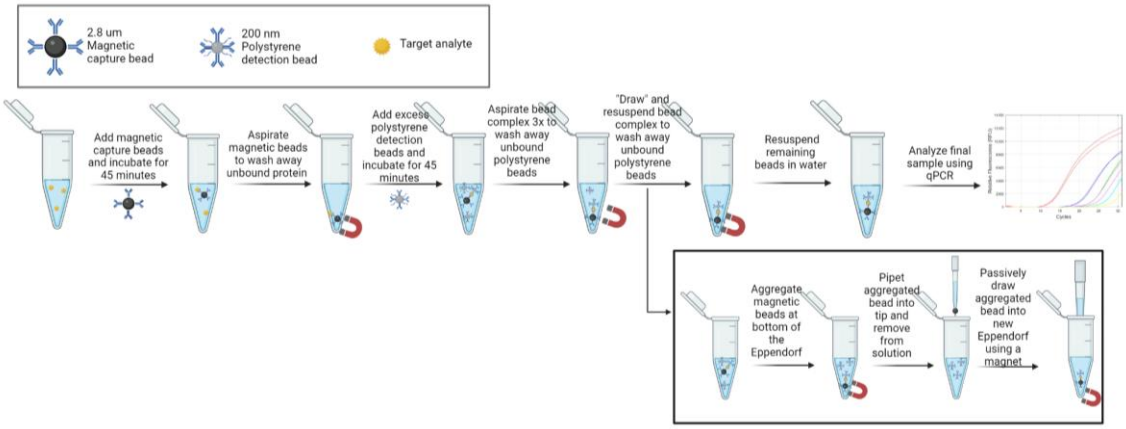

Figure 2.1 Detailed schematic of the dual-bead assay protocol. MBs and PSNPs are used to detect the presence of Aβ (1-42) by forming a sandwich complex around the target. qPCR is then performed on the resulting sandwich complex for analysis. **(**Created with BioRender.com)

2.3.7 Quantitative Real-Time Polymerase Chain Reaction Detection

The bead solution was transferred to a 384-well plate for real-time qPCR quantification using a CFX96 Touch Real-Time PCR Detection System (Bio-Rad Laboratories, Inc.,

Hercules, CA, United States). The primers, probes, and conditions used are given in Supplementary Table 2.1. The sample was run alongside a negative control and a dilution ladder of PSNPs to produce a standard curve for analysis.

2.4 Results and Discussion

2.4.1 DNA functionalization

In order to achieve the desired sensitivity, the amount of ssDNA per PSNP was optimized to produce a detectable signal around 0.01 pg mL^{-1} of Aβ (1-42). A noncoding DNA sequence of 85 base pairs was chosen as the amplicon and its dynamic range of amplification was observed to be between 0.15fM - 50pM of ssDNA. Serial dilutions of the biotinylated ssDNA tag were amplified using qPCR to optimize the amplification efficiency (Figure 2.2a). Once the optimal conditions were determined, they were applied to a 5X serial dilution of PSNPs to determine the amplification efficiency of the ssDNA when coupled to the PSNPs, as well as estimate the average amount of ssDNA per PSNP (Figure 2.2b). The dynamic range of both the free ssDNA tag and functionalized PSNPs was observed to cover four orders of magnitude. Since the cycle threshold number (Ct) is a function of the total amount of DNA per well, the average amount of ssDNA per PSNP could be estimated by dividing the reported concentration of DNA by the concentration of PSNPs. Approximately 10 strands of ssDNA per PSNP were observed. This is supported by the standard curve produced by the PSNPs (Figure 2.2b), in which the limit of detection was approximately 1200 beads mL^{-1} (12 beads per well).

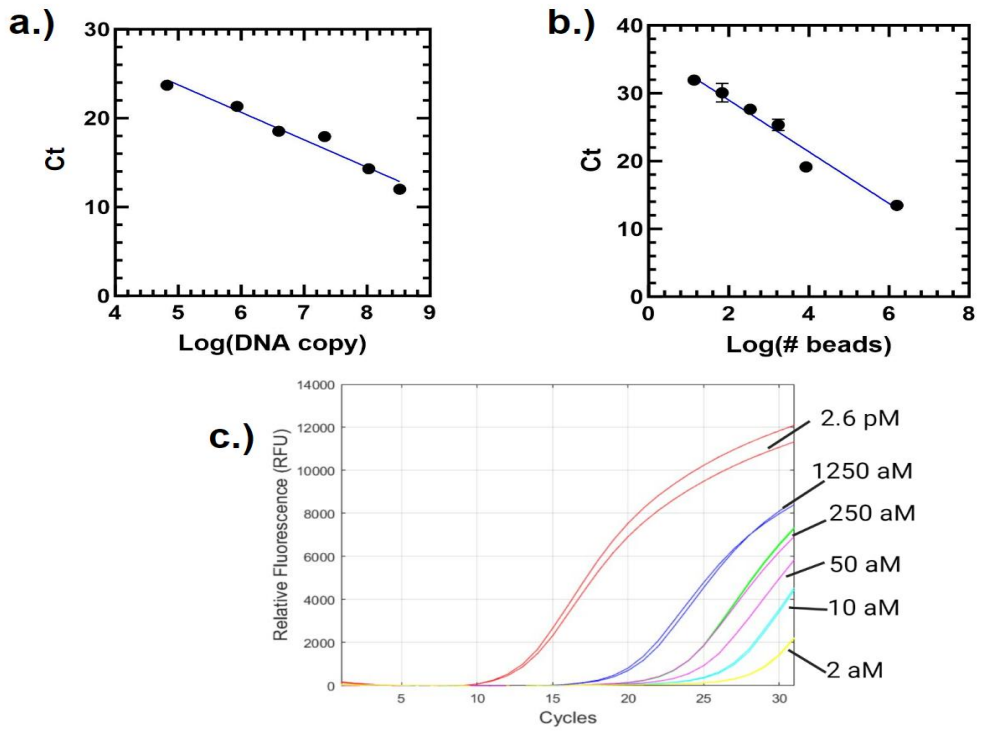

Figure 2.2 (a.) Standard qPCR curve of 1:5 ssDNA biotinylated tag dilutions in which amplification efficiency was calculated to be 103%. (b.) Standard qPCR curve of 1:5 PSNP dilutions in which the amplification efficiency was calculated to be 82.9% (c.) Representative qPCR amplification curves of the PSNP dilutions.

To avoid the process of decoupling the ssDNA from the PSNPs prior to qPCR, a mixture of PSNPs and MBs were run together in the same well to show that amplification is not impacted (Figure 2.3). There was no significant difference between PSNPs run by themselves and those mixed with MBs. Thus, the ssDNA tag did not need to be decoupled from the PSNP during the assay and qPCR could be performed directly on the beads. This also greatly reduced the total number of washing steps and time required to perform the assay when compared to similar methods previously published.[13] The total time required

to run this assay is about 3.5 hours (about 20 minutes of hands-on time and 3 hours of hands-off incubations).

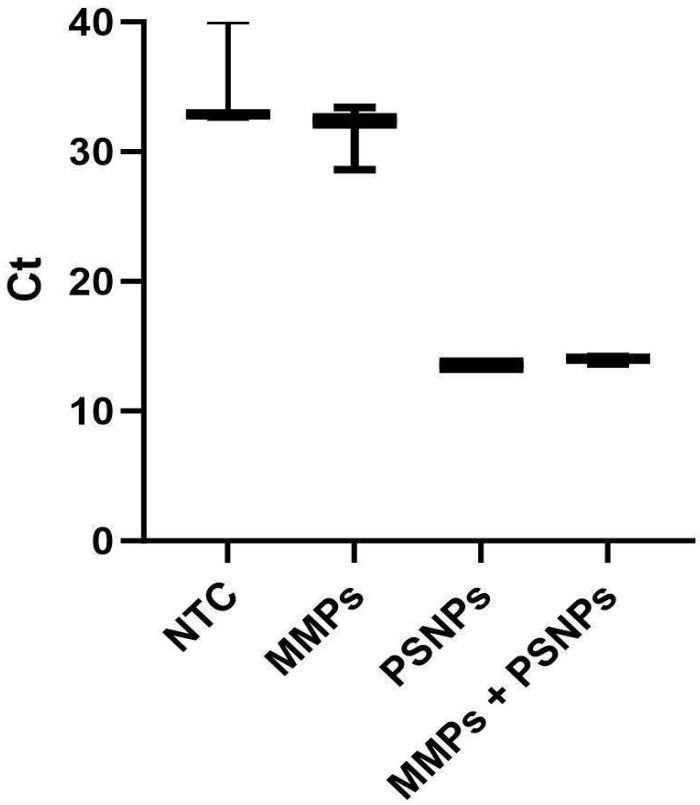

Figure 2.3 Reported cycle threshold values for 2 uL of MMPs and 10 uL of PSNPs to showcase that the presence of MMPs does impact the amplification of PSNPs (N = 3).

2.4.2 Antibody Functionalization and Surface Conjugation

A fundamental challenge of biosensor development is the efficient immobilization of an affinity probe to the sensor surface to enable target specific recognition. The method of probe immobilization impacts the coating density, functionality, stability, and overall sensitivity of the assay. As part of this work, two methods of biotin conjugation were investigated. The first method utilized NHS-PEG_4-Biotin to target primary amines present on lysine and the N-terminus of the protein. The NHS ester reacted with primary amines

to form irreversible amide bonds. This method was fast and efficient for labeling large quantities of antibodies. The hydrophilic PEG spacer arm increased the stability of the detection bead by imparting water solubility and reducing steric hindrance between antibodies. The spacer arm consists of 4 units of PEG for a total length of 29 angstroms. The decrease in Ct during qPCR (Figure 2.4) indicates greater DNA loading onto PSNPs as a result of the spacer arm. However, the nonspecific addition of biotin due to presence of multiple primary amines on the surface may have negatively impacted the functionality of the antibodies due to poor orientation or the presence of biotin in the binding region. The nonspecific addition of biotin also resulted in a higher background signal most likely due to excess biotin on the detection bead binding to open streptavidin sites on the MMP. This issue was resolved by blocking both beads with excess biotin post antibody conjugation (Figure 2.4).

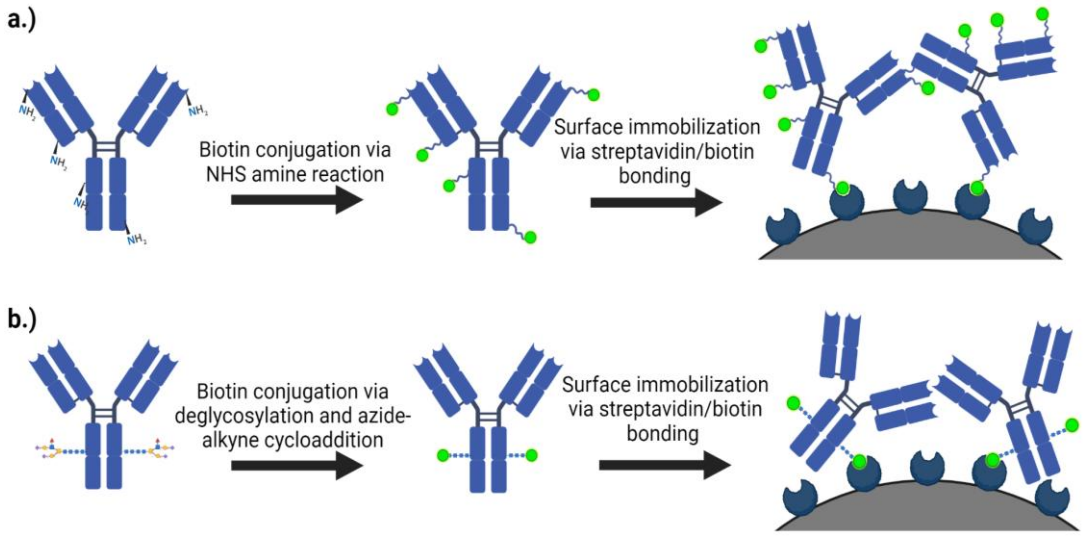

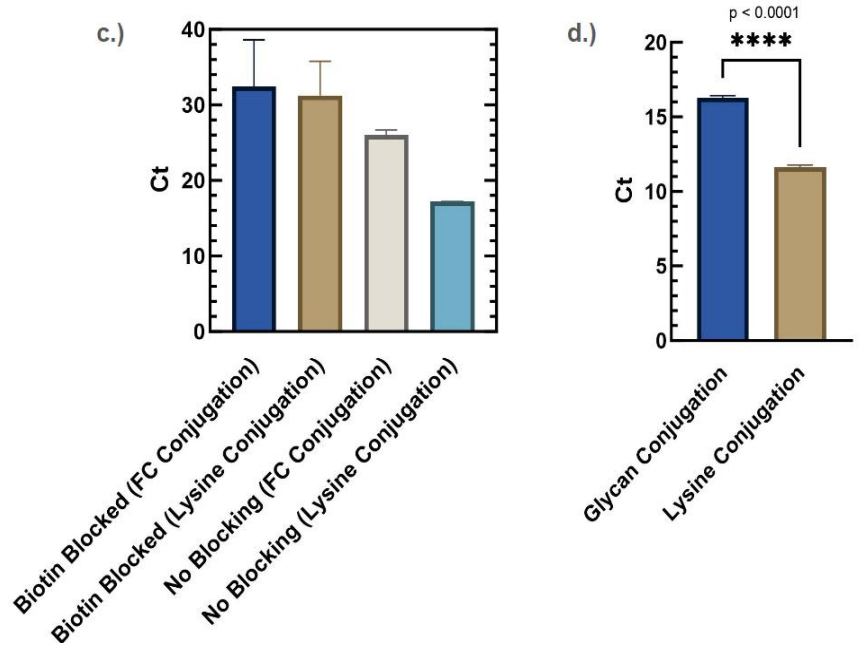

Figure 2.4 (a.) Schematic illustration of biotin conjugation targeting primary amines followed by addition to the particle surface.**(**Created with BioRender.com) b.) Schematic illustration of biotin conjugation targeting the Fc region of the antibody followed by addition to the particle surface.**(**Created with BioRender.com) c.) Cycle threshold values reported to evaluate the effect of antibody conjugation on background signal. PSNPs were mixed with MMPs and subsequently washed away. qPCR was then performed on the MMPs. PSNPs not blocked with biotin had lower Ct values and therefore produced a high background signal. Biotin blocked PSNPs had significantly reduced nonspecific interactions. (N = 3) d.) Cycle threshold values reported for 2 x 10^4 PSNPS conjugated using either lysine or glycan labeling. The lower Ct value for lysine indicates greater DNA packing. (N = 2)

In comparison, glycan modification was chosen as an alternative method of labeling due to its site-specific addition of biotin to the Fc region (Figure 2.4). Biotin was conjugated via complete enzymatic deglycosylation of the antibody, followed by an azide-alkyne cycloaddition. The Fc glycans were hydrolyzed using the Fc specific endoglycosidase (EndoS2) to open a region for the enzymatic addition of GalNaz. This generated an azide activated antibody that was then reacted with cyclooctyne-functionalized biotin for conjugation. The addition of biotin to the Fc region produced antibodies that were

immobilized onto the bead surface “tail on”.[15] This orientation resulted in a decrease in DNA loading (Figure 2.4) on the detection bead due to increased antibody packing. The biotin label did not include a PEG spacer arm to decrease steric hindrance. The addition of biotin to the Fc region likely did not impact the functionality of the antibody, as it is not near the antigen binding site. However, there was still a significant amount of nonspecific binding between the PSNPs and MMPs when coated using these antibodies. The background signal was significantly decreased by the addition of a biotin blocking step post bead conjugation - similar to the lysine modification. Due to the increase in DNA loading onto the lysine modified antibodies, this method was chosen moving forward. Both conjugation schemes resulted in a level of nonspecific bead interactions that were resolved by the inclusion of an additional blocking step. Lysine conjugation was easier to scale, more reproducible, and more cost effective.

2.4.3 Detection of amyloid-beta (1-42)

In order to have efficient labeling of the desired target, PSNPs were added in excess to ensure that each PSNP would form an immunocomplex with a single target.

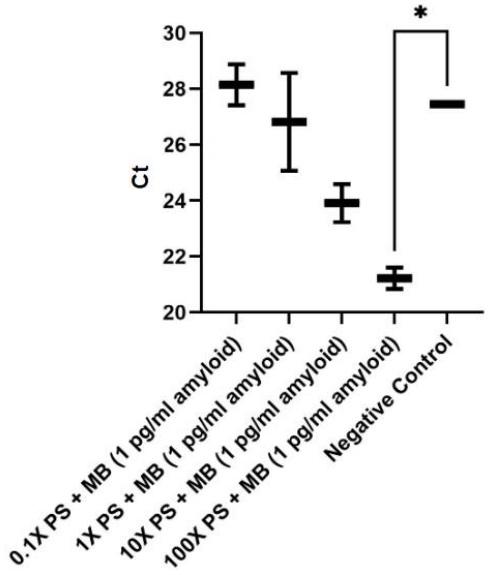

Figure 2.5. Reported cycle threshold values for the assay when 1 pg mL^{-1} of Aβ (1-42) was spiked into Tris buffer using increasing concentrations of PSNP for detection (N = 3).

The MMPs were washed prior to the addition of the PSNPs to reduce the matrix effect The dynamic range of this assay was determined by producing a calibration curve measuring synthetic Aβ (1-42) concentrations in Tris Buffer. The standard curve provides a dynamic range of four orders of magnitude. The lower limit of detection was established as 0.05 pg mL^{-1} using the following equation:[15]

$$Limit\ of\ Detection = \underline{x}_{blank} + 3.3\sigma_{blank} \qquad \textbf{Equation 2.1}$$

Where $\underline{x}_{blank}$ is the mean of blank and σ_{blank} is the standard deviation of the blank. At low concentrations, nonspecific amplification reduces the accuracy of the test and. At concentrations greater than 100 pg mL^{-1}, the signal stops responding linearly and plateaus. One explanation for the plateau, is that it is the result of multiple Aβ42 peptides binding to one PSNP. An alternative explanation would be that at high concentrations (> 100 pg mL^{-1}) the amount of DNA attached to the PSNPs to be amplified is outside of the qPCR exponential phase. If this is the case, then the DNA sequence on the PSNP could be

modified in future experiments in an effort to increase the dynamic range of quantification. This assay requires less time and is more sensitive than other experimental methods that have previously reported limits of detection only as low as 1 pg mL^{-1} of Aβ42.[96-102] Kits sold commercially have limits of detection of 4.73 and 1,000 pg mL^{-1}.[20] The increase in sensitivity is attributed to the exponential amplification of the ssDNA as well as increased binding kinetics. Bead-based assays exhibit similar reaction kinetics to solution-based reactions, as the probability of the microbead finding the target analyte is greater than in a planar assay.[103, 104] Slow diffusion kinetics are often the limiting factor for planar assays and result in long incubation periods.[105] Another distinct advantage of microbeads is their potential to advance the rapid multiplexed analysis of a wide variety of analytes.[104] Further work can be done to adapt this method to measure multiple target analytes in a single sample.

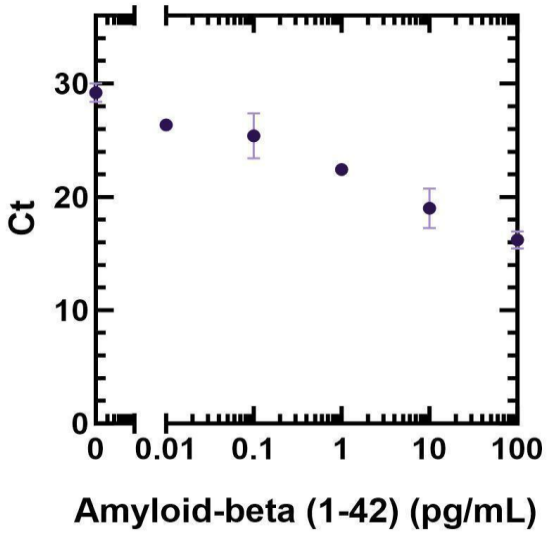

Figure 2.6 Recorded cycle threshold values for control Aβ42 analysis (technical replicates N = 3).

2.5 Binding Kinetics

The results described can be attributed to an increase in binding efficiency due to the utilization of magnetic and polystyrene beads carrying a large number of antibodies. Coupling beads with capture antibodies helps increase the capture efficiency due to increased diffusion, thus reduced incubation time. The magnetic beads were estimated to be covered with ~10^6 antibodies per bead using the following equation:

$$IgG = \frac{4\pi r^2}{25} \quad \textbf{Equation 2.2}$$

Where *r* is the bead radius (nm) and 25 is the estimated surface area of a single antibody. The polystyrene beads were estimated to carry ~5,000 antibodies when *r* is 100 nm. When the target protein comes into close proximity to the bead surface, the localized high density of antibodies drives equilibrium binding. Further, once the protein is bound, it is difficult for the protein to dissociate from the bead because of competition from surrounding antibodies.

The formation of the sandwich complex is a two step process that can be expressed as the following[107-108]:

$$MB + P \leftrightarrow MB - P \quad \textbf{Equation 2.3}$$

$$MB - P + PS \leftrightarrow MB - P - PS \quad \textbf{Equation 2.4}$$

In which, equation 3 describes the first incubation step where the analyte is captured by the MMP and equation 4 describes the second incubation where the detector binds to the magnetic bound analyte. It is assumed that both the analyte and detector are provided in

excess and the reaction is allowed to reach equilibrium. At equilibrium, all the time-derivatives of the rate equation are zero and the rate becomes directly proportional to the product of the concentrations of the reactants. This fundamental equation is known as the law-of-mass-action. The dissociation constant for each reaction can subsequently be written as[109,110]:

$$K_{D,1} = \frac{k_{off,1}}{k_{on,1}} = \frac{c_{MB}\ c_P}{c_{MB-P}} \quad \textbf{Equation 2.5}$$

$$K_{D,2} = \frac{k_{off,2}}{k_{on,2}} = \frac{c_{MB-P}\ c_{PS}}{c_{MB-P-PS}} \quad \textbf{Equation 2.6}$$

Where c is used to represent the molar concentration of each reactant in solution. The fraction of bound protein (f) is defined as the total number of occupied binding spots divided by the initial number of open binding spots (equation 7 and 8). It is a function of protein concentration and proportional to the output signal.

$$f(c_p) = \frac{n_{MB-P}}{n_{MB,0}} = \frac{c_P}{K_{D,1} + c_P} \quad \textbf{Equation 2.7}$$

$$f(c_{PS}) = \frac{n_{MB-P-PS}}{n_{MB-P}} = \frac{c_{PS}}{K_{D,2} + c_{PS}}\ \alpha\ \text{signal} \quad \textbf{Equation 2.8}$$

The signal becomes saturated at high concentrations of Aβ42 due to the surface of the MMPs becoming fully coated (Figure 2.7). At low concentrations, the fraction of occupied binding sites is less than 1% and would be difficult to detect using a traditional ELISA. The exponential amplification of the ssDNA tag enables increased sensitivity.

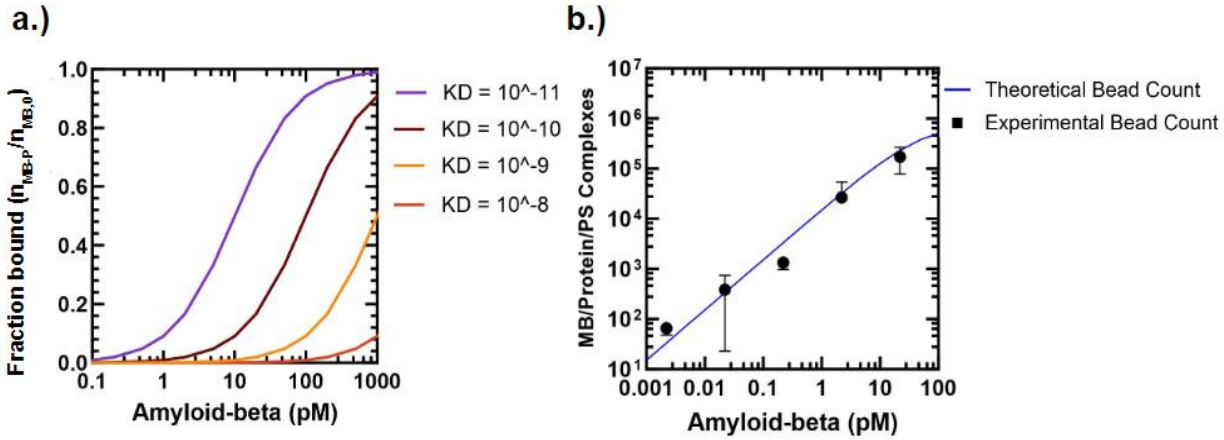

Figure 2.7 (a.) Theoretical fraction of occupied binding sites on MMPS as a function of protein concentration for a range of dissociation constants using equation 5. (b.) Total number of sandwich complexes formed as a function of protein concentration. The blue line represents the theoretical number of sandwich complexes formed assuming $K_D = 5 \times 10^{-11}$ M^{-1} for both reactions. ($R^2 = 0.936$)

The observed signal closely follows the predicted bead count assuming $K_D = 5 \times 10^{-11}$ M for both reactions. This supports that utilizing microbeads increases binding efficiency by overcoming diffusion limited kinetics typically experienced by planar assays.[111]

2.6 Conclusion

The method described here was optimized to detect concentrations of the peptide Aβ42 below 100 pg mL^{-1} in order to aid in the diagnosis of Alzheimer's disease. The lower limit of detection was determined to be 0.05 pg mL^{-1} and the assay dynamic range covered four orders of magnitude. A coating procedure using the streptavidin-biotin binding interaction was explored as a simple and quick method of bead functionalization, which was then further optimized to obtain the ideal ratio of antibody to ssDNA tag. The resulting immunocomplex was then quantified using qPCR without the need for decoupling the DNA from the PSNP.

Overall, this study is significant because it shows that high sensitivity immunoassays can be optimized to reduce the total amount of sample processing time required. The washing protocol utilized, reduces the total number of washes needed as well as the amount of nonspecific carryover. This protocol can be adapted to measure other proteins present in biofluids at low concentrations. In order to determine the accuracy and precision of this assay, it must be further tested using patient plasma samples.

2.7 Supplementary information

Table S2.1 DNA template, primers, and probe sequences used for qPCR.

Template	Sequence (5' - 3')	GC Content (%)	Melting Temperature
ssDNA tag	Biotin-TAGACGACCGAACCTTGGATCATGCTTCTGACACAGATTCTACAGCCTAGCGATTCTGGTAGTCATAGCGCGTAGTCAACTCGTA	48.2	71.1
Forward Primer	TAGACGACCGAACCTTGGA	52.63	62.18
Reverse Primer	GAGTTGACTACGCGCTATGAC	52.38	61.32
Taqman MGB Probe	TCTGACACAGATTCTACAGCCTAGCGA	48.15	67.98

Table S2.2 qPCR amplification protocol.

Step	Temperature (°C)	Time (s)
Polymerase Hot Start	90	30
Denaturing	90	20

Primer Annealing	59.5	30
Extension	72	30

Table S2.3 qPCR cycle threshold values forAβ42a quantification.

	Run 1 Reported Ct Value			Run 2 Reported Ct Value		Mean Ct	Standard Deviation	% CV
Amyloid Concentration (pg/mL)	Replicate 1	Replicate 2	Replicate 3	Replicate 1	Replicate 2			
0.00	29.40	28.33	29.89	30.11	30.15	29.58	0.677749216	2.291551
0.01	26.10	26.83	26.13	26.26	26.32	26.33	0.263772629	1.001871
0.10	24.70	25.44	N/A	24.58	24.64	24.84	0.348998567	1.404986
1.00	22.83	22.36	22.10	22.52	22.49	22.46	0.237065392	1.0555
10.00	20.25	20.30	N/A	20.29	20.26	20.28	0.020615528	0.10168
100.00	N/A	17.00	16.16	17.22	17.78	17.04	0.582237065	3.416884

	Run 1 Measured Concentration (pg/mL)			Run 2 Measured Concentration (pg/mL)		Mean Concentration (pg/mL)	Concentration Standard Deviation (pg/mL)	% CV
Amyloid Concentration (pg/mL)	Replicate 1	Replicate 2	Replicate 3	Replicate 1	Replicate 2			
0.00	0.00	0.00	0.00	0.00	0.00	0.00	0.00	101.76
0.01	0.02	0.01	0.02	0.01	0.01	0.01	0.00	26.67
0.10	0.08	0.03	N/A	0.09	0.08	0.07	0.02	34.25
1.00	0.57	0.94	1.24	0.79	0.81	0.87	0.25	28.32
10.00	9.00	8.53	N/A	8.62	8.91	8.77	0.22	2.55
100.00	N/A	294.29	724.76	232.41	127.44	344.72	262.55	76.16

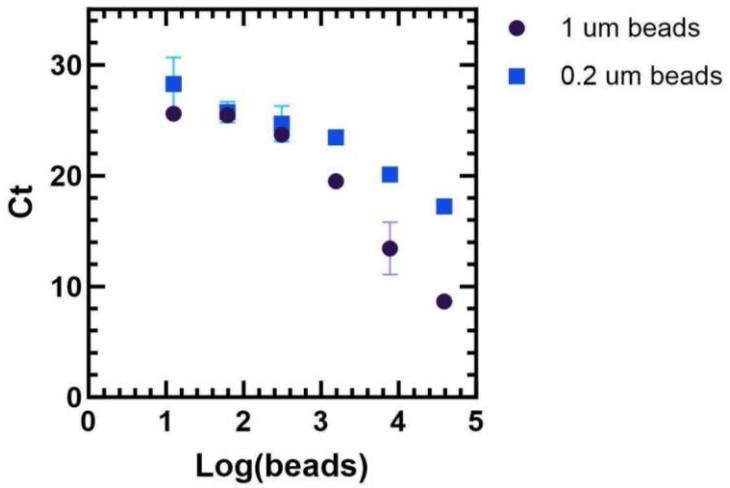

Figure S2.1 Reported cycle threshold values for 1 µm and 0.2 µm PSNPs coated with antibodies and ssDNA.

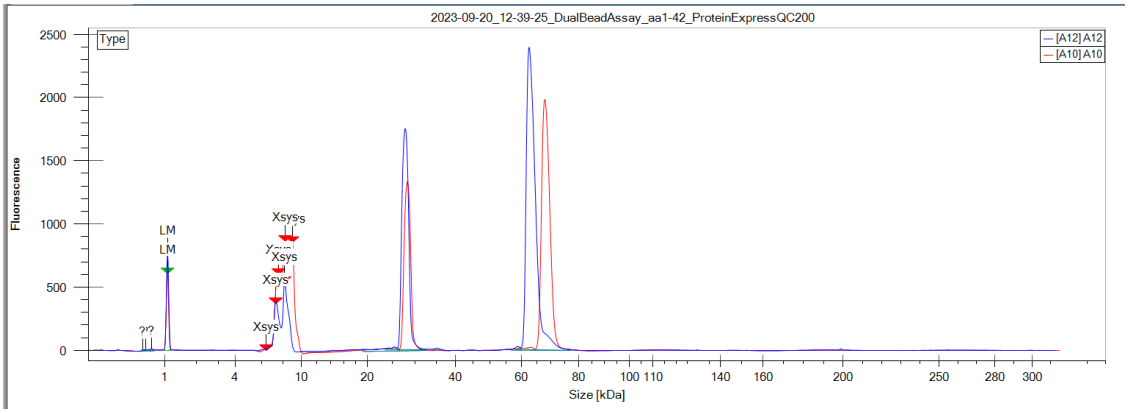

Figure S2.2 Electropherogram displaying the change in molecular mass of the capture antibody as a result of glycan modification. The red is the pre-conjugation normal antibody and the blue is the post-conjugation biotinylated antibody. The molecular weight of the heavy chain decreased slightly due to cleavage of the Fc glycans.

2.8 Acknowledgements

We gratefully acknowledge Quanterix Corporation and extend our appreciation to Kishore Malyavantham for sharing concept details and materials that enabled the progress of our research.

CHAPTER 3:

A High-Sensitivity Digital Framework for the Standardized Quantification of Intact Extracellular Vesicles in Complex Biofluids

---

Chapter 3 has been submitted as an original research article and is currently under review.

Jennifer M. Pollock[1], Connor H. Yew[1], Everett Gutterman-Johns[1], Julia Miller[1], Anji Friedbauer[1], Kishore Malyavantham[2], and Anubhav Tripathi[1]

1. Center for Biomedical Engineering, School of Engineering, Brown University, Providence, RI, USA

2. Quanterix Inc, Billerica, MA, USA

3.1 Abstract

Extracellular vesicles (EVs) hold great potential as liquid biopsy biomarkers, yet their clinical translation has been hindered by the lack of sensitive, standardized quantification methods that bypass the need for tedious pre-isolation. This study describes the development and validation of a digital Single Molecule Array (SiMoA) assay for the direct and robust detection of intact EVs in complex matrices, including human plasma and serum. A primary challenge in adapting digital ELISA for EVs is their large size and polyvalency, which potentially violates Poisson distribution assumptions fundamental to digital quantification. We overcame this critical limitation by evaluating a continuous mathematical model for Average Enzymes per Bead (AEB) determination. By employing a piecewise function that combines digital and analog measurements successfully maintained a dynamic range over four orders of magnitude, confirming that EV polyvalency does not compromise digital logic at low concentrations. We evaluated 12 assay configurations targeting the tetraspanins CD9, CD63, and CD81, achieving a low limit of detection of 1.61 x 10^7 EVs/mL. Results indicated that CD9-based detection offered superior sensitivity, reflecting its higher surface density in serum-derived EVs. In a proof-of-concept study for oncology, we compared EV expression from breast cancer and healthy patient serum. While CD9 levels remained stable, CD63 expression was elevated in cancer samples, highlighting the platform's utility for phenotypic profiling of tumor-associated subpopulations. The assay's specificity for intact vesicles was confirmed through membrane lysis and protease degradation studies. Furthermore, the SiMoA platform demonstrated superior performance compared to commercial MSD R-plex assays,

exhibiting higher inter-plate reproducibility and consistent limits of detection essential traits for longitudinal clinical monitoring. This framework provides a scalable, high-throughput solution for EV-based diagnostics, offering a more nuanced tool for early disease detection and treatment monitoring. Ultimately, we hope our work can help shift the paradigm of EV diagnostics from isolation to direct profiling.

3.2 Introduction

Extracellular vesicles (EVs) have been recognized increasingly more over the past few years as key mediators of intercellular communication. Previously often dismissed as waste or cellular debris, EVs have shown themselves to play important roles in important physiological and pathological processes. The Minimal Information Studies for Extracellular Vesicles (MISEV) 2023 defines EVs as small, nano- and microparticles delimited by a lipid bilayer that carry bioactive cargo.[39] They are an extremely heterogeneous population that varies in size, origin, and composition. Their size ranges from 50 nm to 10 μm. EVs are excreted by most cells and can be found in a wide variety of biofluids such as blood, saliva, cerebral spinal fluid, urine, and ascitic fluid.[112,113] In Alzheimer's disease, EVs have been found to carry neurotoxins and contribute to the propagation of the disease. Due to their ability to also cross the blood-brain-barrier, there is high potential for their use as an effective biomarker for dementia and other CNS diseases.[114]

Additionally, tumor-derived EVs (tEVs) have also been found to play a pivotal role in the creation of the tumor microenvironment, promotion of angiogenesis, and contributing to

metastasis in distant organs.[115] Unlike circulating tumor cells, tEVs can be found in high abundance in even early stages of cancer. Elevated levels of EVs, particularly $CD63^+$ EVs, have been found to be good indicators of disease.[116,117]

However, despite their immense potential, the clinical translation of EV-based diagnostics is currently hindered by the limitations of traditional isolation and quantification methods. Standard techniques often struggle to balance purity, yield, speed, and reproducibility.[118,119] Traditional plate-based ELISAs lack the sensitivity to detect low concentrations of EVs in biospecimens without pre-isolating EVs. Methods like NTA cannot easily distinguish between EVs and non-vesicular particles in complex fluids; nanoFCM requires extensive expertise and calibration; SP-IRIS is powerful but can be lower throughput and expensive.[120,121] Bias and lack of reproducible results caused by heterogeneous isolation methods (e.g., ultracentrifugation vs. size exclusion chromatography) has shifted the goal away from isolation and toward direct profiling in complex biofluids.

In this study, we present a robust, high-throughout immunoassay utilizing single molecular array (SiMoA) technology for the direct detection and quantification of EVs in biospecimens (Figure 3.1). The high sensitivity of SiMoA technology is used to overcome such limitations by minimizing the amount of material required and avoiding the need for extensive sample concentration and pretreatment. The assay is dependent on the colocalization of tetraspanins - or other EV surface markers - to detect whole EVs. SiMoA technology is a digital bead based assay that loads antibody labeled microbeads into

femtoliter-sized microwells for imaging. Microscopic bead-analyte-detector complexes, along with a fluorogenic substrate, are loaded into the microwells and imaged over time to measure the enzymatic activity. While SiMoA has revolutionized soluble protein biomarker detection, adapting it for large, multivalent lipid vesicles presents entirely unique physical and chemical challenges.[122] Our work successfully re-engineers the SiMoA paradigm (which was built for single, small protein analytes) to accommodate large (50-1000 nm), heterogeneous nanoparticles with multiple binding sites.

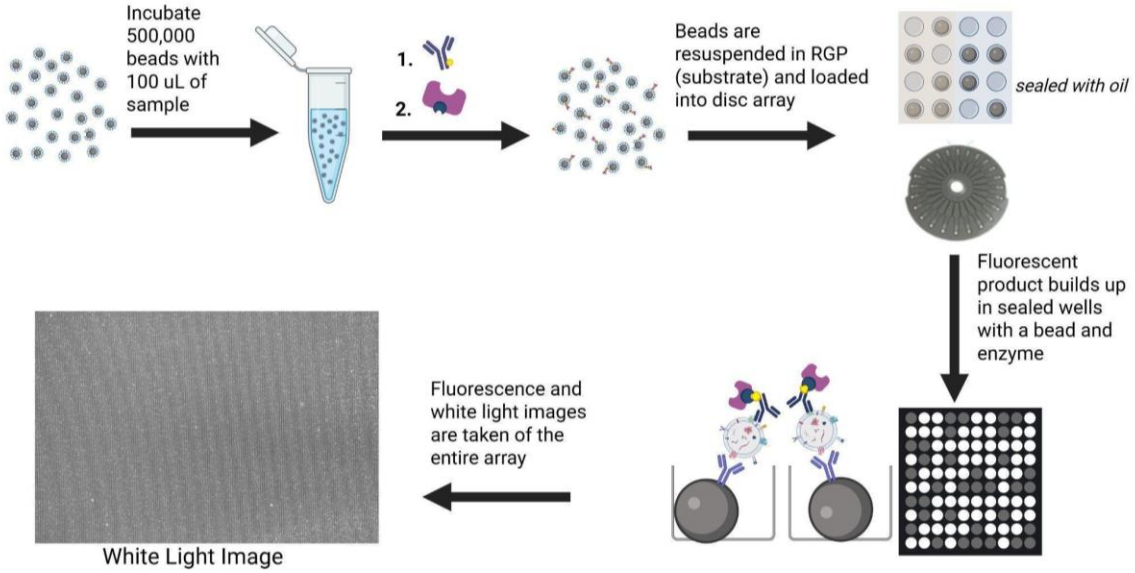

Figure 3.1 Single Molecular Array (SiMoA) Workflow (Image created with Biorender.com)

AEB was first reported in 2010, based on the work of Walt *et al.,* to report the concentration of Prostate specific-antigen (PSA) in blood. Poisson statistics are used to determine analyte concentration by observing the presence or absence of fluorescent products in each microwell. The fraction of "on" microwells is correlated to bulk enzyme

concentration. This binary readout method proved that enzyme catalysis amplifies the signal sufficiently at low concentrations to provide high-sensitivity detection without the need for actual single molecule detection.[123] We investigated the use of similar microarrays to develop an ultrasensitive assay to quantify the presence of extracellular vesicles in biofluids. The two main challenges associated with EV detection are, first, ensuring that the assay measures whole EVs and not free-floating protein. The second challenge is reducing nonspecific binding of EVs to surfaces to prevent false positives. This issue is fixed by utilizing a 3-step assay configuration and utilizing a passivated surface.

For general quantification of EVs, we utilized the three major EV tetraspanins CD9, CD63, and CD81, to develop a configurable, ultrasensitive digital ELISA. Due to the ability of EVs to express multiple tetraspanin molecules on the surface, even including multiple of the same protein, homogeneous and heterogeneous assay configurations could be used for capture and detection. Homogeneous configurations utilize the same antibody for capture and detection (i.e. CD9 capture and CD9 detection). Heterogeneous assays utilize a different target for capture and detection (i.e. CD9 capture and CD63 detection). The final EV immunoassay presented has a total of 16 total potential combinations with the potential for even more future combinations. Here we report the development and performance of a SiMoA assay for the quantification of whole EVs in biofluids using common EV surface markers - CD9, CD63, and CD81. This assay has the potential to reduce costs, save sample volume, and reduce the time to answer for EV measurement. The field currently struggles to map EV subpopulations, by offering a 16-combination matrix, our new assay allows

researchers to rapidly profile the surface "fingerprint" of EVs in a biofluid, which is transformative for discovering novel biomarker signatures in oncology and neurology.

3.3 Materials and Methods

3.3.1 Bead Conjugation

Simoa 488nm Homebrew Beads (Catalog #104006) were conjugated with monoclonal antibodies for each marker listed in Table 1. Briefly, beads were conjugated using 1-ethyl-3-(3-dimethylaminopropyl) carbodiimide (EDC) chemistry. The bead surface was activated with EDC/NHS prior to the addition of the antibody solution. The antibody coating efficiency was determined utilizing UV-vis (NanoDrop ND-1000 Spectrophotometer) to measure the antibody content in solution pre and post-isolation. After conjugation, the bead surface was further passivated using Bead Blocking Buffer (Quanterix Cat#101356) for 1 hour at room temperature.

3.3.2 SiMoA EV Assay

All calibration curves and parallelism studies were performed on the Quanterix Simoa HD-X. A custom 3-step assay definition was created for analysis. The first bead incubation step was 30 minutes, followed by 20 minute detector incubation, and a 10 minute incubation with streptavidin beta-galactosidase (SBG) reagent. Samples were diluted on the bench using EV sample diluent prior to running the assay. All bead stocks were resuspended with over-end mixing for 1 hour prior to being loaded onto the reagent bay.

Human female normal and breast cancer serum samples were obtained commercially (BioIVT Cat#HUMANSRM-0004591). Samples were held at -80°C until testing. On the day of testing, serum was thawed in a 37°C water bath and then centrifuged for 10,000g x 5 minutes to remove debris. Each sample was then diluted 4X in EV sample diluent. Analysis was performed using a 2-step assay on the Quanterix SR-X. Samples were incubated for 45 minutes with 20 µL of detector and 25 uL of beads. The resulting pellet was washed on a 96-well microplate washer. The aspirated bead pellets were then resuspended with 100 µL of SBG reagent and incubated for 5 minutes. The bead immuno-complexes were then subsequently washed and fully aspirated on the plate washer prior to analysis.

3.3.3 Immunoaffinity Isolation

EDTA plasma and cell media was thawed in a 37ºC water bath and centrifuged for 10,000g x 5 mins to remove debris. 1 mL aliquots were then made and beads were added at the indicated volumes. Samples were then incubated overnight with over-end mixing for 18 hours. The beads were washed three times with 1mL of 1X PBS + 0.01% Tween-20. EVs were eluted with 0.1M Glycine HCl (pH = 2.5) by incubating at 40°C for 40 minutes with mixing at 1000rpm.

3.3.4 Ultracentrifugation

To begin, pooled serum or plasma (BioIVT Cat#HUMANSRM-9982-T and Cat#HUMANPLK2-9914-R) was thawed in a 37°C water bath. Next, 15 mL aliquots of

plasma/serum were centrifuged at 300xg for 10 minutes at 4ºC. The supernatant was collected and transferred to sterile protein lo-bind tubes, where it was diluted with 1X PBS, before being spun for 30 minutes at 10,000g, with no brake during deceleration. The supernatant was removed and the pellet was resuspended in 1X PBS. The solution was then centrifuged at 100,000xg for 2 hours. Following the 100k centrifugation, the pellet was resuspended in 250 µL of cold PBS and stored at -20ºC until use.

3.3.5 Protease K Treatment

First, 1 mL aliquots of plasma were centrifuged for 10,000g x 5 minutes to clear debris. Next, 500 µL of plasma was aliquoted into sterile protein lo-bind tubes and 20 µL of protease K (Thermofisher Cat#EO0491) was added to a final concentration of 2 mg/mL. The protease K was left to digest proteins for 40 minutes at 37ºC. After the incubation period, the plasma was heated to 95ºC for 15 minutes to inhibit the protease k activity. The sample was then diluted 4-fold prior to analysis.

3.3.6 Trypsin Treatment

Thawed normal plasma was centrifuged for 10,000g x 5 minutes to clear debris and then aliquoted into sterile protein lo-bind tubes. 25 µL of trypsin (Thermofisher Cat#25200056) was added to 100 µL of plasma and incubated at room temperature for 40 minutes. Post incubation, 2.5 µL of protease inhibitor (Thermofisher Cat#78429) was added to inhibit the trypsin activity. The plasma was then diluted 4-fold prior to analysis.

3.3.7 Glioblastoma Spheroid Culture and EV Collection

The primary human glioblastoma cells were obtained following surgical removal from patient brain tumors at the Rhode Island Hospital under Institutional Review Board IRB #418015. The isolated cells were placed in non- coated 60 mm dishes at an initial seeding density of 1 million cells per dish and allowed to form spheroids. The conditioned media was harvested after 5 days of growth and EVs were subsequently isolated via ultracentrifugation. The cell media created for culturing was serum-free and consisted of 1× Neurobasal A, 2 mM GlutaMAX-I, 100X Antibiotic-Antimycotic, 20 ng/mL bFGF and EGF, B-27-A, and heparin.

3.3.8 Data Analysis

All data analysis and curve fitting was performed using GraphPad Prism (ver 10.0.2). For the comparison of breast cancer and normal serum AEB values, an unpaired t-test was performed to determine statistical significance.

3.4 Results and Discussion

3.4.1 Calculating Average Enzymes Per Bead (AEB)

Analyte concentration is determined by the average number of enzymes per bead (AEB) when performing a digital ELISA utilizing Quanterix's HD-X and SR-X. AEB is calculated using the following equations, assuming that analyte binding follows a Poisson distribution:[63]

$$AEB_{digital} = -\ln(1 - f_{on}) \quad \textbf{Equation 3.1}$$

$$AEB_{analog} = \frac{f_{on} \cdot \underline{I}_{bead}}{\underline{I}_{single}} \quad \textbf{Equation 3.2}$$

Where f_{on} is the fraction of on beads loaded into the array $\underline{I}_{bead}$ is the increase in fluorescent intensity that is a product of the enzyme-substrate interactions averaged across all beads, and $\underline{I}_{single}$ is the average growth in fluorescent intensity of a single enzyme. Arrays with $f_{on} < 0.2$ are used to calculate $\underline{I}_{single}$.[63]

$$\underline{I}_{single} = \sum_i \left(\frac{N_i}{N_{total}} \cdot \frac{f_{on,i} \cdot \underline{I}_{bead,i}}{-\ln(1 - f_{on,i})} \right) \quad f_{on,i} < 0.2 \quad \textbf{Equation 3.3}$$

It is assumed that due to the excess of capture beads at low analyte concentration, the capture of one analyte onto a bead is independent of another bead. When the fraction of on wells is low, there is generally only a single enzyme per bead and equation 2 approaches the value of equation 1. In a well mixed, poisson compliant system AEB_{analog} is a digital parameter for $f_{on} < 0.7$. The value of AEB can therefore be written as a piecewise function:[63]

$$AEB_{piecewise} = \begin{cases} AEB_{digital} = -\ln(1 - f_{on}) & f_{on} \leq 0.7 \\ AEB_{analog} = \frac{f_{on} \cdot \bar{I}_{bead}}{\bar{I}_{single}} & f_{on} > 0.7 \end{cases} \quad \textbf{Equation 3.4}$$

This assumption was tested for the quantification of EVs, which are larger than the typical analytes measured with SiMoA technology and often contain multiple potential binding sites per vesicle.[124] Such characteristics can potentially contribute to non-Poisson behavior and ultimately result in AEB discontinuity. AEB discontinuity has been observed in the past when measuring proteins prone to aggregation. While the calibration curve performed on each run helps account for such inconsistencies, AEB discontinuity can make inter-experiment comparisons difficult. Samples that may exhibit an AEB around 0.7 would be most affected. In general, non-Poisson compliant behavior can result in unwanted lot-to-lot variations that are undesirable for clinical application. One solution to account for AEB discontinuity is to instead calculate it continuously based on the weighted contributions of the digital and analog measurements:[63]

$$AEB_{continuous} = wAEB_{digital} + (1 - w)\cdot AEB_{analog} \quad \textbf{Equation 3.5}$$

$$w = \frac{(1 - f_{on})^2}{(1 - f_{on})^2 + f_{on}^{6.75}} \quad \textbf{Equation 3.6}$$

A comparison of how equations 1, 2 and 5 perform when measuring plasma derived EVs using CD9 capture and detection is shown in Figure 3.2. We observed that under optimized assay conditions (Supplementary Figures S3.1 - S3.3), AEB can be calculated using the piecewise function described by equation 4. As predicted, the digital and analog AEBs were not significantly different at low f_{on}. When f_{on} exceeded 0.7, the two values began to diverge and AEB_{analog} exhibited an increase in the linear region of quantification at high concentrations. Meanwhile, $AEB_{digital}$ exhibited an increase in sensitivity over AEB_{analog} at

low concentrations. The large size and presence of multiple binding proteins on the surface do not appear to hinder the ability of the assay to accurately measure EVs in solution. The piecewise combination of analog and digital measurements led to an increase in sensitivity and extended the dynamic range of the assay over 4 orders of magnitude.

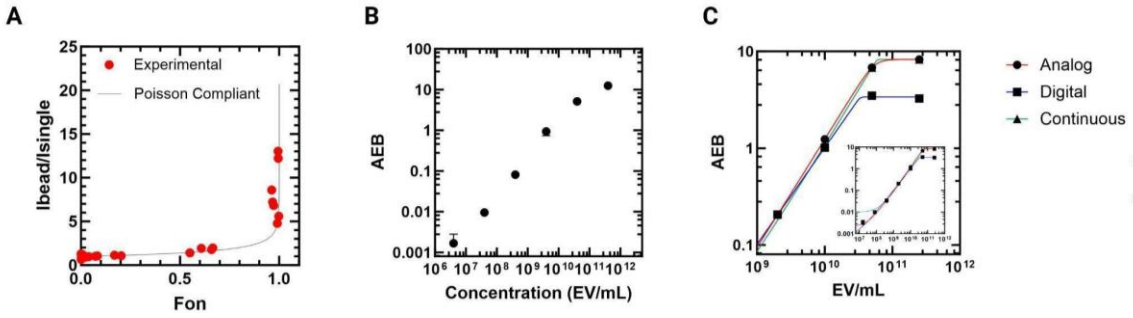

Figure 3.2 (A) Plot of $\frac{I_{bead}}{I_{single}}$ as a function of f_{on}. exhibiting Poisson compliant behavior of CD9 capture and detection assay. (B) Calibration curve for plasma EV quantification using AEB calculated as a piecewise function (equation 4) for the CD9 capture and detection assay. (C) Plot of AEBs calculated using equations 1, 2 and 5 for plasma derived EVs.

The calibration curve produced using the piecewise calculation of AEB for plasma derived EVs was fitted using a 4PL logistic regression curve model and the limit of detection was calculated by adding the signal of negative control plus 2.5 times the standard deviation. The limit of detection for the piecewise calculation of AEB was determined to be 2.95 x $10^7 \frac{EV}{mL}$ (Figure 3.2B).

3.4.2 Digital Detection of EVs Utilizing Single Molecular Array Technology (SiMoA)

The first challenge for developing an assay to target whole EVs is obtaining a good quality source of concentrated, purified EVs. In order to achieve the most accurate quantification

of total EVs in serum, we chose to isolate EVs from pooled human serum via ultracentrifugation to produce a concentrated pellet of EVs for calibration. The final yield and concentration were verified using NTA prior to dilution for the assay (Figure 3.3). Ultracentrifugation is the current gold standard for EV isolation, as it provides a good balance of purity, yield, and volume.[125] Though it can co-isolate some lipoproteins, such as high-density lipoproteins (HDLs), that have a similar density.[126] The presence of that may affect the accuracy of the final EV concentration measured using NTA. The average size distribution of the EVs isolated and used for experiments was 131.2 +/- 99.8 nm.

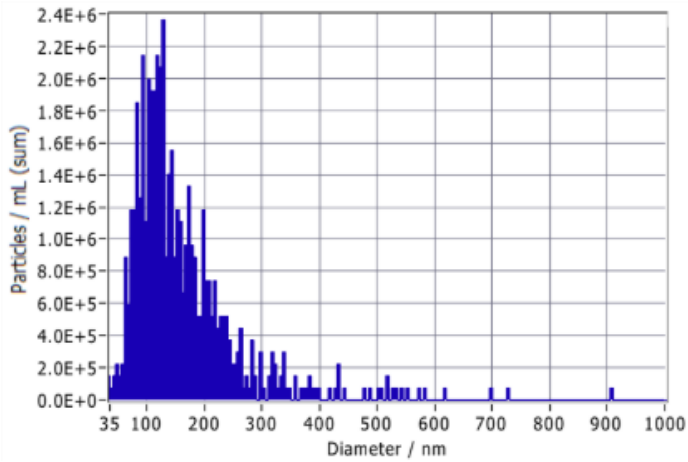

Figure 3.3 Nanoparticle tracking analysis results for serum EVs isolated via ultracentrifugation using Malvern ZetaView. EVs were used as standards for the SiMoA EV quantification assay.

Capture beads were produced by utilizing EDC/SNHS click chemistry to conjugate CD9, CD63, CD81, IgG control capture antibodies listed in Table 1 to the surface on Quanterix Simoa Homebrew Beads. Antibody coating efficiency was calculated using UV-Vis spectrophotometry at 280 nm to measure the protein concentration before and after

conjugation (Table S1). The conjugated capture beads were mixed with surface passivated helper beads (Quanterix Cat #103208) at a ratio of 1:3. All detector antibodies were purchased pre-biotinylated.

We also then chose to select antibody pairs suitable for capture and detection. Because the assay was designed to measure the concentration of natural, intact EVs present in a sample, we chose to utilize conformational binding antibodies. Each clone recognizes the three-dimensional structure produced by the tetraspanin when it is present in the membrane of a vesicle. Specifically, each antibody recognizes the EC2 domain, the large extracellular loop, of each tetraspanin. Two clones for each marker were selected - one for capture and one for detection (Table 3.1).

Table 3.1 Capture and detection antibodies used for the assay.

Antigen	**Vendor**	**Usage**	**Cat. No.**	**Host/isotype**	**Species Specificity**
CD9	Abcam	Capture	ab58989	Murine IgG1 kappa	human
Biotin-CD9	Ancell	Detector	156-030	Murine IgG1 kappa	human
CD63	Abcam	Capture	ab59479	Murine IgG1 kappa	human
Biotin-CD63	Ancell	Detector	215-030	Murine IgG1	human
CD81	Abcam	Capture	ab59477	Murine IgG2a kappa	human
Biotin-CD81	Ancell	Detector	302-030	Murine IgG1	human
Mouse IgG	Abcam	Capture	ab37355	Murine Polyclonal IgG	-

The resulting calibration curves are shown in Figure 3.4A - D. The lowest limit of detection was determined to be 1.61 x 10^7 EVs/mL utilizing CD63 capture and CD9 detection (Table S3.1). CD9 detection consistently achieved around one order of magnitude greater sensitivity than CD63 and CD81 across all assay configurations. The significant increase in sensitivity when utilizing CD9 as a detector is most likely due to its higher rate of expression compared to the other markers. In contrast, CD63 detection was the least sensitive of the three detectors. It consistently scored as the least sensitive detector for every capture bead. This supports previous reports of CD63 being a poor choice for general EV detection in immunoaffinity assays.[127,128] For total EV quantification we recommend utilizing either CD9 and a pantetraspanin cocktail to obtain the highest sensitivity. Alternative configurations may be better suited for disease or tissue specific applications.

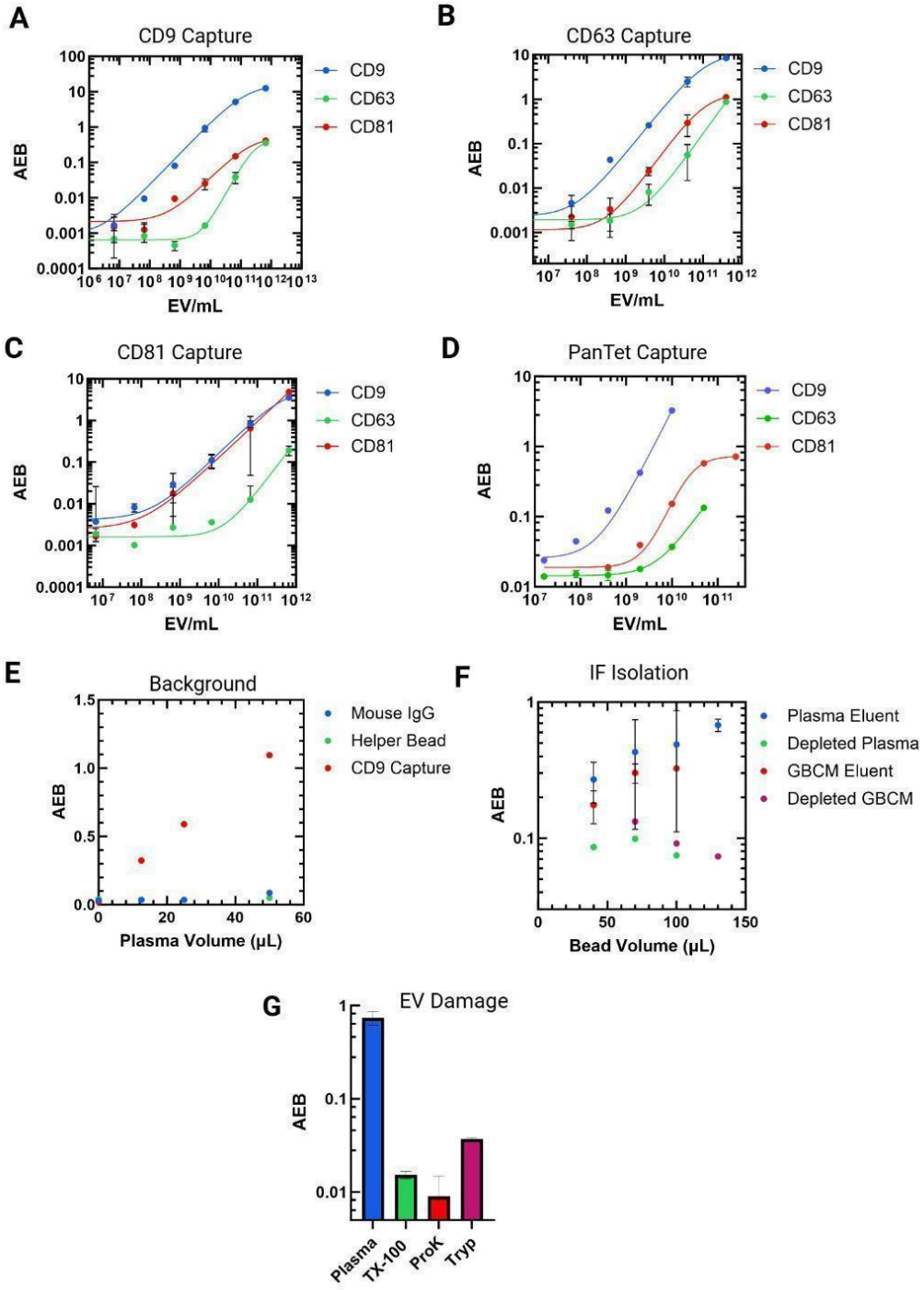

Figure 3.4 AEB calibration curves produced using EVs isolated from pooled normal serum for (A) CD9 capture beads, (B) CD63 capture bead, (C) CD81 capture beads, and (D) PanTet (mixture of CD9, CD63, and CD81) capture beads. (E) No significant nonspecific binding was observed on helper beads or the mouse IgG isotype control when normal

plasma was run against a PanTet detector. (F) CD9 beads prepared for the assay were shown to also be effective at depleting plasma and cell media of EVs when performing immunoaffinity (IF). AEB was measured for the resulting eluent and depleted medium using the homogeneous CD9 assay. (G) Plasma EVs damaged with 1% Triton X-100, Protease K, and trypsin were tested against PanTet capture and detection. No significant signal was observed when EVs were damaged.

Nonspecific binding and background signal were tested by analyzing the AEB produced on surface passivated helper beads and IgG control conjugated beads against a PanTet detector. Both controls did not have a significant dosage response to EDTA plasma (Figure 3.4E), unlike CD9 capture beads which produced a significant dosage response. These results support the conclusion that there is minimal nonspecific binding of EVs or detectors to the bead surface.

We performed immunoaffinity EV depletion in plasma and serum-free conditioned media (patient derived glioblastoma cells) using CD9 capture beads (Figure 3.4F). The volume of beads added to 1 mL of plasma and media was titrated to determine the minimum concentration of beads required to efficiently isolate most EVs. We found that a volume of 130 μL (1.3×10^8 beads/mL) was the most effective for overnight isolation from 1 mL of solution. EVs were then eluted off of the beads, and the resulting eluent and depleted supernatant were measured using the SiMoA assay. Post incubation, both plasma and conditioned media showed a significant reduction in CD9 signal. The eluent was found to contain a significant number of isolated EVs that were confirmed using both SiMoA and NTA. A negative control bead coated with mouse IgG was used alongside to confirm that the depletion was not purely due to non-specific binding to the bead matrix.

We also tested specificity for intact EVs by running the assay against damaged EVs. Plasma was treated with either 1% Triton X-100 to lyse EVs, protease K, or trypsin for 40 minutes. Protease K and trypsin were used to cleave peptide bonds of surface exposed proteins. The EV membrane therefore remained intact, but the exposed surface proteins, like tetraspanins, were broken down. The plasma was then diluted 4X with sample diluent and AEB was measured using PanTet capture and detection. Damaged EVs showed a significant decrease in AEB compared to untreated plasma (Figure 3.4G).

3.4.3 Parallelism, Linearity, and Recovery in Plasma and Serum

We determined the dynamic range and robustness of the assay in EDTA plasma and serum by performing serial dilutions across multiple samples to assess the linearity of the response. All samples were run in duplicate and the standard deviation is reported (Tables 2 and 3). EVs in plasma and serum showcased linearity across at least an 8-fold dilution series. Plasma and serum samples exhibited a linear response between 2-fold and 8-fold dilutions (Figures 3.5 and 3.6). The coefficient of variation among these samples was on average 13%. These results suggest that the recommended dilution factor for plasma and serum is 4X, as it typically establishes most samples in the middle of the assay's dynamic range.

Additionally, normal serum samples were spiked with three levels of concentrated serum-derived EVs to assess accuracy and matrix effects on analyte recovery. Serum samples with low endogenous levels of EVs were chosen as carrier matrices. They were then subsequently spiked with a known amount of serum-derived EVs. All serum samples were

run at the optimal recommended dilution factor of 4X. The results of the spike recovery test are shown in Table 4. Most samples fell within the acceptable range of 80 - 110% recovery. The two mid level spiked samples had recoveries of 112% that is just slightly above the acceptable range. The coefficient of variation for all spiked samples was also below 10%. These results suggest that the assay has high accuracy and precision when measuring the concentration of EVs in human serum, especially when utilizing EVs derived from the same biospecimen (i.e. pooled serum) as calibration material.

Table 3.2 Plasma parallelism and standard deviation for PanTet capture (n = 2 technical replicates)

	CD9 Detector			**CD63 Detector**			**CD81 Detector**		
Dilution Factor	**P1**	**P2**	**P3**	**P4**	**P5**	**P6**	**P7**	**P8**	**P9**
2X	0.351 ± 0.014	0.742 ± 0.121	0.581 ± 0.079	0.116 ± 0.024	0.221 ± 0.066	0.401 ± 0.066	0.113 ± 0.001	0.717 ± 0.013	0.077 ± 0.001
4X	0.234 ± 0.042	0.357 ± 0.047	0.300 ± 0.099	0.071 ± 0.011	0.076 ± 0.024	0.421 ± 0.011	0.099 ± 0.004	0.577 ± 0.007	0.0329 ± 0.010
8X	0.195 ± 0.029	0.198 ± 0.02	0.132 ± 0.032	0.033 ± 0.001	0.031 ± 0.001	0.105 ± 0.038	0.055 ± 0.002	0.152 ± 0.003	0.018 ± 0.003
16X	0.222 ± 0.037	0.168 ± 0.047	0.153 ± 0.022	0.030 ± 0.001	0.037 ± 0.001	0.034 ± 0.012	0.027 ± 0.003	0.039 ± 0.003	0.018 ± 0.001
32X	0.194 ± 0.037	0.170 ± 0.018	0.113 ± 0.011	0.036 ± 0.001	0.033 ± 0.033	0.02 ± 0.001	0.021 ± 0.002	0.019 ± 0.002	0.016 ± 0.002

64X	0.155 ± 0.037	0.099 ± 0.008	0.086 ± 0.001	0.036 ± 0.004	0.032 ± 0.003	0.019 ± 0.005	0.022 ± 0.001	0.015 ± 0.001	0.014 ± 0.002

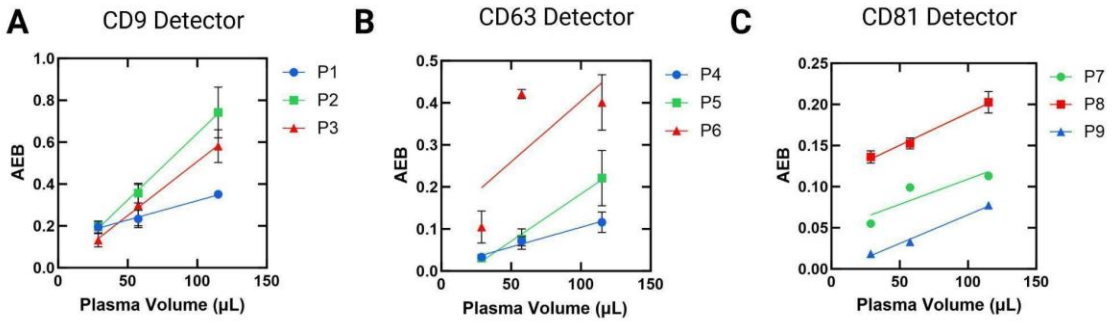

Figure 3.5 (A - C) Linear dilution series of EDTA plasma for PanTet capture and CD9, CD63, and CD81 detection (n = 2 technical replicates).

Table 3.3 Serum parallelism and standard deviation for PanTet capture (n = 2 technical replicates)

	CD9 Detector			**CD63 Detector**			**CD81 Detector**		
Dilution Factor	**S1**	**S2**	**S3**	**S4**	**S5**	**S6**	**S7**	**S8**	**S9**
2X	0.234 ± 0.018	0.343 ± 0.015	0.807 ± 0.151	0.547 ± 0.059	0.309 ± 0.015	0.319 ± 0.019	0.201 ± 0.012	0.1648 ± 0.045	0.170 ± 0.033
4X	0.187 ± 0.014	0.213 ± 0.02	0.398 ± 0.075	0.330 ± 0.097	0.156 ± 0.0462	0.195 ± 0.018	0.089 ± 0.013	0.112 ± 0.028	0.111 ± 0.043
8X	0.155 ± 0.008	0.147 ± 0.016	0.309 ± 0.053	0.157 ± 0.025	0.091 ± 0.016	0.116 ± 0.003	0.025 ± 0.006	0.025 ± 0.006	0.030 ± 0.006
16X	0.101 ± 0.004	0.154 ± 0.015	0.194 ± 0.015	0.108 ± 0.030	0.059 ± 0.001	0.083 ± 0.001	0.041 ± 0.005	0.041 ± 0.005	0.020 ± 0.003

32X	0.078 ± 0.001	0.066 ± 0.002	0.123 ± 0.020	0.078 ± 0.008	0.047 ± 0.004	0.046 ± 0.001	0.032 ± 0.004	0.032 ± 0.004	0.014 ± 0.002
64X	0.063 ± 0.002	0.118 ± 0.012	0.102 ± 0.010	0.047 ± 0.001	0.0309 ± 0.006	0.032 ± 0.001	0.017 ± 0.004	0.017 ± 0.004	0.022 ± 0.001

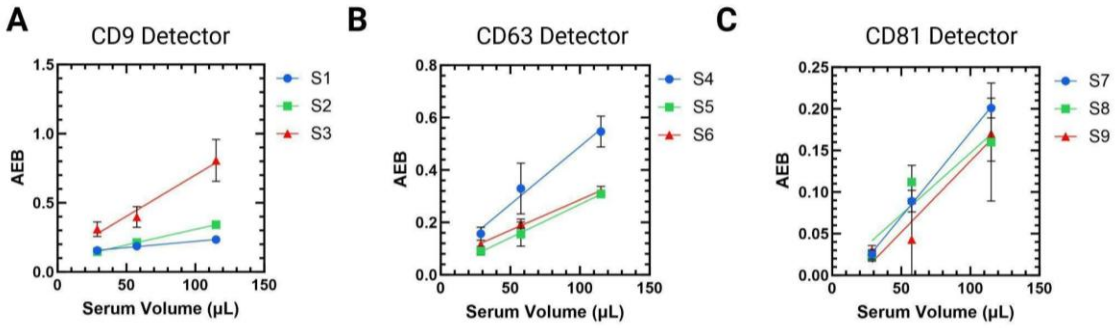

Figure 3.6 (A - C) Linear dilution series of serum for PanTet capture and CD9, CD63, and CD81 detection (n = 2 technical replicates).

Table 3.4 Spike recovery results of concentrated serum EVs spiked into normal male serum samples.

		AEB	Reported Concentration (EVs/mL)	Expected Concentration (EVs/mL)	% Recovery	% CV
Serum 10	No spike	0.098	1.7×10^8	-	-	8.8
	Low Spike	0.152	3.18×10^8	3.00×10^8	105.9	13.9
	Mid Spike	0.594	1.48×10^9	1.32×10^9	112.1	5.3
	High	2.58	7.29×10^9	6.98×10^9	104.4	2.1
Serum 11	No spike	0.055	7.02×10^7	-	-	6.0

	Low Spike	0.25	5.66×10^8	6.00×10^8	94.37	0.4
	Mid Spike	0.67	1.69×10^9	1.50×10^9	112.37	2.4
	High Spike	2.17	6.00×10^9	7.2×10^9	83.8	13.1

3.4.4 Comparing Sensitivity and Robustness to a Commercial Assay

We also opted to compare the sensitivity and reproducibility of our SiMoA assay to a commercially available electrochemiluminescence assay from Mesoscale Discovery (MSD). We evaluated the sensitivity of our most sensitive assay configuration - CD63 capture and CD9 detection - against MSD's R-plex assay (Mesoscale Discovery, Cat #F215L-3 and Cat #F215M-3). We ran the same normal plasma derived EV calibrator material across both platforms side-by-side for 2 separate runs completed one week apart (Figure 3.7). Our SiMoA assay exhibited good inter-experiment reproducibility as the percent difference between the slope of the two calibration curves was only 5.0% and the average coefficient of variation was 11.4%. In comparison, the MSD R-plex assay had very good intra-plate precision. The average coefficient of variation was only 7.9%. However, the calibration slope varied by 31% between the two separate runs, and the limit of detection was significantly lower on the second run compared to the first. There was greater than two orders of magnitude difference between the two calibration curves despite using aliquots of the same EVs. SiMoA was an order of magnitude less sensitive than the R-plex assay, however due to the significant difference in response between the two curves produced using MSD, our SiMoA assay showed superior inter-plate reproducibility.

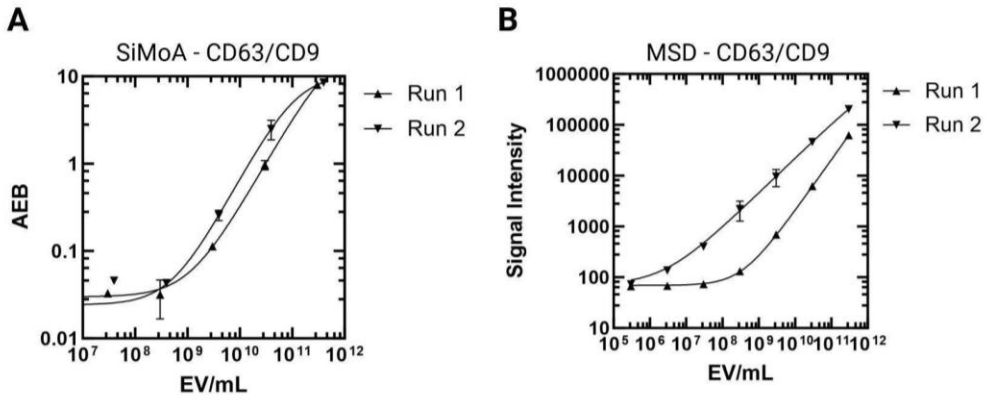

Figure 3.7 Comparison of sensitivity and reproducibility of our SiMoA CD63 capture and CD9 detection assay compared to the commercial R-Plex assay from Meso Scale Discovery. (A) Our SiMoA assay results for normal plasma derived EVs isolated via ultracentrifugation with an LOD of 8.0 x 10^8 EVs/mL for run 1 and 3.57 x 10^8 EVs/mL for the second run. (B) MSD's R-plex assay results for a calibration curve using normal plasma derived EVs. The first run had an LOD of 2.5 x 10^7 EVs/mL and the second run had an LOD of 1.2 x 10^5 EVs/mL.

3.4.5 Comparing Phenotypic Differences of Tetraspanin Expression in Serum

Here we have utilized the SiMoA assay to explore phenotypic differences between normal plasma EVs and breast cancer derived EVs. Due to the natural heterogeneity of EVs, the limit of detection and slope of the calibration curve depends greatly on the type of material used. The slope of the calibration curve produced using tEVs isolated from MCF7 conditioned media is greater than the slope produced by normal EVs. The signal produced by the tEVs is approximately ten times greater for the same concentration (Figure 3.7A). Additionally, we tested a small cohort of eight serum samples collected from patients diagnosed with breast cancer (BC) to compare against normal serum. We utilized three assay configurations to compare the expression rate of CD9 and CD63 between the two groups. The heterogeneous combination of CD63 capture and CD9 detection indicated that

BC samples tended to produce an AEB five times higher than normal serum (Figure 3.7B). It was observed that this difference in signal can be attributed to the presence of ten times more EVs on average present in BC serum. Under further examination, it appears that CD63 is potentially upregulated in breast cancer serum compared to normal individuals (Figure 3.7C). Conversely, the rate of CD9 expression remained relatively constant (Figure 3.7C). These results support previous studies in which EVs derived from tumors have been found to often more highly express CD63 than normal plasma.

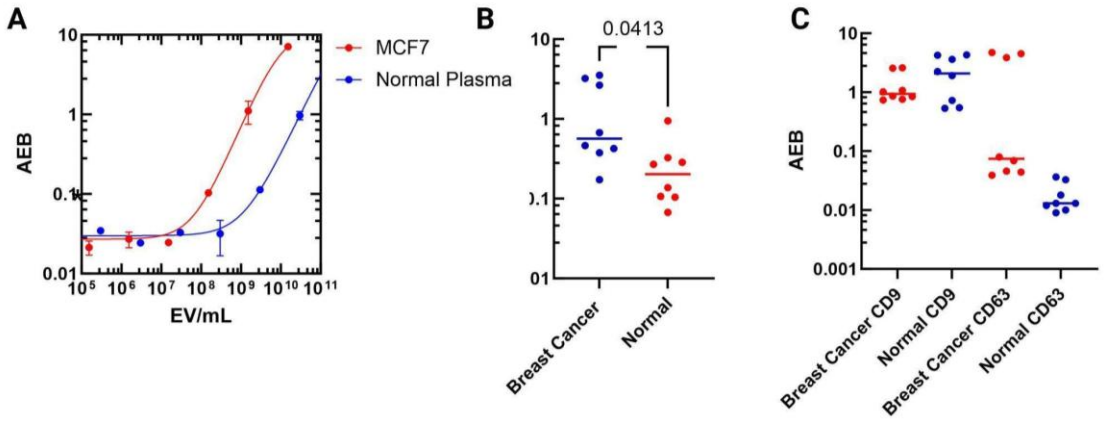

Figure 3.8 (A) SiMoA calibration curves for CD63 capture and CD9 detection using EVs isolated from MCF7 conditioned media (Galen Cat#HBM-MCF7-100/5) and normal human plasma EVs. (B) Comparison of reported AEB values for the CD63 capture and CD9 detection assay run using serum samples taken from normal patients and patients diagnosed with breast cancer. (C) Reported AEB values for total CD9 (CD9 capture and detection) and total CD63 (CD63 capture and detection) in normal and breast cancer serum. (N = 8 normal female serum samples and N = 8 female breast cancer serum samples). For normal serum, 5 out of 8 samples were below the limit of quantification. (CD9 assay p–value = 0.1555 and CD63 assay p-value = 0.0558).

3.4.6 Detection of Small tumor-derived EV Subpopulations

Magnetic beads were also conjugated with anti-CD44 antibodies (Abcam Cat#AB6124) in order to target EVs derived from cancer stem cells. CD44 is a cell surface glycoprotein known to bind to hyaluronan and it is often overexpressed by cancer cells in order to better navigate their environment. In particular, CD44 is a marker of cancer metastasis

due to its ability to help cells stick and unstick themselves from the surrounding tumor. It is often correlated with tumor aggressiveness and chemoresistance. The proposed dual-target immunoassay - CD44 capture paired with CD63 detection - has great potential to detect aggressive, chemoresistant tumors early on. It utilizes the upregulation of both surface markers by cancer cells to increase the clinical utility compared to using just normal tetraspanins for quantification. The results shown in Figure 3.8 indicate its use to detect EVs derived from breast, colorectal, and brain cancer.

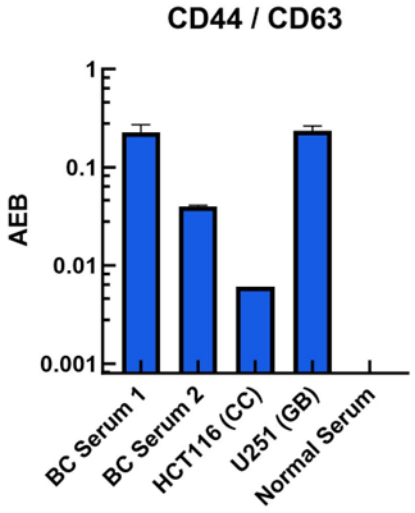

Figure 3.9 SiMoA AEB results for an assay designed to target EVs derived from stem cell like cancer cells using CD44 capture and CD63 detection. Serum samples were run using a 4X dilution and all EVs derived from cell conditioned media were run at a concentration of 10^{10} particles/mL. The AEB of the blank was 0.005 ± 0.001.

Normal serum levels of $CD44^+$ EVs are typically very low and were found to be below the limit of detection. In comparison, a 4-fold dilution of different two breast cancer serum samples had detectable levels of $CD44^+$ EVs. The signal-to-noise ratio of one sample was 36 times greater than that of the blank and the second sample was 8 times greater.

Additionally, EVs derived from cell conditioned media of HCT116 (colorectal cancer) and U251 (glioblastoma) cells also showed significant expression of $CD44^+$ EVs. These results are a proof-of-concept for further application of this assay to measure small subpopulations of potentially pathogenic EVs circulating in peripheral fluids.

3.5 Conclusion

The development of a digital Single Molecule Array (SiMoA) assay for the quantification of EVs represents a significant advancement in liquid biopsy technology. By leveraging the sensitivity of a digital ELISA platform, we have demonstrated a robust method for detecting intact EVs in complex matrices such as plasma and serum. Our findings highlight several critical technical considerations when designing an assay - ranging from the mathematical modeling of analyte binding to the biological implications of tetraspanin expression. Overcoming such difficulties are essential for the clinical translation of EV diagnostics.

A central challenge in adapting SiMoA for EVs is the physical nature of the analyte. Unlike small proteins, EVs are relatively large and polyvalent, possessing multiple binding sites for a single bead. This characteristic theoretically threatens the Poisson distribution assumption (Equation 1) that is fundamental for digital quantification. To mitigate this, we evaluated a continuous weighted function for AEB determination (Equation 5). While the piecewise function (Equation 4) proved sufficient for our optimized assay, the continuous model offers a potential solution for inter-experiment variability and lot-to-lot

inconsistencies, which are common hurdles in clinical assay validation. The ability of the piecewise function to maintain a dynamic range over four orders of magnitude suggests that the large size of EVs and polyvalency does not inherently break the digital logic of SiMoA. Our results demonstrate that under optimized conditions, the system remains Poisson-compliant at low concentrations.

We described how the three tetraspanins - CD9, CD63, and CD81 - could be mixed and matched as needed to develop custom assays. Our evaluation of 12 potential assay configurations provided valuable insight on the expression rate of each tetraspanin on the EV surface. Specifically, using CD9 as a detector consistently yielded an order of magnitude higher sensitivity compared to CD63 or CD81. This is likely reflective of the higher surface density of CD9 on the isolated serum EVs. Conversely, CD63 performed poorly as a general detector, supporting its reputation as a more variable or less abundant marker in certain EV subpopulations. The specific enrichment of CD63 on tumor-associated EVs aligns with the known biological role of this tetraspanin in malignancy. CD63 is deeply involved in the regulation of intracellular trafficking, integrin signaling, and the modulation of the tumor microenvironment. Its upregulation in breast cancer EVs suggests a potential role in driving metastasis or stromal remodeling, making it not just a structural marker, but a biologically relevant target for disease monitoring.[129-131] We further explored this idea by utilizing the assay as a proof-of-concept for disease monitoring. We compared the rate of CD9 and CD63 expression in breast cancer serum to normal serum. We observed that EVs derived from MCF7 cells and BC patient serum produced significantly higher signals than those from healthy controls. Notably, CD9 expression

remained relatively consistent between groups, while CD63 expression was significantly increased in breast cancer serum. This shift in the focus from simple EV quantification to phenotypic profiling explores the potential to distinguish between total EV counts and specific tumor-associated subpopulations. Such kinds of analytical methods could provide a more nuanced tool for oncology, opening the door for earlier detection or better disease monitoring.

The specificity of the assay for intact vesicles was rigorously confirmed through depletion and degradation studies. The loss of signal following membrane lysis and protease treatment confirms that the assay specifically measures intact vesicles via their surface epitopes rather than free-floating proteins or debris.

Performance is a critical requirement for any clinical diagnostic in complex biospecimens. Our assay demonstrated parallelism and linearity in both EDTA plasma and serum across an 8-fold dilution range. Our SiMoA platform showed superior inter-plate reproducibility when compared to the commercial MSD R-plex assay. While the MSD platform showed high intra-plate precision, its significant variation in calibration slope (31%) and LOD (two orders of magnitude) between runs suggests that SiMoA may be a more reliable platform for longitudinal clinical studies where samples are processed at different times.

Despite these promising results, we acknowledge certain limitations in the current study. First, the breast cancer cohort utilized for phenotypic profiling was small (N=8 per group) and strictly intended as a proof-of-concept; large-scale, longitudinal clinical cohorts are required to robustly validate the diagnostic performance of the CD63/CD9 signature.

Secondly, while ultracentrifugation is the gold standard for generating our calibrator material, it is known to co-isolate lipoproteins of similar densities, such as HDLs. Because NTA cannot perfectly distinguish between EVs and lipoproteins, there is an inherent limitation in the absolute accuracy of the calibrator concentration, though the relative quantification and extreme linearity demonstrated across serial dilutions remain highly robust.

Further work should be done to continue to expand the utility of the assay for quantification in other complex biofluids such as cerebral spinal fluid (CSF) and saliva. This work showcases the potential of SiMoA technology to perform high-throughput phenotypic EV screening. Additionally, multiplex assays should be developed to further elucidate the potential of identifying EV subpopulations. The development of single and multiplex assays utilizing tumor-specific markers such as HER2 could further enhance the diagnostic potential for breast cancer.

In conclusion, we have established a Single Molecule Array framework capable of sensitive and robust quantification of intact EVs directly from human plasma and serum. While emerging single-particle techniques like SP-IRIS and nanoFCM offer excellent multiparameter resolution, they often require highly specialized calibration or face throughput limitations. With a limit of detection reaching 1.61×10^7 EVs/mL and the ability to process samples in a standard multi-well format, this SiMoA approach bridges the gap between single-vesicle sensitivity and the high-throughput, standardized workflows required for centralized clinical laboratories. By optimizing the transition

between digital and analog detection, this platform provides a scalable solution for the emerging field of EV-based molecular diagnostics.

3.6 Supporting Information

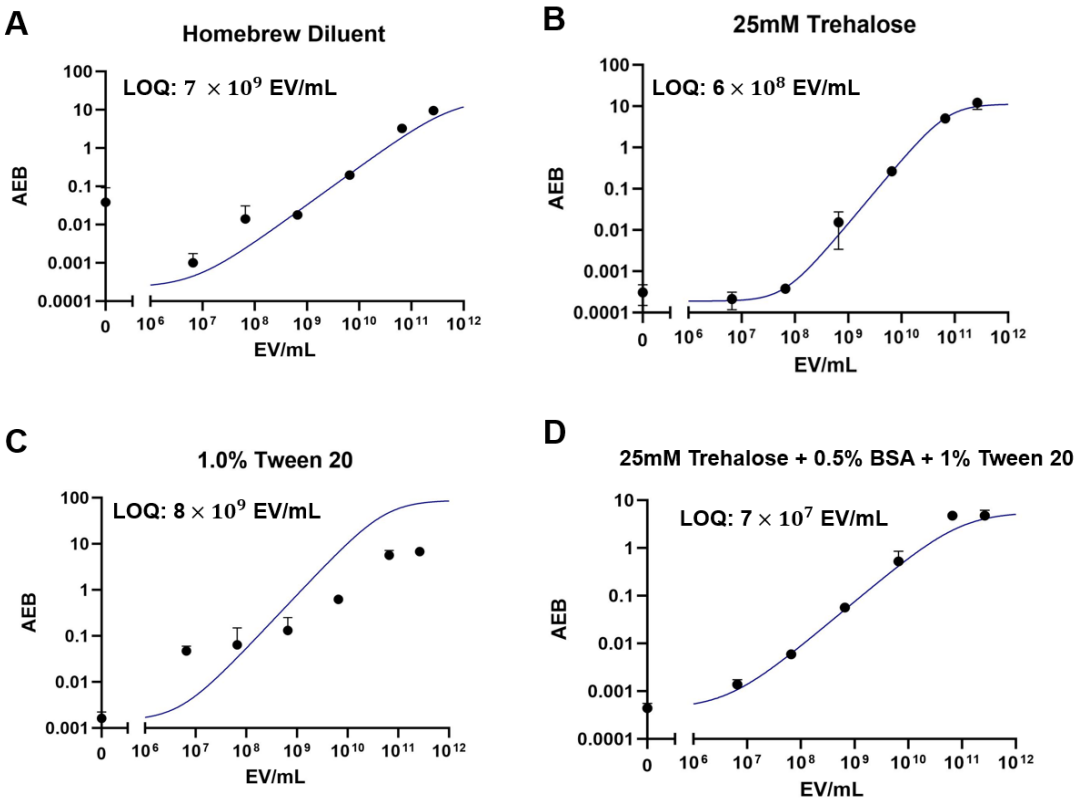

Figure S3.1 The sample diluent used to dilute and resuspend EV pellets was optimized to achieve the lowest LOD and greatest dynamic range using CD9 capture and detection. Different zwitterionic buffers and additives were tested to stabilize EVs and lower nonspecific binding. (A) We tested the effectiveness of Quanterix's standard homebrew sample diluent as a control. (B) Trehalose was mixed with 250 mM HEPES buffer solution. (C) 1% Tween 20 (v/v) was added to a 250 mM HEPES solution. (D) 25mM Trehalose, 1.0% Tween 20 (v/v), and 0.5% (w/v) bovine serum albumin (BSA) were all mixed with a 250 mM HEPES buffer. The addition of trehalose and BSA decreased nonspecific binding of vesicles to the well-plate and increased the signal-to-noise ratio. The limit of detection decreased 2 orders of magnitude compared to the control Homebrew diluent.

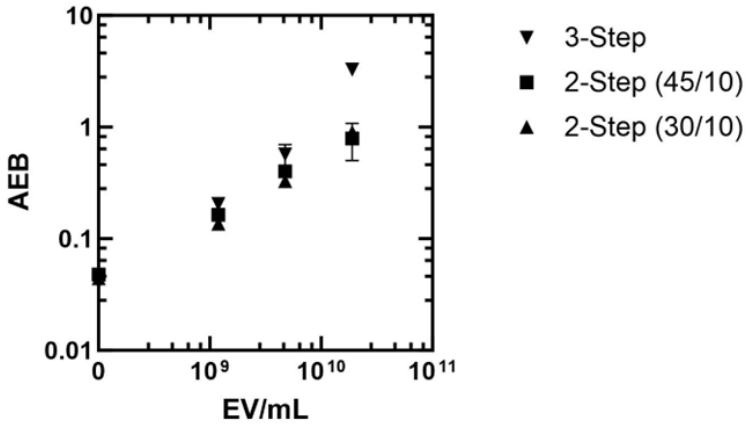

Figure S3.2 Bead incubation times were optimized using CD9 capture and CD9 detection to achieve the lowest limit of detection while maintaining assay robustness. A 3-step assay (35 minute / 20 minute / 10 minute) was chosen as the optimal assay format due to low coefficients of variation and increased signal-to-noise ratio. 2-step assay formats yielded similar results but were more prone to nonspecific vesicle binding. The minimum bead incubation time required was determined to be 30 minutes and the maximum was 45 minutes. Below 30 minutes, the signal was too low for quantification. Above 45 minutes, some samples experience nonspecific binding of vesicles leading to overestimation.

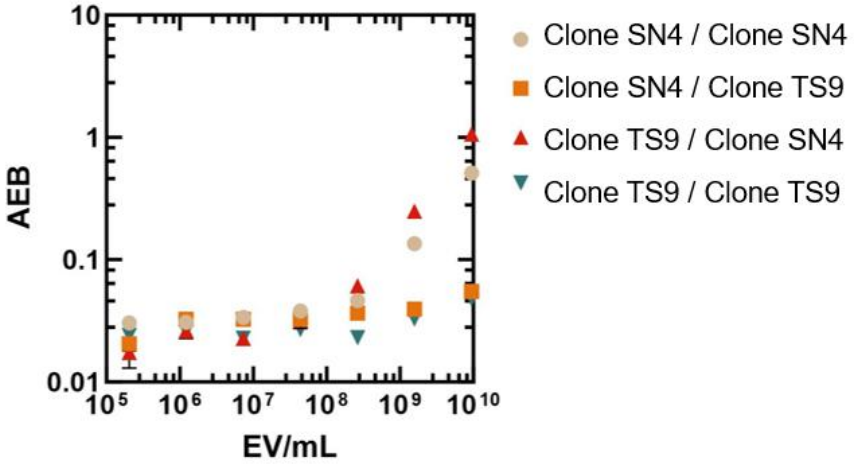

Figure S3.3 Sensitivity analysis to determine the optimal CD9 capture and detector pairing.

In order to assess the effectiveness of antibody conjugation, the coating efficiency was calculated for each capture bead produced. The coating efficiency is defined as the final antibody mass left in solution divided by the initial amount used. This was measured using UV-vis spectrophotometry wavelength 280nm. The conjugation buffer was used as the blank reference. It is important to note that a high coating efficiency does not necessarily equate to functional beads. During the conjugation process, the antibody could potentially degrade, aggregate, or bind to the surface in a non-functional orientation. The conjugation reaction was run at 4℃ to control the rate of reaction.

Table S3.1 Capture bead antibody coating efficiency

Antibody	Starting Amount (μg)	Ending Amount (μg)	Coating Efficiency (%)
anti-CD9	75	19.4	73.5
anti-CD63	65.4	15.3	76.3
anti-CD81	75	21.3	66.2

Table S3.2 is provided to outline the calculated limits of detection (LODs) for each assay configuration tested using the serum-derived EVs. The LOD was calculated as the sum of the blank's AEB plus 3.3 times the standard deviation of blank. Each curve was fitted using 4 parameter logistic regression using GraphPad Prism 10.0.2.

Table S3.2 Limit of detection for each SiMoA EV assay configuration.

Capture	**Detector**	**Limit of Detection (EVs/mL)**
CD9	CD9	2.77×10^7

CD9	CD63	5.09×10^9
CD9	CD81	1.40×10^8
CD63	CD9	1.61×10^7
CD63	CD63	9.82×10^8
CD63	CD81	4.63×10^8
CD81	CD9	2.65×10^8
CD81	CD63	1.73×10^{10}
CD81	CD81	3.5×10^7
PanTet	CD9	5.04×10^7
PanTet	CD63	2.99×10^9
PanTet	CD81	5.18×10^8

The capture beads were also utilized to perform immunoaffinity isolation from 1 mL of normal plasma in order to characterize the size distribution of EVs targeted by the beads. The EV yield and size distributions are shown below:

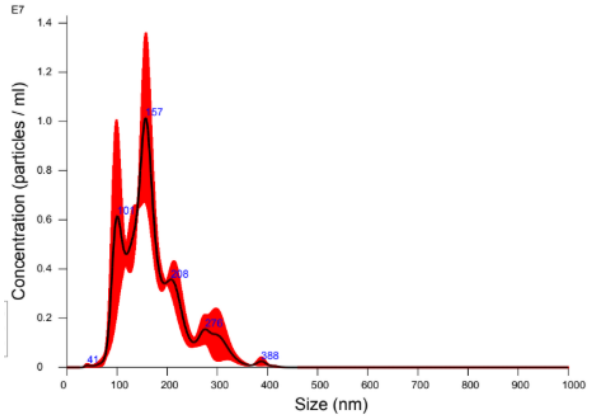

Figure S3.4 Nanoparticle tracking analysis (Malvern Nanosight NS3000) results for CD9 immunoaffinity isolation. Samples are diluted 1:1000 in 1X PBS. The average diameter is 172.6 ± 11.2 nm and the mode is 149.2 ± 7.7 nm.

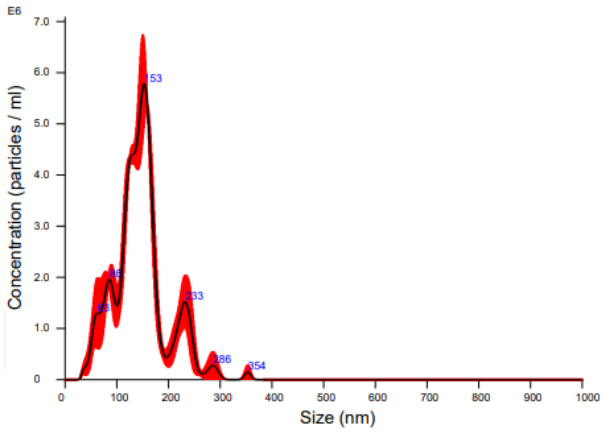

Figure S3.5 Nanoparticle tracking analysis (Malvern Nanosight NS3000) results for CD81 immunoaffinity isolation. Samples are diluted 1:100 in 1X PBS. The average diameter is 145.8 ± 3.1 nm and the mode is 156.4 ± 3.9 nm.

CD63 immunoaffinity from 1 mL of normal plasma did not yield enough EVs to be accurately detected using NTA. For CD9 immunoaffinity, the presence of each tetraspanin was also confirmed using a traditional western blot and compared against EVs isolated using ultracentrifugation and precipitation.

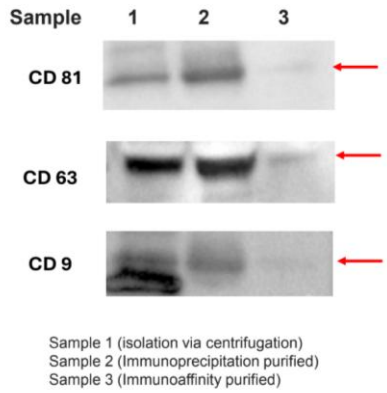

Figure S3.6 Image of the western blot used to positively detect the presence of all three tetraspanins (CD9, CD63, and CD81) in EVs isolated across 3 different methods from 1

mL of normal plasma. The immunoaffinity EVs were isolated overnight using CD9 capture beads. Precipitation was performed using commercially available reagents (ExoQuick Cat#: EXOQ5TM-1).

For the comparison of normal and breast cancer patient derived serum, additional EVs were isolated from pooled normal plasma for the generation of the calibration curve shown in Figure 3.7. The same ultracentrifugation protocol was followed as described in section 3.3.4 to produce a pellet that was subsequently characterized using the Malvern ZetaView instrument at the Extracellular Vesicle Core Facility at Brown University Health. The results and instrument parameters are shown below (Figure S3.1).

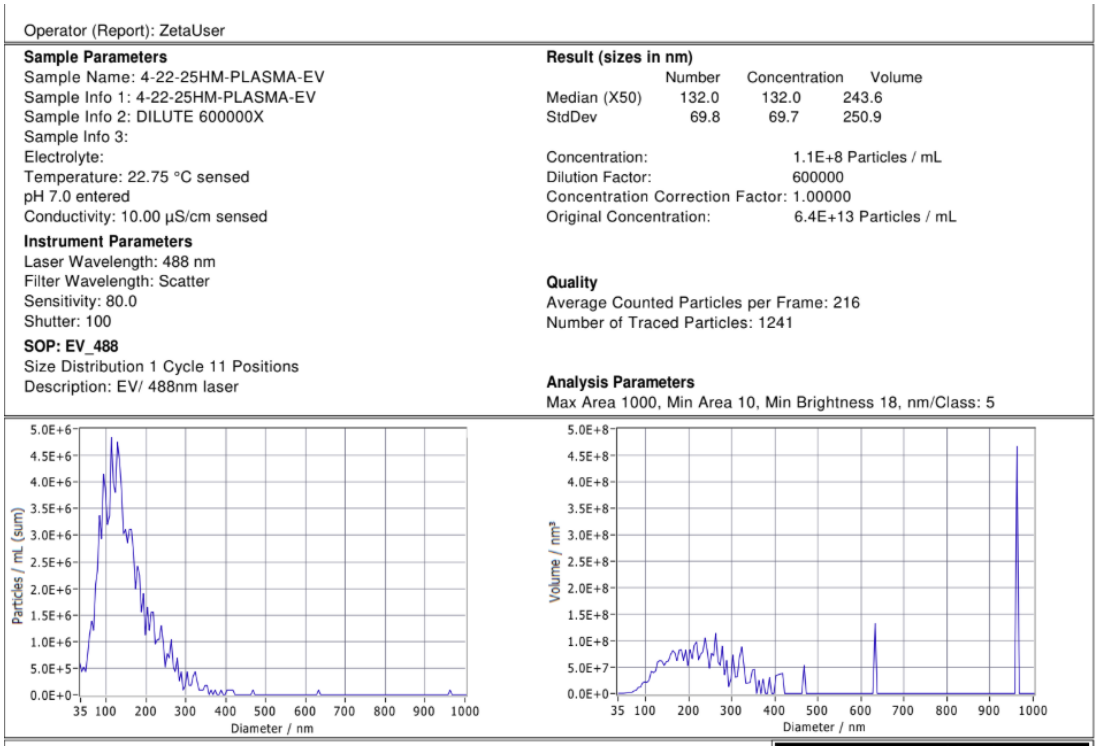

Figure S3.7 Nanoparticle tracking analysis results for plasma-derived EVs isolated via ultracentrifugation using Malvern ZetaView. These EVs were used as standards for the SiMoA EV quantification assay to calculate the concentration of vesicles in normal and breast cancer serum. The average reported diameter is 132.0 nm +/- 69.8 nm.

The AEB and intensity signal values are reported in the following tables (Tables S3. - S3.) that are used to compare the sensitivity of our configurable assay to the commercially available plate-based electrochemiluminescence assay sold by MSD. Tables of the raw AEB values for the breast cancer serum and normal serum comparison are also provided for transparency.

Table S3.3 Reported AEB and signal intensity values for the calibration curves produced using plasma derived-EVs for both the SiMoA and MSD R-Plex Assay. For both platforms CD9 was used for capture and CD63 was used for detection.

Plasma EV Calibrators	Particles /mL	SiMoA (AEB)	s.d.	MSD (intensity)	s.d.
Cal A	3.00E+11	0.109	0.024	35431.5	639.931
Cal B	3.00E+10	0.006	0.001	7966	367.695
Cal C	3.00E+09	0.002	0.001	1562	155.563
Cal D	3.00E+08	0.001	0.000	399	19.798
Cal E	3.00E+07	0.000	0.000	128	1.414
Cal F	3003000	0.001	0.000	78.5	3.535
Cal G	300300	0.001	0.001	63	2.828
Cal H	0	0.001	0.000	71.5	10.606

Table S3.4 Reported AEB and signal intensity values for the calibration curves produced using plasma derived-EVs for both the SiMoA and MSD R-Plex Assay. For both platforms CD63 was used for capture and CD9 was used for detection.

Plasma EV Calibrators	Particles / mL	Simoa	s.d.	MSD	s.d.
Cal A	3.00E+11	8.002	0.069	204123	579.827
Cal B	3.00E+10	0.969	0.116	46333.5	2056.973
Cal C	3.00E+09	0.113	0.010	9658	3573.717
Cal D	3.00E+08	0.032	0.015	2209	929.138
Cal E	3.00E+07	0.033	0.003	403	19.798
Cal F	3003000	0.024	0.000	137	8.485
Cal G	300300	0.034	0.001	73.5	4.949

Cal H	0	0.033	0.007	68	0

Table S3.5 Reported AEB and signal intensity values for the calibration curves produced using MCF7 derived-EVs for both the SiMoA and MSD R-Plex Assay. For both platforms CD63 was used for capture and CD9 was used for detection.

MCF7 EV Calibrators	Particles / mL	Simoa	s.d.	MSD	s.d.
Cal A	1.53E+10	7.097	0.283	305763.5	3901.108112
Cal B	1.53E+09	1.107	0.355	31646.5	140.7142495
Cal C	1.53E+08	0.103	0.004	3351	48.08326112
Cal D	1.53E+07	0.025	0.001	388	18.38477631
Cal E	1533333.333	0.027	0.006	100	4.242640687
Cal F	153333.3333	0.021	0.004	69.5	0.7071067812
Cal G	15333.33333	0.036	0.008	66	0
Cal H	0	0.031	0.000	66	4.242640687

Table S3.6 Reported AEB values and standard deviations for 4X dilutions of breast cancer serum using CD63 capture and CD9 detection.

	AEB	**s.d.**
BC 1	0.425	0.046
BC 2	3.539	0.881
BC 3	0.173	0.028
BC 4	3.221	0.669
BC 5	2.651	0.063
BC 6	0.674	0.114
BC 7	0.378	0.050
BC 8	0.463	0.003

Table S3.7 Reported AEB values and standard deviations for 4X dilutions of normal female serum using CD63 capture and CD9 detection.

	AEB	**s.d.**

HC 1	0.326	0.000
HC 2	0.105	0.016
HC 3	0.137	0.008
HC 4	0.945	0.124
HC 5	0.286	0.002
HC 6	0.067	0.012
HC 7	0.270	0.017
HC 8	0.107	-

Table S3.8 Reported AEB values and standard deviations for 4X dilutions of breast cancer serum using CD63 capture and CD63 detection.

	AEB	**s.d.**
BC 1	0.039	0.004
BC 2	4.724	0.532
BC 3	0.044	0.001
BC 4	4.531	0.352
BC 5	3.880	0.181
BC 6	0.080	0.003
BC 7	0.046	0.004
BC 8	0.069	0.001

Table S3.9 Reported AEB values and standard deviations for 4X dilutions of normal female serum using CD63 capture and CD63 detection.

	AEB	**s.d.**
HC 1	0.036	0.000
HC 2	0.009	0.006
HC 3	0.013	0.003
HC 4	0.033	0.000
HC 5	0.018	0.006
HC 6	0.012	0.000

HC 7	0.013	0.001
HC 8	0.010	0.003

Table S3.10 Reported AEB values and standard deviations for 4X dilutions of breast cancer serum using CD9 capture and CD9 detection.

	AEB	**s.d.**
BC 1	1.078	0.120
BC 2	1.018	0.255
BC 3	0.862	0.269
BC 4	0.760	0.148
BC 5	0.736	0.119
BC 6	2.565	0.080
BC 7	0.845	0.095
BC 8	2.599	0.143

Table S3.11 Reported AEB values and standard deviations for 4X dilutions of normal female serum using CD9 capture and CD9 detection.

	AEB	**s.d.**
HC 1	0.546	0.003
HC 2	1.906	0.620
HC 3	4.256	0.724
HC 4	3.604	0.926
HC 5	4.304	0.368
HC 6	0.535	0.127
HC 7	2.244	0.400
HC 8	0.728	0.223

Table S3.12 The expression of CD81 on the surface of serum EVs was measured for the same breast cancer serum samples. CD63 was used as the capture bead and CD81 was used as the detector.

	AEB	s.d.
BC 1	0.047	0.009
BC 2	1.614	0.132
BC 3	0.058	0.003
BC 4	1.836	0.247
BC 5	1.432	0.635
BC 6	0.054	0.001
BC 7	0.057	0.022
BC 8	0.031	0.000

Table S3.13 The expression of CD81 on the surface of serum EVs was measured for the same normal female serum samples. CD63 was used as the capture bead and CD81 was used as the detector.

	AEB	s.d.
HC 1	0.155	0.023
HC 2	0.036	0.003
HC 3	0.032	0.003
HC 4	0.032	0.001
HC 5	0.047	0.002
HC 6	0.053	0.038
HC 7	0.052	0.002
HC 8	0.109	0.050

3.7 Acknowledgements

3.7.1 Funding Statement

This work was completed with funding provided in part by Quanterix Corporation, Brown University Graduate School, and the Zimmerman Innovation Award for Brain Science from the Carney Institute for Brain Science.

3.7.2 Author Contributions

J.P., A.T., and K.M., contributed to the conceptualization, supervision, and administration of the project. J.P, C.Y., E.J., J.M., and A.F. contributed to investigation and formal analysis. J.P. and C.Y. designed methodology and contributed to the validation, curation, and visualization of the data. J.P. and A.T. acquired the funding. J.P. and A.T.. wrote the first draft. J.P., A.T., and K.M. reviewed and edited the manuscript.

The authors would also like to gratefully acknowledge Dr. Sicheng Wen and Mandy Pereira, M.S. from the COBRE Extracellular Core Facility at Brown University Health for their guidance and help with EV isolation and NTA analysis. They also thank Dr. Kristine Pelton from Brown University's Fluid Biomarker Core Facility for completing the Mesoscale Discovery experiments. They also give special thanks to Sarah Planchak, M.S. for her work culturing the glioblastoma spheroids and supernatant collection. Another special thanks is given to Dr. Sean Lawler from Brown University Department of Biology and Medicine for providing the U251 cell conditioned media. Mingwei Zhao from Quanterix Accelerator services also helped with troubleshooting technical difficulties.

3.7.3 Conflict of Interest Statement

The authors declare that they have no competing interests. All contributions from authors associated with Quanterix are strictly scientific. The work does not aim to promote or endorse any commercial product.

CHAPTER 4:

Ultrasensitive Single Molecular Array Quantification Assays for Brain-Derived Extracellular Vesicles

---

Chapter 4 has been submitted as an original research article and is currently under review.

Jennifer M. Pollock, Anji Friedbauer, Connor H. Yew, Everett Gutterman-Johns, Kishore Malyvantham and Anubhav Tripathi

1. Biomedical Engineering, School of Engineering and Medical Sciences, Brown University, Providence, RI, USA

2. Quanterix Inc, Billerica, MA, USA

4.1 Abstract

Neurological disorders collectively affect over 3 billion individuals worldwide, yet early-stage diagnosis remains elusive due to a lack of sensitive, minimally invasive biomarkers that can capture dynamic CNS pathophysiology in peripheral blood. Extracellular vesicles (EVs) have emerged as promising liquid biopsy biomarkers for neurological diseases due to their ability to carry CNS-specific cargo across the blood-brain barrier. However, clinical translation is hindered by a lack of standardized, high-throughput quantification methods that can bypass tedious isolation steps and reliably distinguish low-abundance brain-derived EVs (bdEVs) from the dense peripheral background. We developed an isolation-free, digital immunoassay for the direct quantification of bdEVs using Single Molecule Array (SiMoA) technology. To address the analytical challenges posed by EV polyvalency and size, we implemented a continuous piecewise mathematical model for Average Enzymes per Bead (AEB) determination based on Poisson statistics. To our knowledge, this represents the first application of a piecewise AEB correction framework to EV-based SiMoA assays, directly addressing the analytical artifacts introduced by EV polyvalency and stochastic multimarker engagement on single beads. We systematically evaluated a panel of neuronal markers—L1CAM, NCAM, and ATP1A3—alongside canonical tetraspanins (CD9, CD63, CD81) across multiple capture/detector configurations. Assay performance, including dilutional linearity, matrix effects, and limit of detection (LOD), was validated using pooled human serum-derived EVs as a matrix-matched biological reference. The SiMoA framework maintained a dynamic range over four orders of magnitude with exceptional robustness (CV < 10%). NCAM-based capture

yielded the highest sensitivity (LOD = 1.03 x 10^7 particles/mL), while ATP1A3 demonstrated the greatest clinical utility, successfully quantifying bdEVs in > 92% of normal plasma samples. This study establishes a standardized, high-throughput platform for bdEV profiling using SiMoA that eliminates the variability of traditional isolation methods. Our findings suggest that ATP1A3 and NCAM serve as alternatives to L1CAM for stable bdEV quantification. This digital ELISA framework provides a scalable tool for early disease detection and longitudinal monitoring in neuro-oncology and neurodegeneration research.

4.2 Introduction

The past few years have seen a shift in how the scientific community understands extracellular vesicles (EVs). Originally dismissed as cellular waste, EVs are now understood as important mediators of intercellular communication, influencing both ordinary physiology and disease progression.[132] The Minimal Information Studies for Extracellular Vesicles (MISEV) 2023 defines EVs as nano and microparticles delimited by a lipid bilayer that carry bioactive cargo.[39,133] They are an extremely heterogeneous population, varying in size, origin, and surface composition, ranging from 50 nm up to 10 μm. EVs are secreted by most cell types and can be recovered from a wide variety of biofluids including blood, saliva, cerebrospinal fluid, and urine.[133]

EVs have attracted particular interest in the context of neurological disease. In Alzheimer's disease, EVs have been shown to package and propagate neurotoxic species including

amyloid-β and tau, potentially accelerating disease progression.[134] Their ability to cross the blood-brain barrier and into circulating blood makes them accessible, minimally invasive windows into central nervous system (CNS) biology, and attractive diagnostic markers for dementia and other CNS diseases.[135] Alzheimer's disease alone affects an estimated 55 million people globally, and its diagnosis typically occurs years after irreversible neuronal loss has begun.[136] Given that cerebrospinal fluid collection is invasive and blood-based protein biomarkers (e.g., plasma p-tau181) remain confounded by peripheral noise, a high-throughput, EV-based liquid biopsy platform capable of enriching CNS-specific signal from peripheral blood represents a critical unmet clinical need.[137]

Despite their potential, clinical translation of EV-based diagnostics is constrained by existing quantification methods. Conventional bulk ELISAs for EV surface markers typically report detection limits on the order of 10^9-10^{10} particles/mL, one to two orders of magnitude above the physiologically relevant range for bdEVs in plasma. NTA is a good tool to measure the total particle count, but cannot perform the surface-marker-specific discrimination required to isolate the rare bdEV subpopulation (estimated at 1-10% of total plasma EVs) from the dominant non-neural background. Additionally, more high-resolution tools like NanoFCM that can identify rare subpopulations, cannot do so in "dirty" samples and require extensive sample preparation that makes clinical translation not feasible.[138]

Furthermore, there is a lack of standardization in EV isolation. Ultracentrifugation, size exclusion chromatography, and precipitation-based methods each favor yielding

compositionally distinct EV populations, which makes cross-study comparisons unreliable.[138] There is a growing consensus that the field must move towards the development of isolation-free, direct profiling of EVs in biofluids to yield reproducible, clinically actionable results.

Single Molecule Array (SiMoA) technology achieves single-molecule sensitivity by confining enzyme-labelled complexes in femtoliter-volume microwells, enabling digital counting of individual binding events.[122] While SiMoA has been validated for soluble protein biomarkers (e.g., neurofilament light chain, GFAP), its adaptation for nanoparticle analytes such as EVs presents unique challenges related to analyte polyvalency, size, heterogeneity, and the need for co-localization of capture and detector signals to confirm intact vesicle detection. These are challenges that remain unaddressed in the current literature.

For brain-derived EVs (bdEVs) specifically, detection is further complicated by their low abundance relative to the total EV pool population in peripheral blood. Quantifying them reliably depends on the detection of surface markers that can distinguish them from the broader EV background. Markers such as L1CAM, NCAM, and ATP1A3 have been proposed for this purpose, but their comparative performance and quantification in ultrasensitive immunoassays have not been well characterized for immunoassay development.[135] We hypothesize that ATP1A3, by virtue of its integral membrane topology and near-exclusive CNS expression, will outperform L1CAM and NCAM as a capture target in terms of clinical detection rate, and that a digital SiMoA co-localization

framework can be adapted for EV polyvalency to achieve single-vesicle sensitivity directly in unfractionated plasma and serum.

In this study, we present a high-throughput immunoassay utilizing Single Molecule Array (SiMoA) technology (Figure 1) for the direct detection and quantification of EVs in biofluids, without the need for extensive sample concentration or pretreatment. It is to the best of our knowledge, the first to directly compare the performance of multiple neuronal markers using SiMoA technology for intact bdEV detection. It expands upon previous work done utilizing high-resolution - but low throughput - methods to quantify the relative distribution of proteins on the surface of bdEVs.[124] Our assay relies on the colocalization of EV surface markers on antibody-conjugated microbeads to confirm the detection of intact vesicles. We evaluate a selection of neuronal and pan-EV surface markers, including L1CAM, NCAM, ATP1A3 and canonical tetraspanins CD9, CD63, and CD81 across multiple capture and detector configurations and biospecimen types to identify optimal assay formats for bdEV detection and quantification. By comparing these markers within a standard SiMoA framework, this work aims to provide a reproducible and sensitive platform for bdEV quantification and detection that can support future biomarker discovery efforts in the context of neurological disease.

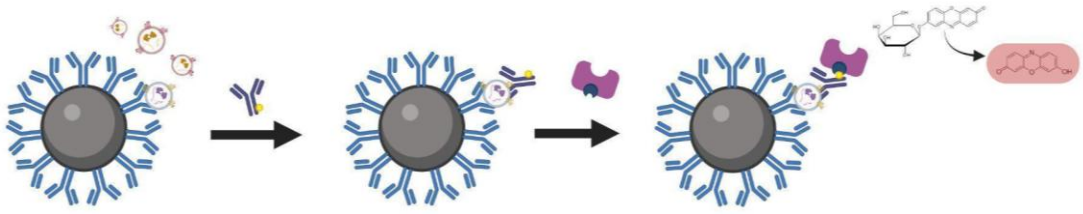

Figure 4.1 Schematic showcasing a simplified visual representation of the Single Molecular Array (SiMoA) for the detection of intact, membrane-enclosed EVs. (Created with Biorender.com)

4.3 Materials and Methods

4.3.1 Bead Conjugation

Simoa 488nm Homebrew Beads (Catalog #104006) were conjugated with monoclonal antibodies using 1-ethyl-3-(3-dimethylaminopropyl) carbodiimide (EDC) chemistry. Prior to antibody addition, the carboxylic acid functional groups on the bead surface were activated with EDCS/NHS. Immediately after activation, the diluted antibody solution was added to the beads and incubated for 2 hours with over-end mixing. UV-vis (NanoDrop ND-1000 Spectrophotometer) was used to measure the antibody content in solution pre and post-isolation to evaluate the coating efficiency. The bead surface was further passivated using Bead Blocking Buffer (Quanterix Cat#101356) for 1 hour at room temperature.

Table 4.1 Capture and detection antibodies used for the assay.

Antigen	**Vendor**	**Usage**	**Cat. No.**	**Host/isotype**	**Species Specificity**
L1CAM	Abcam	Capture	ab80832	Murine IgG1 kappa	human
NCAM	Abcam	Capture	ab8233	Murine IgG2a	human
ATP1A3	Abcam	Capture	ab2826	Murine IgG1	Human, mouse, rat
Biotin-NCAM	Ancell	Detector	208-030		human
Biotin-CD9	Ancell	Detector	156-030	Murine IgG1 kappa	human

Biotin-CD63	Ancell	Detector	215-030	Murine IgG1	human
Biotin-CD81	Ancell	Detector	302-030	Murine IgG1	human
Mouse IgG	Abcam	Capture	ab37355	Murine Polyclonal IgG	-

4.3.2 SiMoA bdEV Assay

Analysis was performed on the Quanterix Simoa HD-X system using a custom 3-step assay definition. The first bead incubation step was 35 minutes, followed by a 20 minute detector incubation, and a 10 minute incubation with streptavidin beta-galactosidase (SBG) reagent. All the samples were diluted on the bench using EV sample diluent and allowed to come to room temperature for one hour prior to analysis. All bead stocks were resuspended with over-end mixing for 1 hour prior to being loaded onto the reagent bay.

4.3.3 Immunoaffinity Isolation

Capture beads were added to 1 mL aliquots of EDTA plasma at the volumes indicated. These samples were then incubated overnight with over-end mixing for 18 hours. The capture beads were pelleted using a magnetic stand and washed three times with 1mL of 1X PBS + 0.01% Tween-20. 50 uL 0.2M Glycine HCl (pH = 2.5) was used to elute the EVs from the capture beads for 40 minutes with mixing at 1000rpm. After the incubation period, the eluent was transferred to a clean tube and neutralized with 5 uL of Tris HCl (pH = 9.0).

4.3.4 Ultracentrifugation

Pooled serum or plasma was obtained from commercial sources (BioIVT Cat#HUMANSRM-9982-T and Cat#HUMANPLK2-9914-R) as deidentified specimens and exempt from institutional IRB approval. The samples were all held at -80ºC prior to EV isolation. To begin isolation, samples were thawed in a 37ºC water bath prior to centrifugation at 5000xg for 10 minutes at 4ºC to clear debris. The supernatant was collected and transferred to sterile 2 mL protein lo-bind tubes and diluted with 1X PBS. It was then spun again for 30 minutes at 10,000xg, with no brake during deceleration. The supernatant was removed and the pellet was resuspended in 1X PBS. The sample was then centrifuged one more time at 100,000xg for 2 hours. Following centrifugation, the pellet was resuspended in 250 µL of cold EV sample diluent and stored at -20ºC until use. The size and concentration of the EVs was determined using a Nanosight 5000 and results are reported along with instrument parameters in Supplementary Figure S4.2.

4.3.5 Statistical Analysis

Calibration curves were fit using unweighted 4-parameter logistic regression. LOD was calculated as the mean blank AEB plus 3.3 standard deviations (Equation S1). LOQ was defined as 3.3 × LOD (Equation S2). Coefficient of variation (CV%) was calculated as (SD / mean) × 100 for each dilution across replicates. Dilutional linearity was assessed by plotting measured AEB versus expected AEB (based on linear extrapolation from the lowest non-blank standard). All calculations were performed using GraphPad Prism 10.0.2.

Data are expressed as mean ± SD unless otherwise stated. No samples were excluded from analysis.

4.4 Results and Discussion

4.4.1 Calculating Average Enzymes Per Bead (AEB)

The concentration of EVs is determined by utilizing Poisson statistics to calculate the average number of enzymes per bead (AEB). Three key assumptions are made - (1) an excess of capture beads is added to the sample, (2) EV binding is an independent event, and (3) the sample is well-mixed. When these three assumptions are true, analyte binding follows a Poisson distribution that allows for AEB to be calculated using the following equations:

$$\mathrm{AEB}_{\mathrm{digital}} = -\ln(1 - f_{on}) \qquad \textbf{Equation 4.1}$$

$$\mathrm{AEB}_{\mathrm{analog}} = \frac{f_{on} \cdot \bar{I}_{bead}}{\bar{I}_{single}} \qquad \textbf{Equation 4.2}$$

Where f_{on} is the fraction of on-beads bound to the target and $\underline{I}_{bead}$ is the measured fluorescent intensity of the product produced by enzyme-substrate interactions averaged across all beads. The fluorescent intensity of a single enzyme's activity, $\underline{I}_{single}$ is then calculated:

$$\underline{I}_{single} = \sum_i \left(\frac{N_i}{N_{total}} \cdot \frac{f_{on,i} \cdot \underline{I}_{bead,i}}{-ln(1 - f_{on,i})} \right) \quad f_{on,i} < 0.2 \qquad \textbf{Equation 4.3}$$

Where N_i is the number of on-beads for the i-th array with an $f_{on} < 0.2$ and N_{total} is the total number of on-beads for all arrays used. It is assumed that due to the excess of capture beads at low EV concentration that the capture of a single vesicle onto a bead is an independent event - not influenced by the binding of another EV to the same bead or others. When f_{on} is low, there should only be a single enzyme per bead due to Poisson distribution, and equation 2 begins to approach the value of equation 1. When all assumptions are true, the system is considered to be Poisson compliant and AEB_{analog} is a digital parameter for $f_{on} < 0.7$. AEB is a piecewise function[63]:

$$AEB_{piecewise} = \begin{cases} AEB_{digital} = -\ln(1 - f_{on}) & f_{on} \leq 0.7 \\ AEB_{analog} = \frac{f_{on} \cdot \bar{I}_{bead}}{\bar{I}_{single}} & f_{on} > 0.7 \end{cases}$$

Equation 4.4

Due to the large size and natural complexity of EVs, we tested this assumption for the quantification of bdEVs targeting L1CAM, NCAM, and ATP1A3 on the surface of these vesicles and found it to be true under the optimized assay conditions described. Additionally, we evaluated the matrix effects and dosage response of the assay in K2 EDTA plasma and serum.

To validate that EV binding to capture beads remains Poisson-compliant under the assay conditions tested, we performed a bead-saturation experiment using serial additions of NTA-quantified EV stocks to a fixed bead concentration. AEB values calculated via the digital (Equation 1) and analog (Equation 2) branches of the piecewise model converged

within 8% across the linear range (f_{on} = 0.05–0.65), confirming that the Poisson assumption holds for these EV-antibody-bead configurations and that EV polyvalency does not measurably violate independent binding under the reagent excess conditions employed.

4.4.2 Digital Detection of bdEVs Utilizing SiMoA

The functionalized capture beads used for the assay were produced via EDC/SNHS click chemistry to effectively conjugate anti-L1CAM, anti-NCAM, and anti-ATP1A3 antibodies to the bead surface. The coating efficiency of the process was determined by measuring the protein content of the antibody solution before and after conjugation, using UV-vis spectrophotometry with 280 nm wavelength. The surface is then passivated by blocking open regions with BSA. It is important to ensure that the surface is properly passivated to prevent non-specific binding of EVs - especially when using a generic EV detector like CD9, CD63, and/or CD81 in order to prevent a false positive signal. Isotype control beads and NCAM capture beads were each incubated in 1 mL of serum overnight to confirm no significant nonspecific binding (Figure S4.1). The complex surface composition of EVs (glycans, lipids, and proteins) makes them prone to aggregation and adherence via hydrophobic and electrostatic interactions.[140] In order to further reduce nonspecific binding, protein stabilizers such as sugars and nonionic surfactants were used in addition to a zwitterionic buffering agent in the sample diluent to maintain EV integrity.[141-143] All of these actions helped to increase the signal to noise ratio and reduce variability between runs.

For the development of the bdEV quantification assays, we utilized EVs isolated from pooled normal human serum via ultracentrifugation to produce the dosage response curve shown in Figure 4.3. The resulting pellet from ultracentrifugation was resuspended in sample diluent and characterized using nanoparticle tracking analysis (NTA) to determine yield and size distribution (Figure S4.2). The concentrated vesicles were then serially diluted to produce an eight-point standard curve. The particle concentration reported on the x-axis represents the total number of serum-derived vesicles as measured by NTA, including a small subpopulation of bdEVs and other peripherally derived vesicles. We believe that using total serum EVs as the biological reference for assessing the dosage response provides useful feedback on the utility of the assay for the relevant matrices tested. Bulk isolation of total serum EVs also allowed for a more cost-effective generation of reference material that could be used to directly compare sensitivity between each biomarker. EVs derived from neuroblastoma cell conditioned media would be a good alternative, however scaling up cell lines to generate enough material for the entire study was not feasible in this case. Neuroblastoma cells also often overexpress surface markers like L1CAM, NCAM, and ATP1A3 which could potentially lead to an overestimation of the sensitivity.[144-146] Previous work done by other groups suggests that bdEVs make up approximately 1 - 10% of the total EV population in plasma.[147,148] All concentrations reported during analysis here are based on total particle counts - the actual concentration is likely one to two orders of magnitude lower. An alternative method to determine the exact concentration of bdEVs in the reference material would be NanoFCM - this method is low-throughput but enables high resolution single vesicle analysis in clean samples.[149]

Ultimately, isolating very specific subpopulations of EVs for generating "pure" calibration material remains a challenging task and bulk isolation remains as a quick and effective method to generate a dosage response to evaluate assay behavior in the desired matrix.

Note that calibration curves were generated with n=2 technical replicates per concentration point. While this is below the n≥3 for LOD determination, the high reproducibility observed (CV <10%) supports the robustness of the reported values. Prospective clinical studies should employ ≥3 replicates for formal biomarker validation. All LOD and LOQ calculations were performed using established immunoassay guidelines[150], and curve-fitting was performed using unweighted 4-parameter logistic regression (GraphPad Prism 10.0.2; San Diego, CA).

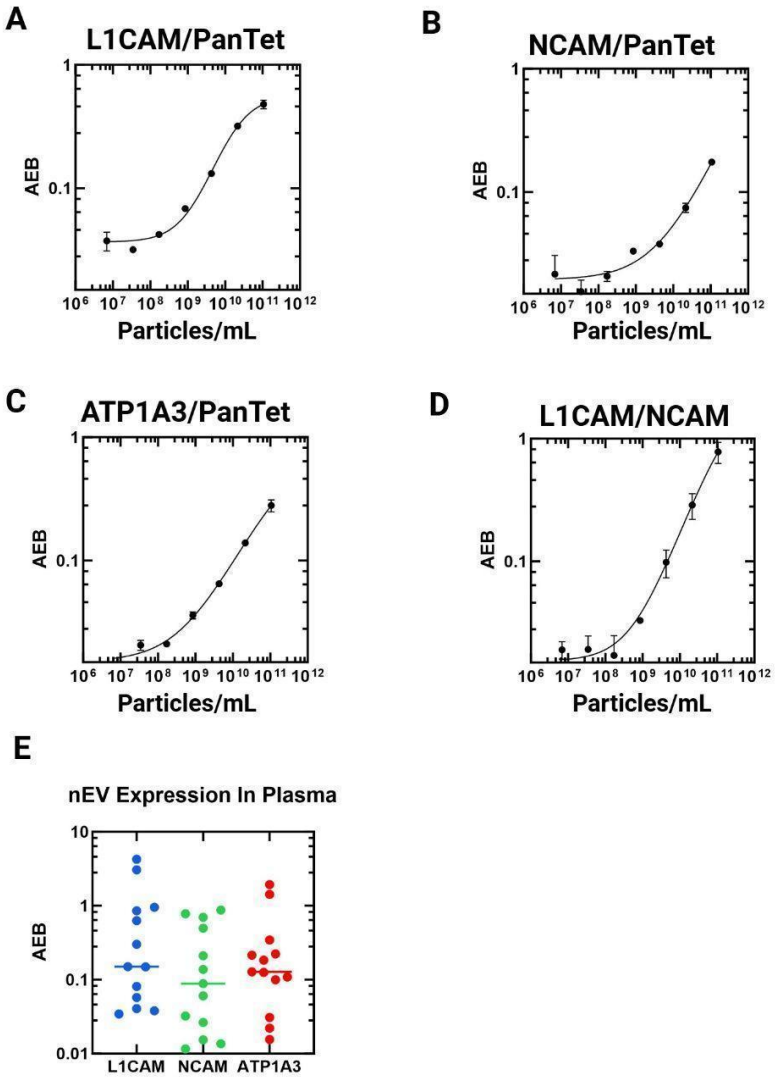

Figure 4.2 Calibration curves produced using normal human serum EVs using the following assay configurations: (A) L1CAM capture, (B) NCAM capture, and (C) ATP1A3 capture. All three curves utilize a mixture of biotinylated anti-CD9, anti-CD63, and anti-CD81 antibodies (PanTet) as the detector. (D) Utilizes L1CAM for capture and biotinylated anti-NCAM as the detector. (E) Normal plasma was depleted of $NCAM^+$ EVs by performing immunoaffinity isolation overnight with the anti-NCAM assay beads. The AEB reported is for the signal produced using an NCAM/CD9 assay configuration. Results indicate that approximately 150 µL (2.1 x 10^8 beads) are required for efficient pulldown. (N = 2 replicates). (F) The relative distribution of each bdEV marker in plasma is shown for 12 normal individuals as measured using PanTet detection and a 4X dilution factor.

A pan-tetraspanin cocktail (CD9, CD63, and CD81) was used as the detector for Figures 4.3A-C to generate a dosage response against serum-derived EVs. The resulting curves were fit using unweighted 4-parameter logistic regression to model the sigmoidal dosage response. Based on an eight point curve and two technical replicates for each concentration, the lowest reported LOD was determined to be 1.03 x 10^7 particles/mL for the NCAM assay (Figure 4.2B). This was calculated by multiplying 3.3 times the standard deviation of the blank plus the mean blank signal (Equation S1). The LOQ, representing the lowest concentration at which the analyte could be reliably quantified with acceptable precision, was established as 3.3 times the LOD (Equation S2). For NCAM, the LOQ was determined to be 2.75 x 10^9 particles/mL. This placed > 76% of normal plasma samples we tested (8 out of 13) above the LOD (Figure 4.2E). In comparison, ATP1A3 capture had a slightly higher reported LOD of 1.21 x 10^7 particles/mL and LOQ of 1.41 x 10^{10} particles/mL (Figure 4.2C). ATP1A3 observed > 92% of the same plasma samples tested were above the LOD (Figure 4.2E). L1CAM capture had the highest established LOD of 4.33 x 10^8 particles/mL for PanTet detection (Figure 4.2A) which resulted in > 76% of the plasma samples being above the LOD. The LOQ of this assay was determined to be 5.73 x 10^9 particles/mL. Alternatively, NCAM was tested as a potential detector in combination with L1CAM capture to increase the specificity of the assay. The reported LOD utilizing NCAM detection was 5.44 x 10^8 particles/mL and the LOQ was 4.63 x 10^9 particles/mL (Figure 4.2D). The coefficient of variation (CV) for each standard curve using pan-tetraspanin detection was < 10%. The CV of the standard curve produced using NCAM detection increased to < 20%. Overall, ATP1A3 was capable of being positively identified in more

normal plasma samples than L1CAM and NCAM. NCAM capture however showcased superior sensitivity due to a higher signal-to-noise ratio. NCAM detection significantly increased the signal-to-noise ratio by reducing the signal dilution due to peripheral EVs, however the sensitivity suffered from higher replicate variability. The superior clinical detection rate of ATP1A3 is mechanistically consistent with its topology as a ten-transmembrane-domain Na^+/K^+-ATPase α-subunit.[24] Unlike L1CAM, which undergoes ADAM10-mediated ectodomain shedding, generating soluble forms that compete with EV-bound protein for capture bead binding and NCAM, which exists in 120 kDa membrane-anchored and 65–105 kDa soluble isoforms, ATP1A3 lacks extracellular cleavage sites and therefore exists almost exclusively in a membrane-embedded form. This structural feature concentrates its accessible epitopes on intact vesicle surfaces, producing a higher signal-per-particle and reducing competition from non-vesicular protein in plasma.

To confirm that the assay signal arises from co-localization of neuronal capture and pan-EV detector markers on intact vesicles rather than from independently adsorbed proteins, we treated EV samples with 1.0% (v/v) Triton X-100 prior to assay. Detergent solubilization of the EV lipid bilayer reduced signal by > 90% relative to untreated controls, consistent with disruption of the vesicle membrane releasing membrane-anchored marker proteins and abolishing the co-localization event required for bead capture (Figure S4.3). This confirms that the assay reports on intact, membrane-enclosed EVs bearing co-expressed neuronal and pan-EV surface markers.

4.4.3 Assessment of Linearity and Dynamic Range

The linearity of the assay's response was evaluated in both normal human serum and K2 EDTA plasma to assess matrix effects and establish the valid minimum required dilution (MRD). Samples were prepared in a 2X serial dilution ranging from 2X to 64X and analyzed in duplicate. The linear response region for each assay is shown in Figure 4.4.

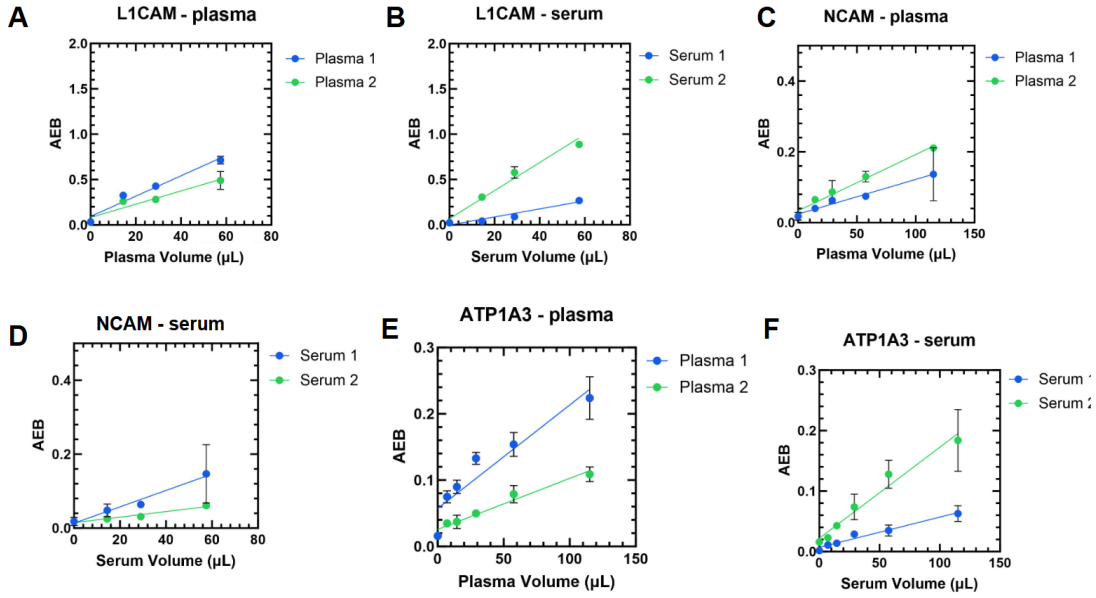

Figure 4.3 Dilutional linearity was assessed across normal serum and K2 EDTA plasma samples using 2 technical replicates for each sample. A pan-tetraspanin cocktail (CD9, CD81, and CD63) was used as the detector. The sample volume shown on the x-axis is the total volume of sample added to each well. The final well volume was 230 µL.

For both matrices using L1CAM capture and PanTet detection, clear linearity was observed starting at the 4X dilution and extended into the 16X dilution (Figure 4.3A and 4.3B). NCAM capture had a greater linear region in plasma than serum. In serum, the linear range for NCAM capture was observed to be between a 2X and 8X dilution. In contrast, NCAM in plasma responded linearly between a 2X to 16X dilution (Figure 4.3C and 4.3D). The

coefficient of variation between replicates for NCAM and L1CAM quantification was exceptional with less than 5% for both serum and plasma. ATP1A3 capture beads were determined to have the same linear range in both matrices of 2X to 16X dilution (Figure 4.3E and 4.3F). The coefficient of variation between replicates for this marker were acceptable in plasma being less than 15%, but in serum the variation between replicates was larger around 20%. The average AEB values and their standard deviations are reported in Tables 1 - 3. These results indicate that all 3 markers are capable of accurately quantifying bdEVs in biofluids. In particular, L1CAM and NCAM show exceptional robustness in plasma and serum. For plasma, we recommend an MRD of 2X for both NCAM and ATP1A3 capture assays. ATP1A3 also works well with an MRD of 2X in serum. A higher MRD of 4X is recommended for NCAM quantification in serum. For L1CAM capture, the recommended MRD is 4X for both plasma and serum.

Note that the matrix-dependent differences in MRD between serum and plasma likely reflect the distinct protein and EV compositions of these biofluids. Serum, produced by coagulation, undergoes platelet degranulation and fibrinogen cleavage, releasing fibrin degradation products and platelet-derived EVs that may compete for non-specific binding sites on the capture bead surface. The higher soluble protein burden in serum (particularly fibronectin and vitronectin, which adsorb non-specifically to beads) may account for the higher MRD requirement observed for NCAM in serum. Future studies should directly compare the protein and EV corona compositions of serum versus EDTA plasma to mechanistically confirm this hypothesis.

Table 4.2 L1CAM Parallelism using PanTet Detector (n=2).

	Plasma		Serum	
Dilution Factor	**P1**	**P2**	**S1**	**S2**
2X	0.628 ± 0.021	0.950 ± 0.015	1.02 ± 0.039	0.950 ± 0.015
4X	0.491 ± 0.099	0.714 ± 0.042	0.268 ± 0.009	0.714 ± 0.042
8X	0.280 ± 0.021	0.428 ± 0.002	0.057 ± 0.012	0.428 ± 0.002
16X	0.261 ± 0.006	0.326 ± 0.022	0.040 ± 0.012	0.326 ± 0.022
32X	0.158 ± 0.008	0.206 ± 0.021	0.0382 ± 0.003	0.206 ± 0.021
64X	0.066 ± 0.04	0.145 ± 0.013	0.005 ± 0.005	0.145 ± 0.013
Blank	0.023 ± 0.001			

Table 4.3 NCAM Parallelism using PanTet Detector (n=2)

	Plasma		Serum	
Dilution Factor	**P1**	**P2**	**S1**	**S2**
2X	0.137 ± 0.012	0.211 ± 0.005	0.827 ± 0.068	0.088 ± 0.005
4X	0.075 ± 0.009	0.130 ± 0.015	0.147 ± 0.079	0.061 ± 0.009
8X	0.063 ± 0.005	0.087 ± 0.032	0.064 ± 0.009	0.031 ± 0.003
16X	0.040 ± 0.001	0.065 ± 0.004	0.048 ± 0.017	0.025 ± 0.003
32X	0.035 ± 0.003	0.060 ± 0.001	0.030 ± 0.002	0.018 ± 0.005
64X	0.024 ± 0.001	0.040 ± 0.008	0.039 ± 0.002	0.017 ± 0.001
Blank	0.018 ± 0.011			

Table 4.4 ATP1A3 Parallelism using PanTet Detector (n=2)

	Plasma		Serum	
Dilution Factor	**P1**	**P2**	**S1**	**S2**
2X	0.224 ± 0.032	0.109 ± 0.011	0.063 ± 0.013	0.184 ± 0.051
4X	0.154 ± 0.018	0.079 ± 0.013	0.035 ± 0.009	0.128 ± 0.023
8X	0.133 ± 0.009	0.050 ± 0.005	0.029 ± 0.001	0.074 ± 0.021
16X	0.090 ± 0.010	0.037 ± 0.010	0.014 ± 0.002	0.043 ± 0.005
32X	0.073 ± 0.009	0.0350 ± 0.002	0.011 ± 0.001	0.023 ± 0.001
64X	0.028 ± 0.002	0.029 ± 0.001	0.011 ± 0.001	0.028 ± 0.002
Blank	0.016 ± 0.003			

One potential reason for L1CAM requiring a higher MRD than NCAM and ATP1A3 is the potential presence of soluble L1CAM that is not associated with the surface of EVs. Previous work done by *Walt et al.* has suggested that L1CAM is not a reliable marker for bdEV isolation.[151] Though it is widely used as a biomarker to isolate neuronal-derived EVs, it has been found to be expressed outside the brain and is present in cleaved and alternatively spliced forms in plasma and CSF. The presence of soluble L1CAM in plasma and serum would require a higher MRD in order to reduce the matrix effect and the likelihood of the soluble protein saturating the surface of the bead. This is also supported by the greater observed LOD in Figure 4.3 by L1CAM. In contrast, NCAM and ATP1A3 have been found to be potentially better alternatives. NCAM is present in its soluble form at much lower concentrations. ATP1A3 is a multipass integral membrane protein that lacks the proteolytically cleavable extracellular domains seen on L1CAM and NCAM.[152] It is

also almost exclusively expressed in the brain, with very low, specific expression in heart muscles.[153]

4.5 Conclusion

This study demonstrates the successful development and validation of a digital SiMoA framework for the sensitive quantification of bdEVs directly from complex clinical matrices such as plasma and serum. By implementing a piecewise model for AEB determination, we confirmed that the inherent polyvalency and large size of EVs does not compromise the key Poisson distribution assumptions required for digital quantification. Our results indicate that while L1CAM, NCAM, and ATP1A3 are all viable targets for bdEV capture, they exhibit distinct analytical profiles influenced by their biological states in circulation.

Specifically, ATP1A3 demonstrated superior clinical utility, with detection levels above the LOD in > 92% of normal plasma samples, likely due to its status as a multipass integral membrane protein that lacks the soluble, proteolytically cleaved isoforms that confound L1CAM and NCAM assays. While NCAM exhibited the highest sensitivity and signal-to-noise ratio, L1CAM required a higher MRD of 4X, suggesting a significant presence of non-vesicular soluble protein in the matrix. The achieved LOD of 1.03×10^7 particles/mL for NCAM-capture SiMoA is comparable to the detection limits reported for NanoFCM single-particle flow cytometry and represents a 10-100-fold improvement over conventional sandwich ELISA formats applied to EV quantification. Critically, unlike NanoFCM, this sensitivity is achieved directly in diluted clinical matrices (serum and

plasma) without prior EV isolation, ultracentrifugation, or size enrichment which substantially reduces assay complexity, time, and the inter-laboratory variability introduced by isolation-dependent workflows.

Furthermore, we established that using pooled serum-derived EVs as a biological reference material provides a cost-effective and matrix-matched alternative to cell-line-derived standards that may better reflect the physiological challenges of clinical diagnostics. The high degree of dilutional linearity and low coefficients of variation (typically < 10%) across these assays underscore the robustness of the SiMoA platform for longitudinal monitoring. Ultimately, this work provides a standardized, high-throughput solution for the direct profiling of neural biomarkers, offering a critical tool for the advancement of liquid biopsies in neuro-oncology and neurodegenerative disease.

Several limitations of this study merit consideration. First, the calibration standards were generated from total serum-derived EVs, which contain only a minor bdEV subpopulation; the absolute concentration of bdEVs in the reference material was not independently determined, precluding absolute quantification in molar or copy-number terms. Second, all clinical samples were derived from healthy donors; the assay's performance in disease states with altered EV biogenesis, cargo loading, or surface marker expression (e.g., AD, TBI, glioblastoma) remains to be characterized. Third, n=2 technical replicates per standard point represent a preliminary validation; confirmatory studies should meet CLSI EP17-A2 requirements prior to full clinical implementation. Finally, the long-term stability

of conjugated capture beads and detector antibodies under clinical laboratory storage conditions requires systematic evaluation before clinical deployment.

Looking forward, the modular architecture of the SiMoA bead conjugation system is inherently compatible with multiplexed profiling simultaneously quantifying ATP1A3^{+}, NCAM^{+}, and L1CAM^{+} EV subpopulations in a single reaction to generate marker-specific bdEV fingerprints. Such multiplexed fingerprinting could enable differential diagnosis of neurodegenerative diseases with partially overlapping EV phenotypes (e.g., Alzheimer's vs. Parkinson's disease vs. frontotemporal dementia) or tracking of treatment response in neuro-oncology. Combined with cargo profiling (miRNA, lncRNA, or intra-vesicular *tau* within immunocaptured bdEVs), this platform offers a path toward a comprehensive, single-tube CNS liquid biopsy.

4.6 Supporting Information

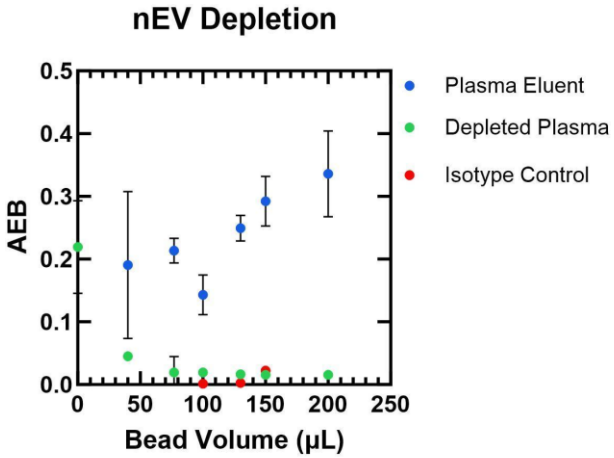

Figure S4.1 The total yield of EVs isolated via overnight immunoaffinity isolation was compared between NCAM and a mouse IgG isotype control bead. Beads were incubated overnight with 1 mL of plasma prior to the EVs being eluted off the surface and analyzed using an NCAM capture and CD9 detection assay. The AEB produced by both eluents

was analyzed. NCAM capture beads depleted the plasma of any detectable NCAM EVs. In contrast, the isotype control eluent yielded no detectable signal.

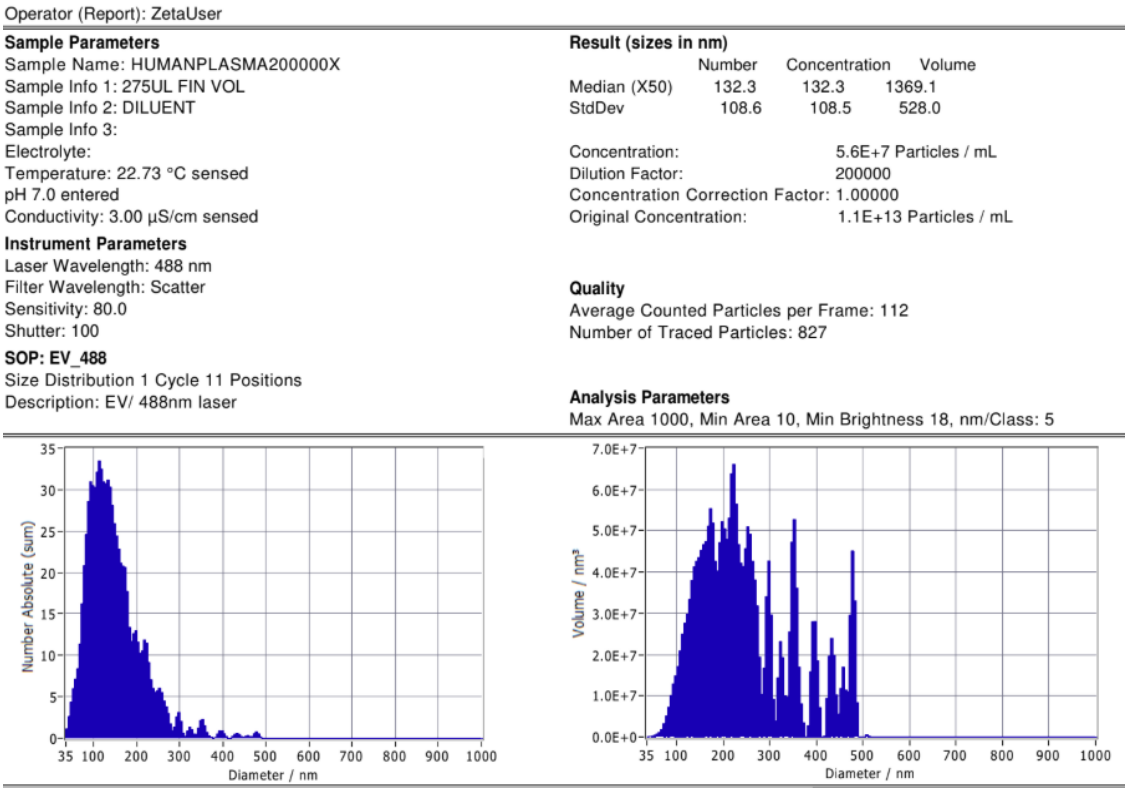

Figure S4.2 A Malvern ZetaView instrument was used to measure the yield of EVs isolated from pooled normal human serum via ultracentrifugation. The resulting pellet was resuspended in EV sample diluent and aliquoted prior to storage.

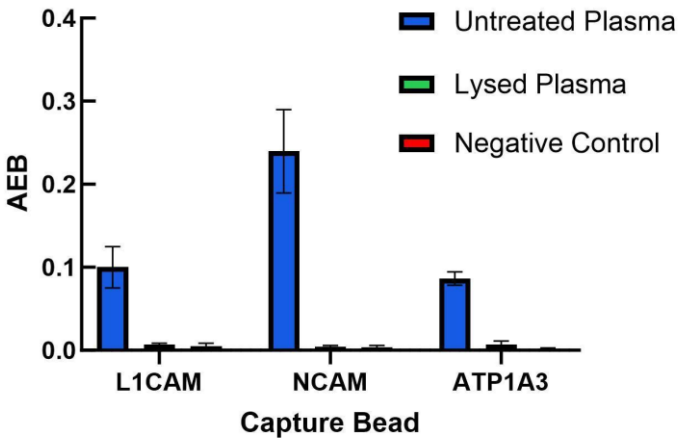

Figure S4.3 The specificity of the assay for intact, membrane-enclosed EVs and not solubilized protein was tested by comparing the signal between untreated plasma (4X dilution) and plasma treated with 1% Triton X-100. The resulting AEB is reported here using a pan-tetraspanin detector. The significant decrease in AEB after lysis indicates that solubilized protein does form a detectable immunocomplex.

To evaluate the sensitivity of each assay the limit of detection (LOD) and limit of quantification (LOQ) were calculated using the following equations as per ICH Q2(R2) guidelines:

$$LOD = 3.3 \times \frac{\sigma}{S} + AEB_{blank} \qquad \textbf{Equation S4.1}$$

$$LOQ = 3.3 \times LOD \qquad \textbf{Equation S4.2}$$

4.7 Acknowledgements

3.7.1 Funding Statement

This work was completed with funding provided in part by Quanterix Corporation, Brown University Graduate School, and the Zimmerman Innovation Award for Brain Science from the Carney Institute for Brain Science.

4.7.2 Author Contributions

J.P., A.T., and K.M., contributed to the conceptualization, supervision, and administration of the project. J.P, C.Y., E.J., J.M., and A.F. contributed to investigation and formal analysis. J.P. designed methodology and contributed to the validation, curation, and

visualization of the data. J.P. and A.T. acquired the funding. J.P. and A.T.. wrote the first draft. J.P., A.T., and K.M. reviewed and edited the manuscript.

The authors would also like to gratefully acknowledge Dr. Sicheng Wen and Mandy Pereira, M.S. from the COBRE Extracellular Core Facility at Brown University Health for their guidance and help with EV isolation and NTA analysis. They also thank Dr. Kristine Pelton from Brown University's Fluid Biomarker Core Facility for completing the Mesoscale Discovery experiments. They also give special thanks to Sarah Planchak, M.S. for her work culturing the glioblastoma spheroids and supernatant collection. Mingwei Zhao from Quanterix Accelerator services also helped with troubleshooting technical difficulties.

4.7.3 Conflict of Interest Statement

The authors declare that they have no competing interests. All contributions from authors associated with Quanterix are strictly scientific. The work does not aim to promote or endorse any commercial product.

CHAPTER 5:
High-Sensitivity Analysis of Brain and Glioblastoma-Derived EV Cargo: A Framework for Subtype-Specific Biomarker Discovery

---

Chapter 5 has been submitted as an original research article and is currently under review.

Jennifer M. Pollock[1], Connor H. Yew[1], Everett Gutterman-Johns[1], Julia Miller[1], Anji Friedbauer[1], Mingwei Zhao[2], Kishore Malyavantham[2], and Anubhav Tripathi[1]

1. Center for Biomedical Engineering, School of Engineering, Brown University, Providence, RI, USA
2. Quanterix Corporation, Billerica, MA 0821, USA

5.1 Abstract

This study investigates the proteomic characteristics of brain-derived extracellular vesicles (bdEVs) and compares them to EVs from cultured glioblastoma (GBM) spheroids, with an aim to improve EV-based biomarker analysis. We first developed a configurable SiMoA assay that quantified bdEVs isolated from normal plasma based on three key bdEV markers: NCAM, L1CAM, and ATP1A3. Our analysis revealed no significant difference in the relative concentration or distribution of EVs isolated by these three markers in normal plasma. In contrast, GBM-EVs showed a higher expression of CD63 compared to normal bdEVs, suggesting a potential signature phenotype of cancer-derived EVs. To further explore the biomarker potential of bdEVs and GBM-EVs, we also assessed the average loading density of four critical neurodegenerative disease biomarkers: amyloid-beta 40 (Aβ-40), amyloid-beta 42 (Aβ-42), neurofilament light chain (NfL), and glial fibrillary acidic protein (GFAP). We found that $NCAM^+$ EVs from normal plasma had a greater average loading density for each of these four proteins compared to $CD9^+$ EVs. This suggests that targeting specific EV subtypes, such as those of neuronal origin, may enhance biomarker detection sensitivity. Finally, GBM-derived EVs isolated from cell culture contained significantly more GFAP per vesicle than EVs from normal plasma. Together, these findings establish a proof-of-concept framework for EV subtype-specific profiling using SiMoA, highlighting the potential of GFAP and CD63 as candidate markers for future patient-based studies of central nervous system pathologies. Although this work does not yet include patient-derived samples, this work is essential to direct translation to clinical diagnostics through validation in disease cohorts

5.2 Introduction

Extracellular vesicles (EVs) are a diverse population of nanoscale, membrane-bound vesicles secreted by almost all cell types. They play a critical role in intercellular communication by transporting bioactive cargo composed of proteins, lipids, and nucleic acids to recipient cells.[132,154,155] This biological signaling is a fundamental process in maintaining homeostasis within the body and the spread of disease, making EVs a subject of intense research in recent years[156].

From a diagnostic perspective, EVs are a revolutionary liquid biopsy tool. As they can be found in all biofluids and obtained non-invasively (Figure 5.1).[157] The cargo of EVs reflects the state of their parent cells, providing a dynamic snapshot of physiological or pathological conditions.[158,159] This allows for the detection of disease-specific biomarkers for conditions ranging from cancer to neurodegenerative disorders, often long before clinical symptoms appear. In particular, brain-derived EVs in blood can provide a window into the central nervous system, offering a non-invasive way to diagnose and monitor brain diseases.[159-161]

Despite these advances, a critical gap remains in the field: most EV-based biomarker studies either rely on bulk plasma EV populations dominated by platelet and red blood cell-derived vesicles, or require extensive purification steps that introduce pre-analytical variability. Brain-derived EVs (bdEVs) represent a minority subpopulation of circulating vesicles, and methods to specifically enrich and phenotype them with high sensitivity

remain underdeveloped. While SiMoA has been used to quantify total EV populations in cancer, its application to neuronal EV subtyping using multiple brain-specific capture antibodies in a configurable, modular format has not been systematically characterized.[162] The primary contribution of this work is therefore a methodological exploration of potential analytical frameworks for EV analysis utilizing SiMoA technology: we develop and benchmark a configurable SiMoA assay for bdEV immunophenotyping, assess the relative utility of three brain-specific markers (L1CAM, NCAM, ATP1A3) for bdEV isolation, and evaluate the differential loading density of these EV subpopulations for neurodegenerative disease biomarkers. Comparisons with GBM-EVs derived from primary cell spheroids are presented as first proof-of-concept observations, with the explicit caveat that cell-line-derived EVs and circulating plasma EVs represent distinct biological systems.

In research, EVs serve as a powerful model to study disease mechanisms. Their ability to transfer pathogenic proteins or genetic material between cells helps researchers understand how diseases, such as glioblastoma, spread and become resistant to therapy.[163,164] By analyzing the unique molecular signature of EVs, scientists can uncover novel therapeutic targets and develop more effective treatments.[164] The study of EVs is rapidly advancing, with the potential to transform both diagnostics and therapeutics.

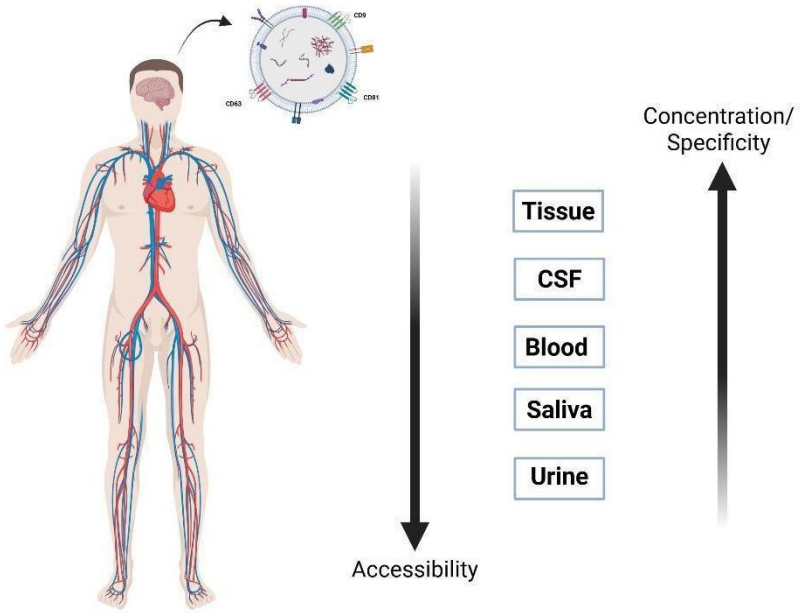

Figure 5.1 Diagram showcasing the utility of EVs as a potential biomarker for disease. It describes the inverse relationship between concentration and specificity compared to accessibility of EVs in the body. (Images created with Biorender.com) This framework motivates the use of brain-specific immunoaffinity capture, which enriches for the low-abundance, high-specificity bdEv subpopulation directly from plasma without the purification steps that reduce yield and introduce variability at the lower-concentration, higher-specificity end of this spectrum.

Glioblastoma multiforme (GBM) is the most common and aggressive primary brain tumor in adults, characterized by a dismal prognosis and a median survival of just over a year.[165,166] The highly invasive nature of GBM and its unique tumor microenvironment pose significant challenges for diagnosis and therapy. A crucial component of this microenvironment is the intricate intercellular communication network mediated by EVs.[167] GBM derived EVs (GBM-EVs) are now recognized as key players in promoting tumor growth, invasion, and angiogenesis, and in suppressing the anti-tumor immune response.[168,169] Their protein cargo represents a rich source of biological information and by analyzing the protein composition of these EVs, researchers can gain new insights into

the specific molecular mechanisms driving GBM pathology in order to better address disease heterogeneity.

This study aims to comprehensively characterize the surface profile and cargo of GBM-EVs compared to normal plasma EVs. We hypothesize that GBM-EVs contain a distinct proteomic signature that reflects their glial cell of origin, and that this signature can be detected and quantified using our SiMoA-based platform. We emphasize that the GBM-EVs used in this study are derived from primary cell spheroids maintained in vitro and therefore differ fundamentally from EVs shed by tumor cells in the complex in vivo tumor microenvironment or collected from patient plasma. As such, the findings presented here should be interpreted as observations rather than validated biomarker evidence. A blood-based analysis of GBM-EV proteins could provide a non-invasive liquid biopsy for early diagnosis, enable real-time monitoring of disease progression, and predict treatment response or resistance. A more thorough understanding of the GBM-EV proteome could lead to the identification of novel therapeutic targets, paving the way for more effective and personalized treatments.

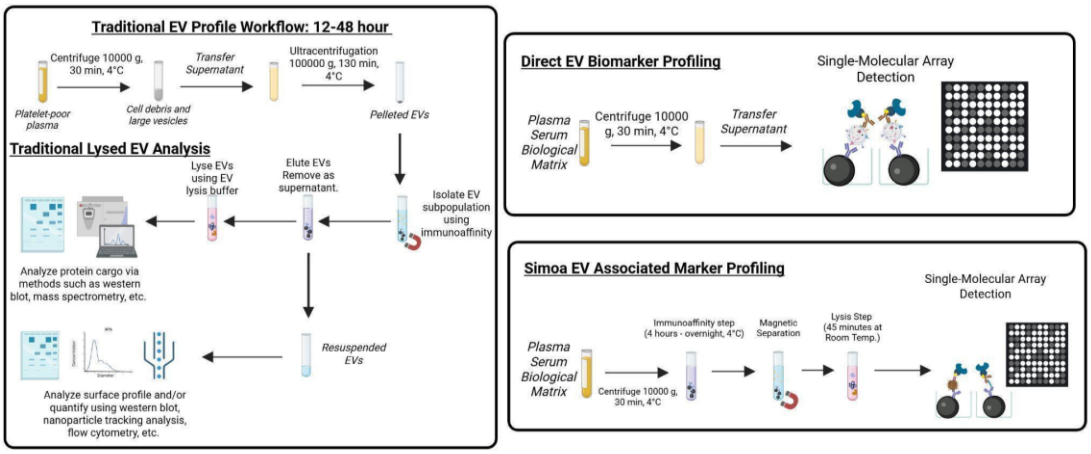

Figure 5.2 Schematic showcasing the streamlined workflow for EV analysis utilizing SiMoA compared to a traditional workflow using ultracentrifugation to isolate EVs prior to analysis. (Created with Biorender.com)

This study also aims to evaluate a simplified and robust method for immunophenotyping EVs using a single-molecule detection array (SiMoA)(Figure 5.2). SiMoA is a novel, ultrasensitive digital ELISA that can quantify analyte concentrations with femtomolar sensitivity.[170] Previous studies have explored the utility of this technology to measure plasmatic levels of $CD63^+$ EVs in colorectal and breast cancer patients without the need for sample purification.[117,171] As it is more difficult to obtain tissue biopsies from brain cancers for diagnosis, bdEVs are a perfect candidate for further study. Circulating bdEVs can provide valuable cellular snapshots of disease progression in the brain without the need for invasive biopsies.

Our findings seek to demonstrate that two cell adhesion molecules, L1CAM and NCAM, and ATPase Na+/K+ transporting subunit alpha 3 (ATP1A3), are found localized on the

surface of bdEVs at comparable levels, thus supporting their reliability as brain specific markers for immunocapture-based EV isolation.[124]

Additionally, we observed the presence of neurodegenerative biomarkers, amyloid-beta 40 (Aβ-40), amyloid-beta 42 (Aβ-42), neurofilament light chain (NFL), and glial fibrillary acidic protein (GFAP), carried with bdEVs. These proteins are of great interest to the neurodegenerative community and highlight the ability of EVs to transport precious cargo across the blood-brain-barrier.[172-174] By leveraging SiMoA, this study seeks to refine the workflow for high-sensitivity isolation and characterization of bdEVs, ultimately working towards advancing bdEV applications in research and clinical diagnostics. Standardizing bdEV profiling methods could enable the earlier detection of neurological diseases and disorders, increase the potential for targeted therapies, and provide insight into disease pathology.

5.3 Materials and Methods

5.3.1 Glioblastoma Spheroid Culture and EV Collection

Primary human glioblastoma cells were obtained following surgical removal from patient brain tumors at the Rhode Island Hospital under Institutional Review Board IRB #418015. In order to form spheroids, the isolated cells were placed in non- coated 60 mm dishes at an initial seeding density of 1 million cells per dish and harvested after 5 days. A complete medium was created for culturing the primary cell spheroids and consisted of

1× Neurobasal A, 2 mM GlutaMAX-I, 100X Antibiotic-Antimycotic, 20 ng/mL bFGF and EGF, B-27-A, and heparin.

5.3.2 Quanterix SiMoA EV Assays

In a 96-well plate, 50ul of sample, such as plasma or glioblastoma cell media, was diluted 2X with 50 uL of EV Sample Diluent. The diluted sample was then incubated for 45 minutes at 30°C and 800 rpm with 25 uL of capture beads (coated with indicated antibodies) and 25 uL of biotinylated detector antibody. The plate was then placed into a microplate washer and incubated for an additional 10 minutes with 200pM streptavidin β-galactosidase. Following a second wash on the microplate washer, the well-plate and resorufin β-galactopyronoside were loaded into the SR-X for analysis. The kit instructions for the Neurology 4-Plex E assay (Quanterix, Billerica, MA, USA, cat. no. 103670) were followed directly to quantify the presence of Aβ-40, Aβ-42, NfL, and GFAP in the EV lysates.

5.3.3 Immunoaffinity Isolation

Pooled and individual healthy donor samples, collected previously using EDTA collection methods (BioIVT, Westbury, NY, USA), were thawed at room temperature for 30 minutes prior to centrifugation for 10 minutes at 5000g. For optimal isolation, 1 mL aliquots of plasma were mixed overnight at 4°C with 1.95 x 10 8 capture antibody coated beads. After the overnight isolation, the beads were washed three times with filtered PBS and EVs were

eluted using 0.1M glycine HCl solution (pH = 2.5). The eluent was then neutralized with 1M NaOH prior to analysis.

5.3.4 Ultracentrifugation

First, 250ul of plasma was centrifuged at 300xg for 10 minutes at 4ºC. Supernatant was collected and transferred to a sterile protein lo-bind tube, where it was diluted with cold 1X PBS, before being spun for 30 minutes at 10,000xg, with no brake during deceleration so as not to disturb the EV pellet that formed form. This supernatant was removed and the pellet was resuspended in 1X PBS. The solution was then centrifuged at 100,000xg for 2 hours. Lastly, following the 100k centrifugation, the pellet was resuspended in 150ul of cold PBS and stored at -80ºC until use.

5.3.5 EV Lysis

EVs were lysed after elution using a final concentration of 2% CHAPS and 1% Triton X-100. Briefly, 14 uL of 10% CHAPS + 5% Triton X-100 + 10X Protease Inhibitor solution was added to 56 uL of EVs and incubated at room temperature for 45 minutes. Samples were vortexed for 30 seconds once every 15 minutes. After lysis, the samples were diluted to a final volume of 230 uL using the Neurology 4-Plex E plasma sample diluent.

5.3.6 Nanoparticle Tracking Analysis

All samples were diluted 100X in PBS to a final volume of 1 ml. Camera settings were set according to the manufacturer's software manual (NanoSight NS300 User Manual, MAN0541-01-EN-00, 2017) and autofocus was adjusted to avoid indistinct particles. For each measurement, 3 30-sec videos were captured under the following conditions: cell temperature: 20°C; Syringe speed: 50 µl/s. Image analysis was completed using the built in NanoSight software.

5.4 Results and Discussion

5.4.1 Development of a SiMoA Assay for Cell Conditioned Media and Plasma

To enable the highly sensitive quantification of EVs, we developed a configurable bead-based immunoassay using SiMoA technology. This assay employed a capture antibody immobilized on 2.7 um paramagnetic beads to isolate EVs, followed by a biotinylated antibody for the direct detection of EVs in biofluids. We focused our experiments on utilizing anti-CD9 and anti-CD63 antibodies to quantify total EVs in normal EDTA plasma and from glioblastoma cell conditioned media. The standard curves produced by the assay are shown in Figure 5.3 and were fitted using 4 parameter logistic curve regression.

The first configuration utilizes a homogeneous pair of anti-CD9 antibodies as the capture and detector to target the extracellular portion of CD9 exposed on the surface of vesicles (Figure 5.3a). The second configuration utilizes the same anti-CD9 bead as the capture probe, followed by anti-CD63 as the detector. The anti-CD9 capture and detector pair was

observed to have the lowest detection limit (LOD = 8.5 x 10^6 EV/mL) across any configuration tested (Figure S5.1). It is important to note that the EV concentrations used to define these standard curves were determined by NTA, which measures total particle counts and does not discriminate between EV subtypes or between EVs and co-isolated non-vesicular particles. The LOD values reported here therefore represent the detection sensitivity for the total particle population and should not be interpreted as the sensitivity for any specific EV subtype or surface marker. The functional sensitivity of the assay for biologically relevant EV targets in heterogeneous samples will depend on the abundance of the specific marker being captured and would require further calibration with marker-specific standards. This supports earlier findings that have reported CD9 to be the most abundant surface marker of the three tetraspanins commonly used to identify EVs – CD9, CD63, and CD81.[39] To verify that the signal is indeed specific to whole EVs and not just free-floating protein, the assay was tested against lysed EVs. There was no signal or dose response (Figure S5.2).

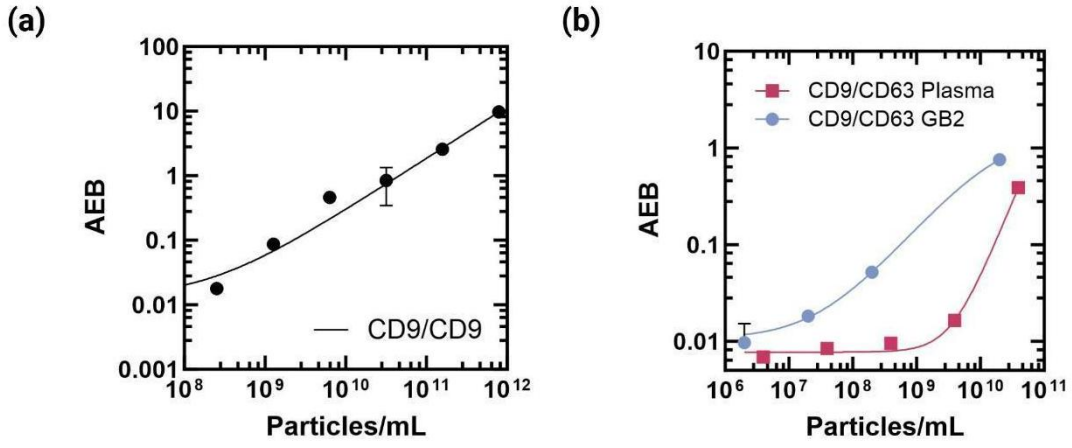

Figure 5.3 (a) Calibration curve of the SiMoA EV assay using anti-CD9 capture beads and anti-CD9 detector. The detection limit was determined to be 8.5 x 10^6 EV/mL. (b) Calibration curve of the SiMoA EV assay using anti-CD9 capture beads and anti-CD63 detector. The limit of detection for the CD9/CD63 assay using plasma EV standards is 1.76 x 10^9 EVs/mL (CV = 4.8%). The limit of detection for EVs isolated from glioblastoma cell media (GBM-EVs) is 1.28 x 10^7 EVs/mL (CV = 18.3%). EVs were isolated from pooled normal EDTA plasma or cell conditioned media via ultracentrifugation and resuspended in 1X PBS. The final concentration was confirmed using NTA (Figure S5.3 and Figure S5.4)

GBM-EVs exhibited a large increase in signal compared to normal plasma derived EVs at the same concentration (Figure 5.3b), subsequently lowering the LOD more than 2 orders of magnitude from 1.76 x 10^9 EVs/mL to 1.28 x 10^7 EVs/mL. The higher signal observed for the GBM-EVs can likely be attributed to an increased expression of CD63, as cancer cells are known to differentially express surface proteins.[175,176] CD63 is known for performing multiple functions including cell activation, adhesion, intracellular trafficking communication. For the GBM-EVs used in our experiments, an elevated CD63 density on the surface of tumor-derived vesicles contributed to greater average enzymatic activity per bead (AEB), resulting in a higher overall signal for the cancer EV population.

5.4.2 Assay Validation Using NTA

To validate the SiMoA results, a subset of samples (n = 3) was analyzed using NTA to determine the total particle concentration. The concentration of EVs measured using the homogeneous SiMoA CD9 assay showed a strong correlation with the total EV concentration measured by NTA ($R2 = 0.9950$, $p < 0.05$). These results provide confidence in the accuracy and reliability of the developed SiMoA assay for EV quantification and characterization (Figure S5.4)**.**

5.4.3 Relative Distribution of Tetraspanins

It was hypothesized that the increase in AEB for GBM-EVs was the result of an increase in CD63 expression.[177] To test this, the tetraspanin phenotype of normal plasma EVs was compared to GBM-EVs using the SiMoA EV assay we developed. The modular nature of the assay was utilized to measure the signal strength produced by each tetraspanin. A cocktail of all three tetraspanins (PanTet) was used as the capture probe, as well as three brain-derived EV (bdEV) markers used individually (Figure 5.4). Despite a wide variance in EV concentration across the cohort, CD9 consistently had the greatest signal followed by CD81 then CD63 regardless of the capture probe used (Figure 5.4).

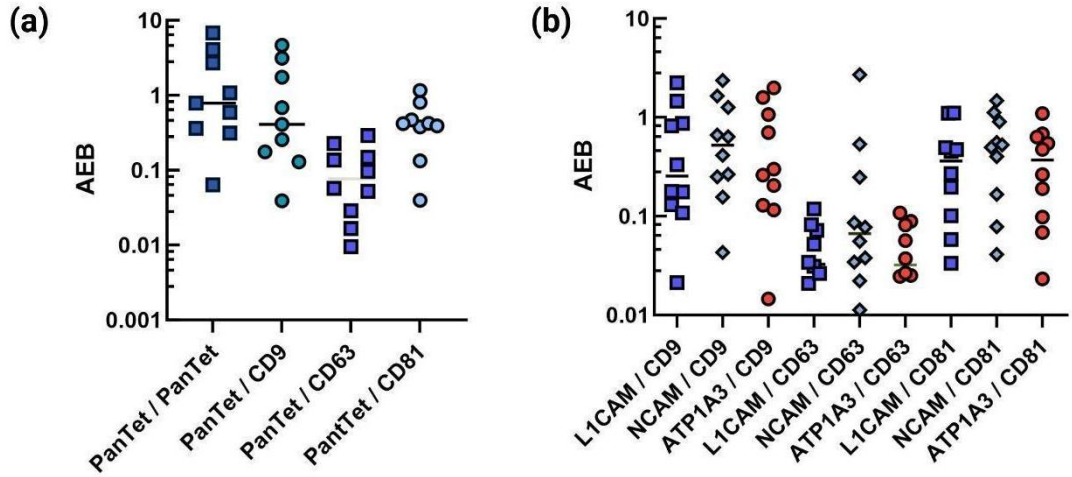

Figure 5.4 Reported average enzymatic activity (AEB) from 50 uL of normal EDTA plasma showcasing the relative distribution of tetraspanins on the surface of (a) general plasma EVs isolated using a mix of anti-CD9, anti-CD63, and anti-CD81 affinity beads. (b) AEB from 50 uL of normal EDTA plasma showcasing the relative distribution of tetraspanins on the surface of bdEVs isolated using either L1CAM, NCAM, or ATP1A3 (as indicated). (n = 9 normal individual EDTA plasma samples).

The relative distribution of each tetraspanin was calculated using the following:

$$\%\ distribution = 100\ \times \left(\frac{individual\ AEB}{\sum\ individual\ AEB}\right) \qquad \textbf{Equation 1}$$

and the results are shown in Figure 5.5. This approach allowed us to determine the distribution of each marker across the total EV population. The normal EDTA plasma cohort demonstrated an average distribution in which 53% of captured EVs were positive for CD9, 9% for CD63, and 37% for CD81. We observed similar distributions across the normal plasma cohort (n=9), suggesting a consistent tetraspanin profile in healthy individuals. The assay was then applied to GBM-EVs, which revealed a distinct tetraspanin signature with a higher proportion of $CD63^+$ EVs compared to normal plasma.[179] This finding indicates the potential of surface profiling as a diagnostic tool, as the presence of tumor-derived vesicles in plasma shifts the overall expression frequency of specific markers, such as CD63, in the general population.

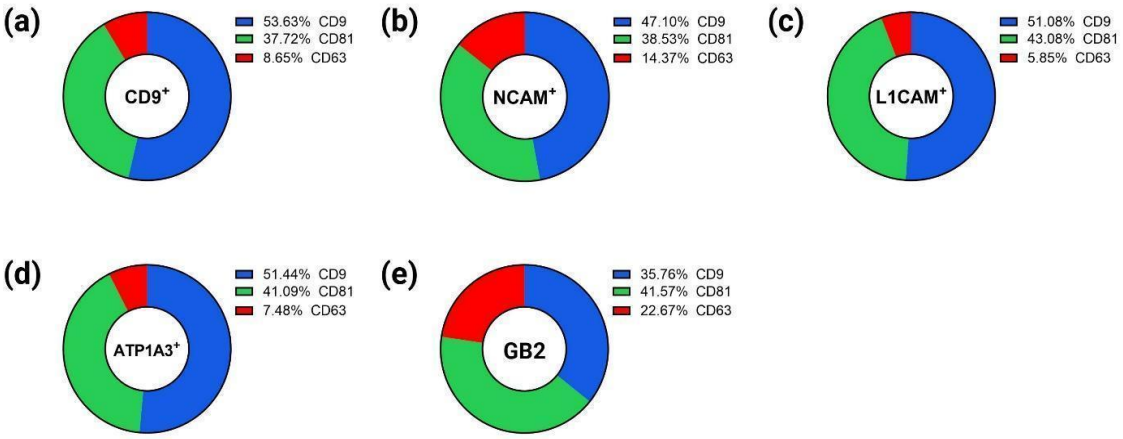

Figure 5.5 The average relative distribution of tetraspanins commonly used to identify EVs (CD9, CD63, and CD81) on normal plasma EVs isolated using (a) anti-CD9, (b) anti-NCAM, (c) anti-L1CAM, and (d) anti-ATP1A3. (n = 10 individual normal EDTA plasma samples) (e) The relative surface distribution of tetraspanins on GBM-EVs isolated using a mixture of anti-CD9, anti-CD63, and anti-CD81 affinity beads from Glioblastoma cell media (n = 2 technical repeats).

Of the three bdEV markers tested, NCAM exhibited the greatest correlation to total plasma EV concentration (Figure S5.6, $R2 = 0.7629$, $p = 0.0021$). EVs captured using anti-NCAM also exhibited greater CD63 expression (Figure S5.7, $p < 0.05$) compared to ATP1A3 and L1CAM. ATP1A3 was also found to be significantly correlated to total EV concentration (Figure S5.8, $R2 = 0.5619$, $p = 0.02$).

Total EV yield from immunoaffinity isolation (Figure 5.6E) supports the conclusion that NCAM is potentially more abundant than L1CAM and ATP1A3 in plasma. These results, along with a small subset of additional tests performed (Figures 5.S9 and S5.10), suggest that all three markers may be suitable for bdEV isolation and analysis. L1CAM was the only bdEV marker tested to not be significantly correlated to total plasma vesicle concentration. The specificity and use of L1CAM as a surface marker for bdEVs has been questioned due to claims that it is not associated with the surface of extracellular vesicles and acts more as a soluble protein in CSF and plasma.[153] Therefore, alternative markers such as NCAM and ATP1A3 are being further explored to increase specificity and yield of bdEVs from biofluids.[180]

5.4.4 Assessing bdEV Yield from Plasma

Immunoprecipitation was performed on bdEVs from 1 mL of plasma to assess the yield of the three different bdEV markers: L1CAM, NCAM, and ATP1A3. Following isolation, the concentration and size distribution of the captured EVs were analyzed using NTA (Figure 5.6). The results indicated that there was no significant difference in the concentration of EVs isolated with any of the three markers, suggesting that all three antibodies yielded a

comparable number of EVs from the starting plasma volume. The average diameter of bdEVs was larger than general plasma EVs isolated using anti-CD9 (Figure 5.6). These findings indicate that L1CAM, NCAM, and ATP1A3 are all viable targets for immunoprecipitation of brain-derived EVs from plasma with similar efficiency.

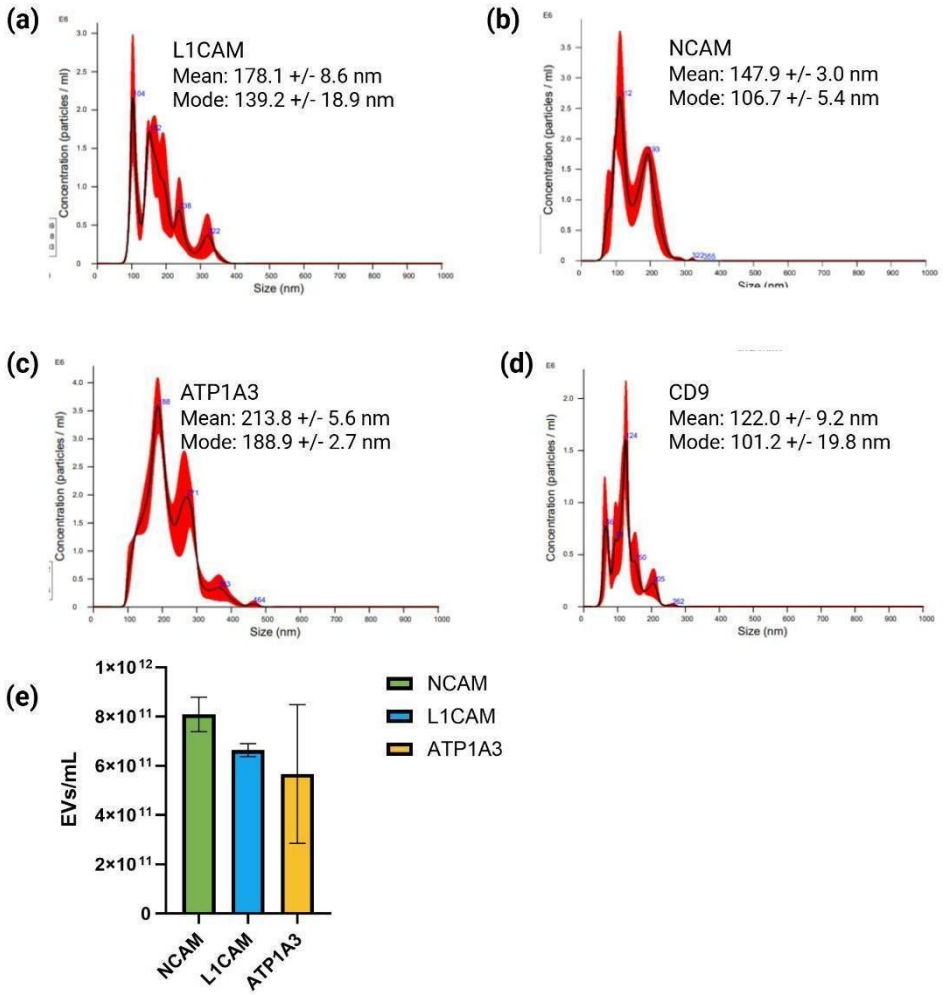

Figure 5.6 Size distribution reported by NTA for (a) anti-L1CAM, (b) anti-NCAM, (c) anti-ATP1A3, and (d) anti-CD9 isolation from 1 mL of normal EDTA plasma. (e) The reported concentration of particles from NTA (n = 3).

5.4.5 Assessing EV Loading Density

We selected Aβ-40, Aβ-42, NfL, and GFAP as our candidate markers for assessing the loading density of GM-EVs compared to normal plasma EVs. It was expected that GFAP would be highly elevated in GBM-EVs, as it is a primary cytoskeletal protein of astrocytic cells.[180] As the GBM cells grow and proliferate, they release EVs containing GFAP as part of their cargo, reflecting the cell of origin. In contrast, NfL is a neuronal protein that is not known to be produced by glioblastoma cells.[181] The presence of NfL in plasma is used as a biomarker for neuroaxonal damage. It is not known to be a direct product of glioblastoma tumor cells. Similarly, amyloid-beta, while sometimes found in the microenvironment, is not typically believed to be largely produced by glioblastoma cells.[182] Its presence is often attributed to systemic production and accumulation from sources like platelets or its role in innate immunity.[183] Therefore, GFAP stands out as a direct and specific marker of the tumor's cellular origin, making it a more abundant and reliable protein to be found within GBM-EVs.

To investigate GBM-EV protein signatures in a controlled plasma matrix while isolating the contribution of tumor-derived vesicles from baseline plasma EV cargo, we employed a spike-in experimental design in which a defined number of GBM-EVs was added to normal donor plasma. We acknowledge that this approach does not replicate the physiological context of circulating GBM-EVs in patient blood, where ongoing tumor activity, immune modulation, and systemic factors would influence the EV landscape in ways that cannot be modeled by ex-vivo spiking. These experiments are therefore intended to demonstrate

assay detection capability and proof-of-concept marker specificity rather than to directly simulate clinical conditions. EVs were isolated via immunoaffinity from 1 mL of normal EDTA plasma using either anti-CD9 or anti-NCAM antibodies. Following isolation, a small portion of EVs was used to assess total yield using the SiMoA CD9 assay. The remaining isolated EVs were lysed to assess protein yield using the Quanterix Neurology 4-Plex E assay. EVs isolated from normal EDTA plasma were found to carry all four of the proteins tested (Figure 5.7). The total yield of protein from normal plasma was also tested using L1CAM, ATP1A3, and an isotype control. Those results are shown in Figure S5.9.

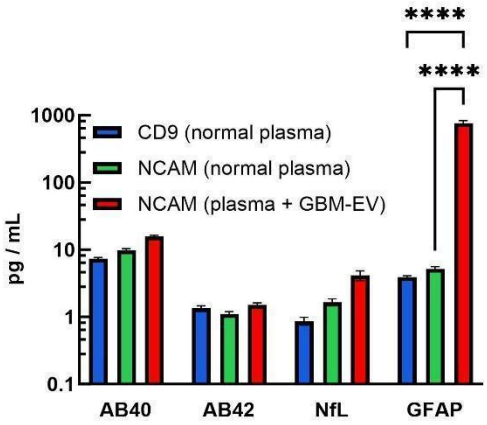

Figure 5.7 Protein yield of EVs isolated from pooled normal and GBM-EV spiked EDTA plasma (1.7×10^{10} GBM-EVs) using anti-CD9 or anti-NCAM. Soluble free protein concentrations were measured to be 14.45 pg/mL of NfL and 78.62 pg/mL of GFAP. Soluble Aβ-40 and Aβ-42 were both below the limit of quantification.

Anti-CD9 and anti-NCAM lysates from normal plasma yielded no significant difference for all analytes. In contrast, plasma spiked with GBM-EVs yielded significantly more total GFAP as predicted.

To get a more detailed view and better understanding of how these proteins are distributed amongst subpopulations of EVs, we calculated the average loading density based off of the total EV and protein yield:

$$Average\ Loading\ Density\ (\frac{pg}{EV}) = \frac{Protein\ Concentration\ (\frac{pg}{mL})}{EV\ Concentration\ (\frac{EV}{mL})} \qquad \textbf{Equation 2.}$$

The average loading density was used to estimate how many molecules of each target analyte are loaded per vesicle. It was theorized that bdEVs isolated via anti-NCAM would have a greater average loading density than the general plasma EVs isolated using anti-CD9. This was observed after calculating the average loading density based on the reported yield from the SiMoA CD9 assay (Figure 5.8a and 5.8b). Anti-NCAM isolation yielded only 10% of the total EVs as anti-CD9 (Figure 5.8b), but no significant difference in total yield (Figure 5.7). Normalizing the cargo yield revealed a higher average loading density of brain-derived proteins in bdEVs. Additionally, plasma spiked with GBM-EVs showed a significant increase in only GFAP loading. This suggests that the GBM-EVs are concentrated carriers of GFAP, but not Aβ-40, Aβ-42, or NfL.

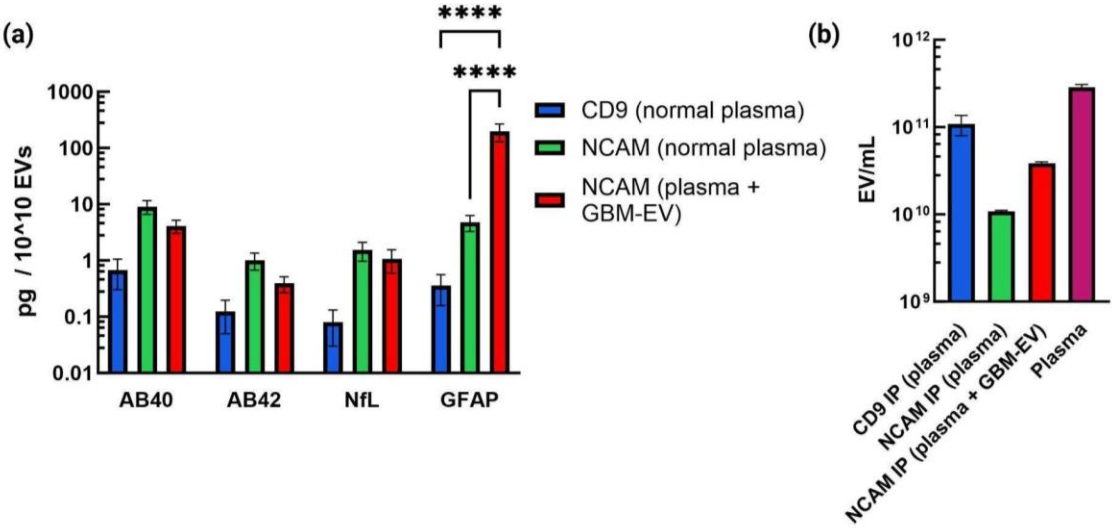

Figure 5.8 (a) Average loading density of isolated EVs based on (b) the reported EV concentration measured using the SiMoA EV CD9 assay.

The average loading density (Figure 5.8) suggests that brain-derived proteins are more concentrated in neuronal-derived EVs than general $CD9^+$ EVs. Immunoaffinity isolation targeting general EV surface markers such as CD9 can efficiently isolate most EVs in plasma, but only looking at total yield alone may not adequately represent the underlying changes in subpopulations. Analytes that are found across multiple cell types may also benefit from more specific capture strategies to better detect changes in small subpopulations and increase specificity. Future work should seek to determine the exact relationship between EV concentration and protein yield.

5.4.6 EV Surface Expression of GFAP

We also explored the use of GFAP as a candidate marker for bdEV identification. To confirm the presence of GFAP on primarily bdEVs, we compared signal produced by GFAP on EVs captured with anti-CD9 to anti-L1CAM. EVs captured with L1CAM exhibited a greater signal than $CD9^+$ EVs in a small subset of samples tested (Figure 5.9). The results of this assay confirm that GFAP is not only found primarily in neuronal EVs, but that it is localized to the surface of the vesicle alongside known bdEV markers. We also positively confirmed the colocalization of each bdEV marker (NCAM, ATP1A3, and L1CAM) on individual EVs circulating in plasma (Figure S5.10 and S5.11). The positive identification of multiple potential brain specific proteins on the surface reveals significant untapped potential for further development of assays to probe specific disease states.

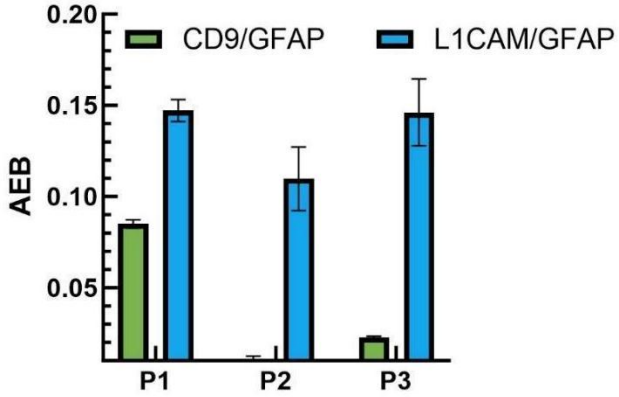

Figure 5.9 AEB values measured across three separate normal EDTA plasma samples comparing the level of GFAP expression on $CD9^+$ EVs and $L1CAM^+$ EVs.

5.5 Conclusion

This study successfully demonstrated a novel approach to isolating and characterizing bdEVs and GBM-EVs using a configurable SiMoA assay. The assay presented has applications for quantifying and phenotyping protein expression levels in EVs without the need for purification. Total plasma EV concentrations and the relative expression of CD9, CD63, and CD81 were measured across a small cohort of normal individuals. The concentration of EVs in plasma was observed to span four orders of magnitude. Similar to previous studies using different methodologies, CD9 was the most expressed protein on the surface followed by CD81 and CD63, respectively.[182] This highlights the importance of utilizing a platform with analog and digital capabilities like the SiMoA platform to capture wide ranges of analyte concentrations. Traditional plate-based ELISAs used for EV quantification lack the sensitivity to measure the presence of unpurified EVs, especially at low concentrations. By measuring the presence of EVs without purification, the assay may provide a more accurate assessment of biomarker distribution across EVs in their

natural state. Techniques used for EV enrichment and purification are known to inherently induce bias by affecting yield and integrity.[183]

Our findings also confirmed that three distinct neuronal markers—NCAM, L1CAM, and ATP1A3—yielded comparable numbers of bdEVs from normal plasma, validating their use as reliable targets for isolation. EVs captured with each marker showed a similar distribution of tetraspanins on the surface. However, anti-NCAM isolation yielded an EV population with slightly increased CD63 expression in normal plasma. The concentration of bdEVs in plasma was also found to be closely linked to total EV concentration in plasma. An estimated 10% of total circulating EVs are expected to be of neuronal origin.

An innovative concept to the GBM-EV comparisons presented in this study is that the GBM-EVs were derived from primary patient cells cultured as three-dimensional spheroids in vitro, while the reference EVs were obtained from circulating plasma of healthy individuals. As we know this represents fundamentally different biological systems. The in-vitro tumor cell cultures lack the complex tumor microenvironment, systemic immune interactions, and blood-borne heterogeneity present in-vivo. Consequently, the differences observed in CD63 expression and GFAP loading between GBM-EVs and normal plasma EVs cannot be attributed exclusively to GBM pathology and may also reflect general differences between cell culture-derived and plasma-derived EVs. We encourage readers to perform further studies to compare GBM-EVs from matched patient plasma samples and healthy controls to properly attribute observed differences to disease-specific biology.

The current findings should therefore be understood as establishing baseline performance characteristics of the assay and identifying candidate markers, rather than as evidence of GBM-specific biomarker signatures.

A key finding was the differing protein expression profiles between normal bdEVs and GBM-EVs. Specifically, GBM-EVs exhibited significantly higher levels of CD63 and GFAP compared to their healthy counterparts. The increase in CD63 expression has been recorded previously in some peripheral cancers, Pairing CD63 and GFAP has potential applications for monitoring patient prognosis. This suggests that these markers could serve as a valuable signature for distinguishing tumor-derived EVs from those originating in healthy brain tissue.

Moreover, the enhanced loading density of $NCAM^+$ EVs for key neurodegenerative disease markers (Aβ40, Aβ42, NfL, and GFAP) highlights the importance of targeting specific EV subtypes to improve biomarker detection sensitivity. The ability to differentiate between healthy and tumor-derived EVs holds significant promise for the future of liquid biopsies and diagnostics. By identifying unique protein signatures, such as the increased expression of CD63 and GFAP on GBM-EVs, we can develop more precise and specific assays for detecting and monitoring central nervous system tumors.

This research establishes a foundational framework for utilizing EV surface markers to not only isolate brain-derived EVs but also to distinguish between various subtypes, such as

those originating from different cell types or disease states. Future studies could expand on this by investigating a wider range of surface markers to identify unique signatures for various tumor subtypes (e.g., astrocytomas vs. oligodendrogliomas) or even different stages of a tumor.[184] Ultimately, this approach could enable a more accurate, non-invasive method for early cancer detection, personalized treatment planning, and monitoring therapeutic response by analyzing the molecular cargo of specific EV populations.

The SiMoA-based EV phenotyping approach described here has potential relevance beyond endogenous extracellular vesicles. Biomimetic particles represent an emerging class of drug delivery and therapeutic vehicles that increasingly incorporate EV-derived surface proteins such as NCAM, CD9, and GFAP to enhance targeting specificity.[186,187] The modular immunocapture framework developed in this work, which allows flexible pairing of capture and detection antibodies, could in principle be adapted to characterize and quality-control biomimetic EV preparations, assess their surface marker loading efficiency, and compare their proteomic profiles to endogenous reference EVs. As the development of biomimetic EV therapeutics advances, standardized quantification platforms like SiMoA may provide a valuable analytical bridge between engineered particles and their biological counterparts.

5.6 Supporting Information

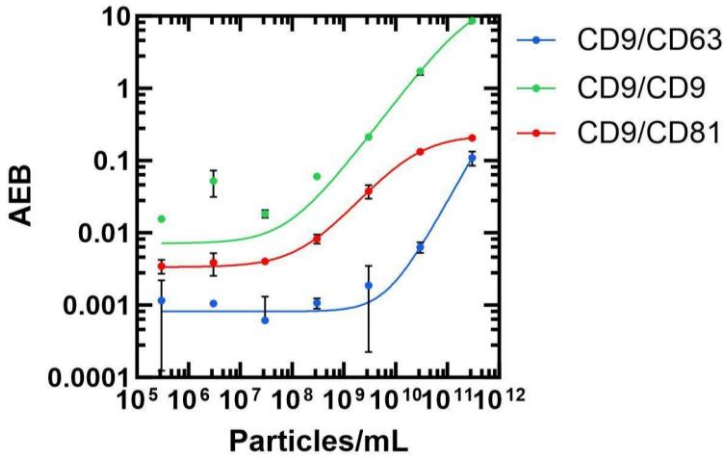

Figure S5.1 Calibration curves generated for CD9 capture and interchanging detector probes to target CD9, CD63, and CD81. EVs isolated from normal EDTA plasma via ultracentrifugation were utilized as the calibration material.

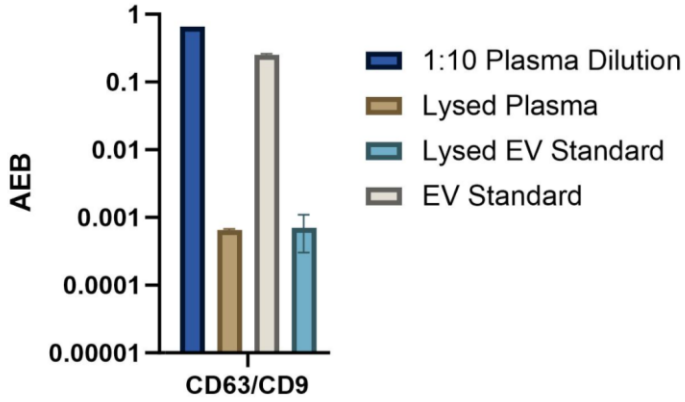

Figure S5.2 The specificity of the assay for whole EVs, and not free floating tetraspanins, was tested by comparing the signal of untreated EVs to EVs treated with 1% Triton X-100. Significant reduction in signal indicates that both CD63 and CD9 must be present on the EV for detection. No signal is observed if the EV is lysed because the sandwich complex cannot form.

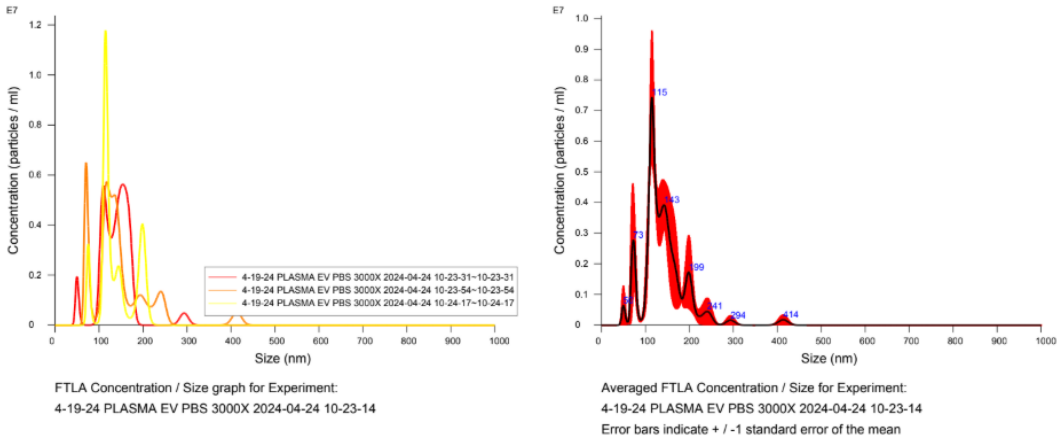

Figure S5.3 Nanoparticle tracking analysis results for normal EDTA plasma EVs isolated via ultracentrifugation. EVs were used as standards for the SiMoA EV quantification assay.

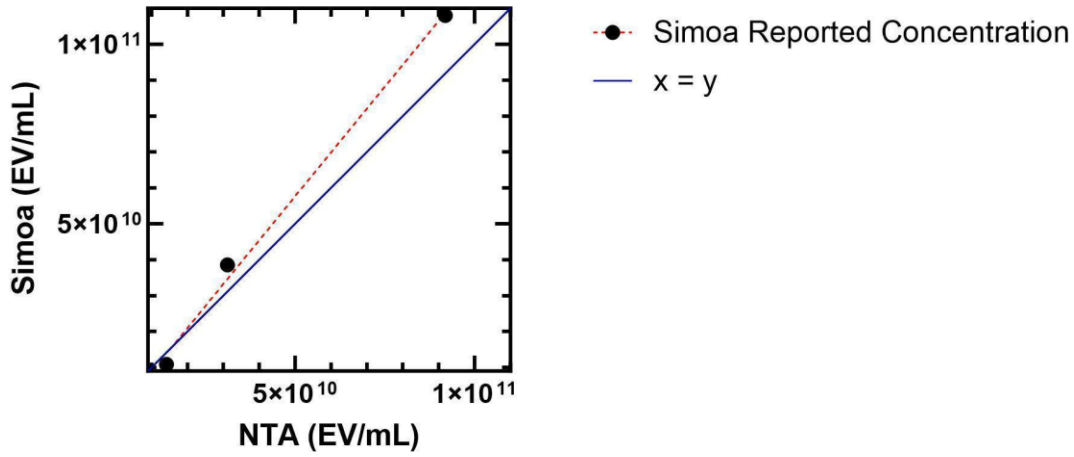

Figure S5.4 Correlation plot between reported NTA concentration and reported SiMoA concentration of 3 EV eluent samples.

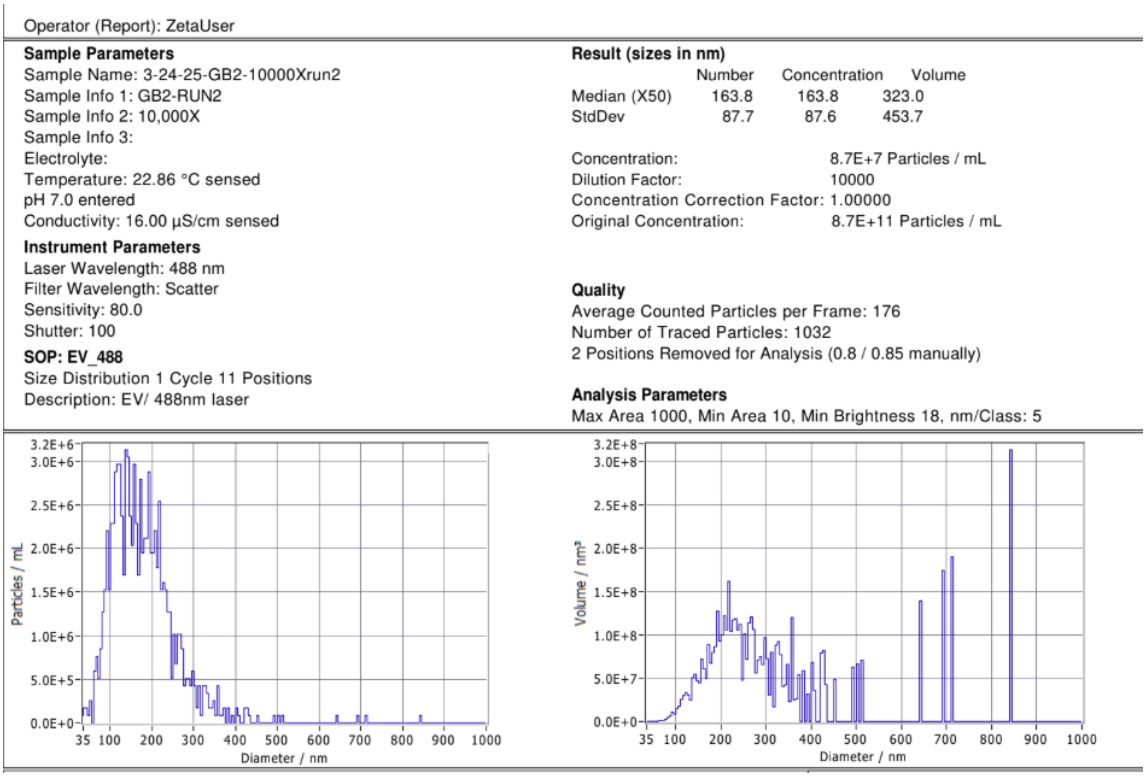

Figure S5.5 Nanoparticle tracking analysis results for glioblastoma cell conditioned media EVs isolated via ultracentrifugation. EVs were used as standards for the SiMoA EV quantification assay and spiked into normal plasma for proteomic analysis.

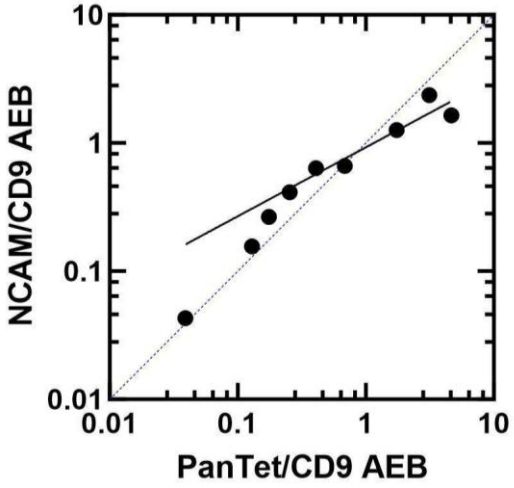

Figure S5.6 Correlation plot between PanTet/CD9 and NCAM/CD9 assay for the normal plasma cohort (n = 10). One plasma sample fell below the limit of detection for the

NCAM/CD9 configuration and is not shown. Analysis was done using the correlation function on GraphPad version 10.0.2.

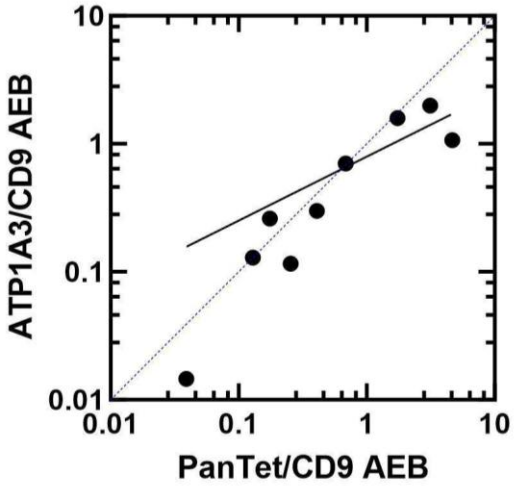

Figure S5.7 Correlation plot between PanTet/CD9 and ATP1A3/CD9 assay for the normal plasma cohort (n = 10). One plasma sample fell below the limit of detection for the ATP1A3/CD9 configuration and is not shown. Analysis was done using the correlation function on GraphPad version 10.0.2.

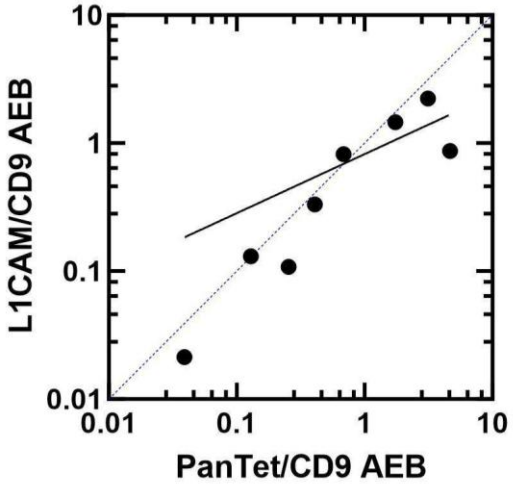

Figure S5.8 Correlation plot between PanTet/CD9 and L1CAM/CD9 assay for the normal plasma cohort (n = 10). One plasma sample fell below the limit of detection for the L1CAM/CD9 configuration and is not shown. Analysis was done using the correlation function on GraphPad version 10.0.2.

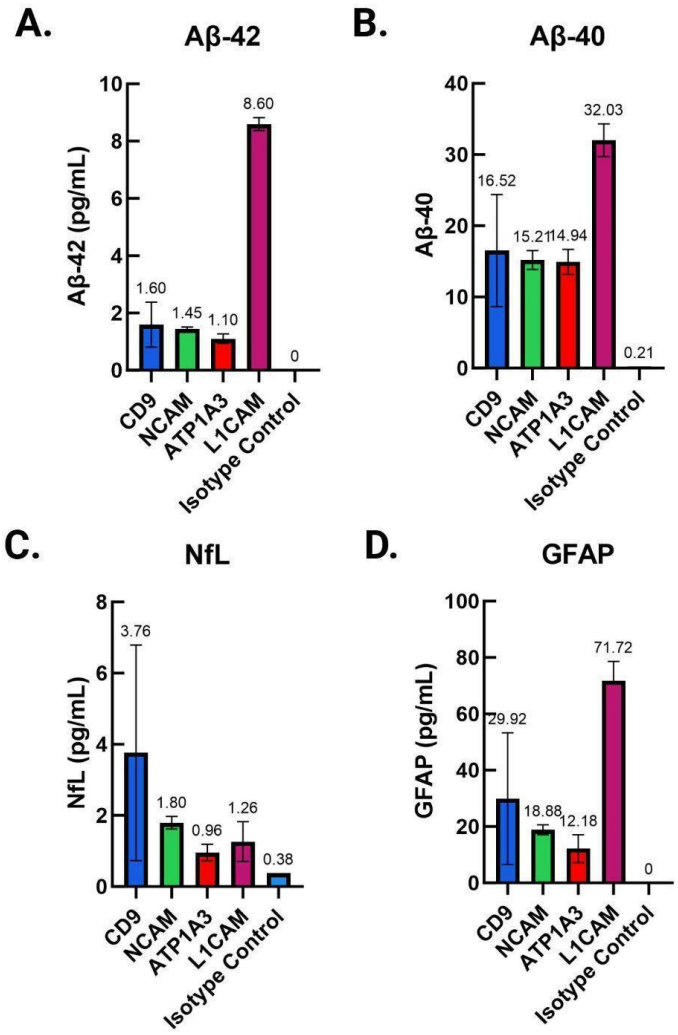

Figure S5.9 EV immunoaffinity isolation was performed on 1 mL of normal EDTA plasma using 150 µL of beads. The EVs were subsequently eluted and then lysed prior to measurement using Neurology 4-Plex E from Quanterix. The protein concentration was measured in duplicate. For the isotype control, the concentrations of both Aβ-42 and GFAP were below the limit of quantification (LOQ).

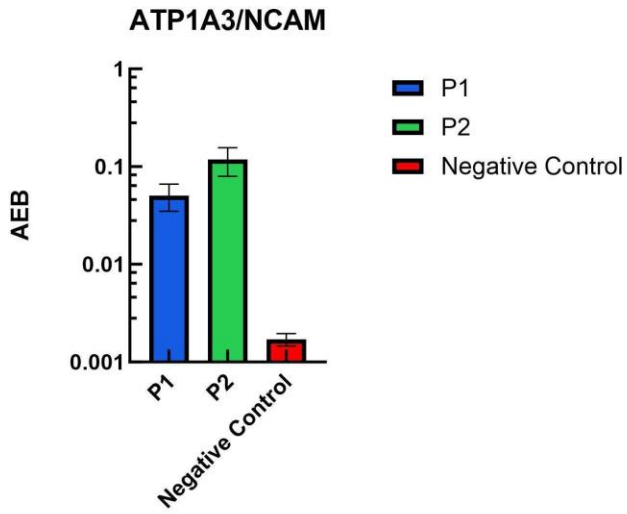

Figure S5.10 Results of testing 2X dilutions of normal EDTA plasma using anti-ATP1A3 beads as the capture and anti-NCAM as the detector. Both plasma samples tested indicated colocalization of ATP1A3 and NCAM on the surface of the vesicle.

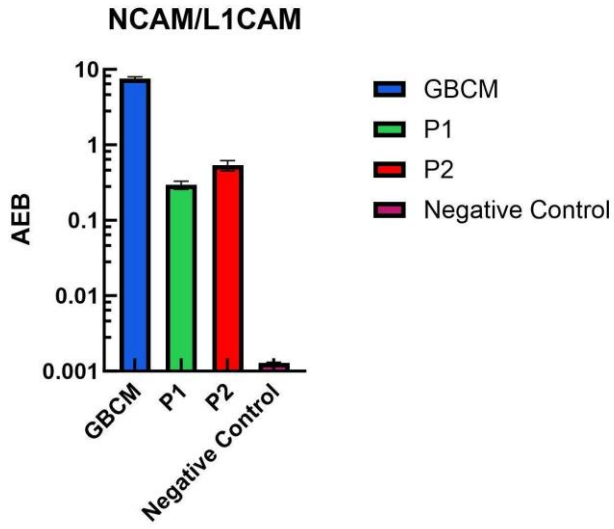

Figure S5.11 Results of testing 2X dilutions of normal EDTA plasma and glioblastoma cell media using anti-NCAM beads as the capture and anti-L1CAM as the detector. Both plasma samples tested indicated high colocalization of L1CAM and NCAM on the surface of the vesicle.

5.7 Acknowledgements

5.7.1 Funding Statement

This work was completed with funding provided in part by Quanterix Corporation, Brown University Graduate School, and the Zimmerman Innovation Award for Brain Science from the Carney Institute for Brain Science.

5.7.2 Author Contributions

J.P., A.T., M.Z., and K.M. contributed to the conceptualization, supervision, and administration of the project. J.P, C.Y., E.J., J.M., and A.F. contributed to investigation and formal analysis. J.P. and C.Y. designed methodology and contributed to the validation, curation, and visualization of the data. J.P. and A.T. acquired the funding. J.P. and A.T.. wrote the first draft. J.P., A.T., and K.M. reviewed and edited the manuscript.

The authors would also like to gratefully acknowledge Dr. Sicheng Wen and Mandy Pereira, M.S. from the COBRE Extracellular Core Facility at Brown University Health for their guidance and help with EV isolation and NTA analysis. They also thank Sarah Planchak, M.S. for her work culturing the glioblastoma spheroids and supernatant collection.

5.7.3 Conflict of Interest Statement

The authors declare that they have no competing interests. All contributions from authors associated with Quanterix are strictly scientific. The work does not aim to promote or endorse any commercial product.

CHAPTER 6:

Biomimetic Nanoparticles as Standardized Controls for Extracellular Vesicle Quantification Assays

---

Miller J., **Pollock M. J,** and Tripathi A.

1. Center for Biomedical Engineering, School of Engineering, Brown University, Providence, RI, USA

6.1 Abstract

The lack of a proper standardized reference material for extracellular vesicles (EVs) liquid biopsies has led to significant reproducibility issues within the field and has ultimately hindered the successful translation of these assays into the clinic. While naturally derived EVs offer biological relevance, they often suffer from batch-to-batch variability. The work presented here explores the development of biomimetic silica nanoparticles conjugated with recombinant CD9 protein as a robust, tunable alternative to plasma and cell media derived standards for the Single Molecular Array (SiMoA) platform. Using 100 nm carboxylated silica beads, we optimized conjugation protocols using EDC/SNHS chemistry. Results from Nanoparticle Tracking Analysis (NTA) and SiMoA indicate that the optimal coating concentration of CD9 is 0.1 mg/mL. Additionally, co-conjugating CD9 with bovine serum albumin (BSA) at 0.2 mg/mL further increases the signal-to-noise ratio of the standard and extends the total dynamic range. The use of BSA as a molecular spacer increases the monomericity of the standard to 97.7% and decreases the limit of detection to 2.0 x 10^6 particles/mL. These biomimetic silica bead standards provide a potential analytical tool for normalizing EV quantification to achieve absolute quantification - a necessary step for eventual regulatory approval.

6.2 Introduction

The exponential growth of EV research over the past decade has shifted the clinical paradigm from basic discovery towards the clinical translation of liquid biopsies for early detection of cancer and neurodegeneration. However, this translation has been bottlenecked by a lack of standardized reference materials and protocols.[44,186] Unlike

soluble protein biomarkers that can be calibrated using purified reference standards, EVs are complex, membrane-bound bioparticles characterized by significant heterogeneity in size, cargo, and surface protein density. This natural complexity creates a crisis in reproducibility across platforms and research centers. For example, there is no well-established reference material or method to directly compare the concentration reported during NTA and the SiMoA platform. A key cornerstone of completing clinical validation is the successful implementation of a clean "cut-off" value for decision making. Without clear reference material assays cannot provide absolute quantification. Thus, the development of a standardized control for EV quantification that can be used across different platforms is a requirement for the field to achieve the analytical rigor necessary for regulatory approval.

The choice of standard material for developing such a standard is critical for establishing sensitivity and specificity. Utilizing naturally derived EVs from pooled biofluids (such as plasma or serum) provides the most biologically relevant option for liquid biopsies. The primary advantage of this approach is that these EVs contain native lipid bilayers, metabolic cargo, and post-translational modifications that make them an excellent matrix-matched control to assess sensitivity and linearity. However, the greatest limitation of pooled biofluids is that they suffer from batch-to-batch variability, even when large patient pools are used. Bulk isolation methods to obtain such a standard material are also prone to co-isolating contaminates such as lipoproteins and protein aggregates. Fluctuations in baseline markers such as CD9 or CD63 will alter assay sensitivity and ultimately the reported concentration of samples.[44,162]

To address this issue, some researchers have turned to using EVs isolated from conditioned cell culture media as controls. These standards offer a more controlled environment that can be more easily scaled for large scale production of more homogeneous vesicles from a single cell line. EVs obtained from cell media offer more consistent surface marker profiles and the cells used for production can be engineered to overexpress specific markers of interest. Conversely, these EVs can also suffer from batch-to-batch variability if strict protocols are not followed and they do not possess the complex protein corona or glycosylation patterns of naturally circulating vesicles.[187-191]

To combat the biological variability presented, "biomimetic" particles (silica beads, liposomes, synthetic polymer vesicles) have emerged as potential alternatives.[193] These particles can be manufactured using strict protocols to control for size and the total amount of recombinant protein on their surface. Their stability and robustness make them a viable candidate as a precise calibrator for both size-based characterization (NTA) and surface marker quantification (immunoassays). The primary limitation of these particles is that they fail to replicate the complex behavior of natural vesicles. Due to the lack of a lipid membrane and protein corona, they may not interact with assay reagents or consumables in the same manner - which could lead to an overestimation of assay performance.

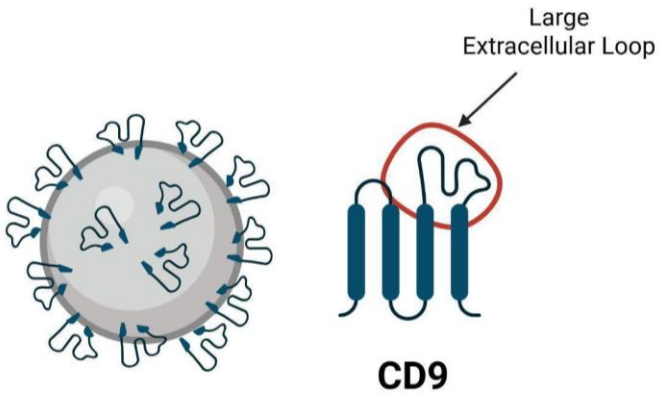

Figure 6.1 Visual representation of the biomimetic silica nanoparticles coated with recombinant CD9 protein. (Image created with Biorender.com)

In this work, we explore the development and use of biomimetic silica nanoparticles (Figure 6.1) as reference standards for the SiMoA assay to replace or accompany plasma-derived EV standard material for calibration. Silica nanoparticles are conjugated with recombinant CD9 protein, then subsequently analyzed using NTA and SiMoA. The goal is to achieve a standard that mirrors the slope and dynamic range of the assay in plasma (4-5 orders of magnitude) while maintaining low replicate variability (of both size and digital output). Silica beads were chosen for their refractive index (~1.47) that more closely mimics that of real vesicles compared to other materials, such as polystyrene(~1.59).

In long-term clinical trials, samples are often analyzed over the course of several months to years, and a stable reference allows for researchers to correct for instrument drift and reagent lot variation. A proper standard will ensure that measured concentrations over time are comparable. This normalization will help clinics establish robust cut-off values needed to monitor disease progression or therapeutic responses.

6.3 Materials and Methods

6.3.1 Silica Bead Conjugation

Particle conjugation begins by vortexing 100 nm carboxyl silica nanoparticle (DiagNano^{TM}, Cat#: DNG-F050) for 30 seconds to resuspend the particles homogeneously. Next, 250 µL of particles are aliquoted into 2 mL protein lo-bind tubes. Add 250 µL of 0.4 mg/mL EDC and 4 mg/mL of SNHS dissolved in MES Buffer (pH = 5.0). Mix thoroughly and then incubate with over-end mixing for 30 minutes at 4℃ to activate the carboxyl surface.

While the beads are incubating, prepare the protein coating solution by mixing 1 mg/mL of CD9 in 1X PBS (SinoBiological Cat#11029-H08H) with Bead Conjugation Buffer (Quanterix Cat#101357) to a final volume of 300 µL. When activation is complete, centrifuge the particles for 25 minutes at 20,000 g. Carefully, remove and discard the supernatant. Resuspend the pellet with the 300 µL of prepared protein solution. Vortex the solution to ensure that all particles are properly dispersed. Incubate this mixture for 2 hours at 4℃ with over-end mixing.

After the 2-hour incubation, add 300 µL of quenching solution (20 mg/mL of BSA in 1X PBS) to the mixture and continue mixing at room temperature for 45 minutes. Following the quenching step, centrifuge the particles again for 25 minutes at 20,000 g. Remove and discard the supernatant. Finally, resuspend the pellet in 500 µL of EV sample diluent. Sonicate the samples for 30 minutes to break up any remaining aggregates. The

concentration of recombinant CD9 used during the conjugation process was titrated to determine the optimal amount.

6.3.2 Nanoparticle Tracking Analysis

All samples were diluted 1600X in PBS to a final volume of 5 ml. Camera settings were set according to the manufacturer's software manual (NanoSight NS300 User Manual, MAN0541-01-EN-00, 2017) and autofocus was adjusted to avoid indistinct particles. For each measurement, 3 30-sec videos were captured under the following conditions: cell temperature: 20°C; Syringe speed: 50 µl/s. Image analysis was completed using the built in NanoSight software.

6.3.3 SiMoA Assay

A custom 2-step assay is used on the Qunterix SR-X system to analyze the AEB produced by the silica particles. First, 25 µL of beads are added to 100 µL of the sample. Directly following, 20 µL of biotinylated detector is added. The solution is loaded onto a plate shaker and incubated for 45 minutes at 30℃ with 700 rpm shaking. Following this incubation, the magnetic assay beads are pelleted and washed prior to the addition of 100 µL of SβG. The solution is incubated for another 10 minutes on the plate shaker at 30℃ with 700 rpm shaking. Lastly, the bead pellet is washed again and left to air dry for 10 minutes prior to loading onto the SR-X system.

6.4 Results and Discussion

The initial physical characteristics of the silica scaffold were established using NTA to confirm that the starting materials maintained a narrow, monodisperse size distribution

prior to conjugation. Following the EDC/SNHS activation and protein conjugation, the NTA measurements revealed increasing average diameters and increasing polydispersity with respect to the concentration of recombinant CD9 used for conjugation (Figure 6.2). The diameter of the unconjugated stock beads measured 77.4 nm and had a monomericity percentage of 98.6% (Figure 6.2D). Monomericity for this work was defined as the fraction of particles less than 150 nm in diameter (i.e. particles whose size is less than the equivalent of 2 beads). Large size distributions of particles less than 150 nm in diameter are indicators of high protein aggregation, but low bead aggregation. At high concentrations of CD9, the rate of irreversible bead aggregation increased significantly. This resulted in a poor standard curve with high background noise (Figure 6.2E). At low protein concentration, the bead remains monomeric and the size increase is most likely due to addition of CD9 onto the surface. There are 2 primary peaks seen for the lowest concentration of CD9 (Figure 6.2A). The first peak is around 70 nm, the baseline unconjugated diameter, and the second is around 100 nm. The second peak indicates that there is a significant population of beads that were successfully conjugated with protein. However, there is also still a significant population of beads that likely did not get any or much protein added. Figure 6.2B also has 2 large peaks that are shifted more to the right. The average diameter of this condition (0.1 mg/mL CD9) is 116.8 nm and this is around the location of the first peak. The second peak appears at 160nm. This second peak indicates that there are some bead aggregates present - thus the lower monomericity. This coating concentration was observed to have the best signal-noise-ratio of the conditions tested with a limit of detection of 1.0 x 10^8 particles/mL. It was chosen as the concentration to use moving forward.

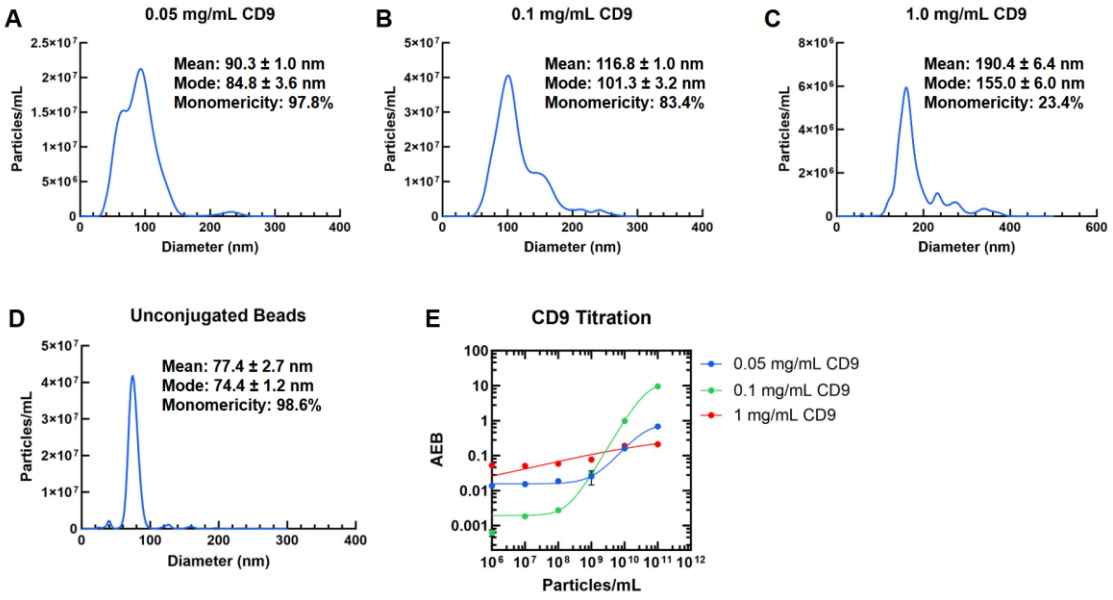

Figure 6.2 The concentration of recombinant CD9 used during the conjugation process was titrated to determine the optimal amount. (A - C) Are the size distributions of the resulting particles as measured by NTA. (D) Is the NTA measurement of the unconjugated stock silica particles. (E) The standard curves produced using the CD9 capture and detection SiMoA assay for the silica beads coated with recombinant CD9.

We also chose to co-conjugate the particles with BSA in order to further optimize the signal-to-noise ratio, increase stability, and potentially mimic the protein corona of natural EVs more closely. The optimal BSA co-conjugation concentration was determined to be 0.2 mg/mL (Figure 6.3A). This resulted in the highest signal-to-noise ratio and best monomericity (97.7%). The addition of BSA as a co-conjugate increased the monomericity by 14%. Conversely, the highest concentration of BSA reduced the overall monomericity to 86.0% and suppressed the CD9 signal observed by SiMoA. Both 0.2 mg/mL and 10 mg/mL of BSA produced similar AEB values using the CD9 capture and detection assay. Overall, the silica particles when co-conjugated with CD9 and BSA were more monomeric and capable of producing a standard curve that spans over five orders of magnitude with

an LOD of 2.0 x 10^6 particles/mL. This work suggests that these biomimetic nanoparticles are good candidates as a stable and robust alternative to natural EVs for assay standardization.

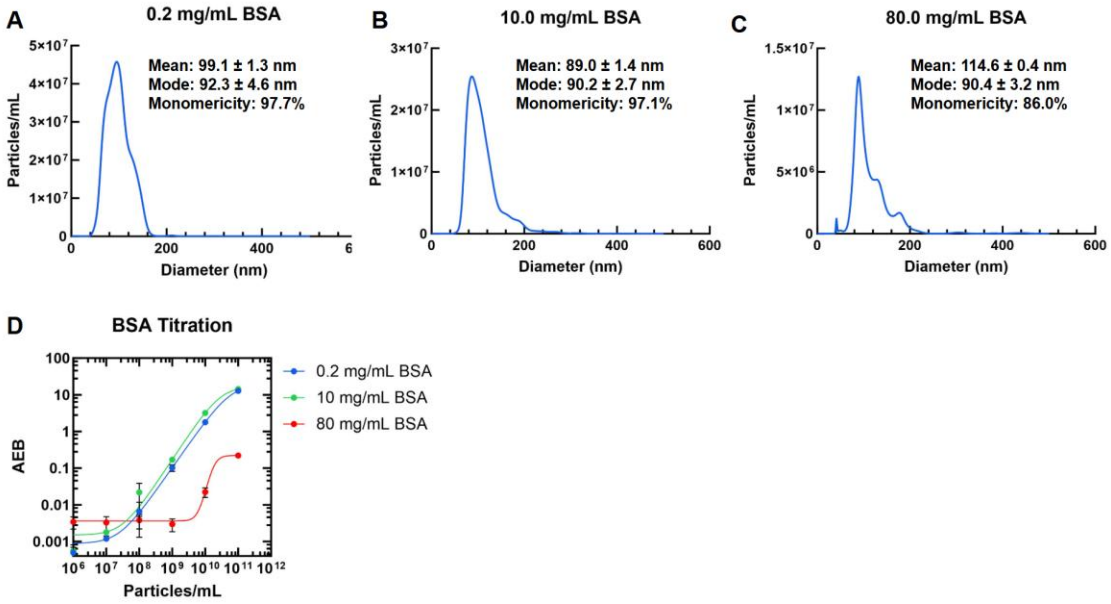

Figure 6.3 The concentration of bovine serum albumin (BSA) used during the CD9 conjugation process was titrated to determine the optimal amount. (A-C) The size distributions of particles co-conjugated with BSA and recombinant CD9 protein as measured using NTA. (D) The standard curves produced using the CD9 capture and detection SiMoA assay for the conjugated silica beads.

6.5 Conclusion

The development of the CD9-conjugated silica nanoparticles presents a significant step towards a solution to the reproducibility issue that hinders the clinical translation of EV liquid biopsies. It addresses the primary need for a standard analytical tool to bridge the quantification gap between different platforms. Unlike naturally derived EVs that suffer from inherent biological heterogeneity, these particles offer a robust, tunable, and highly reproducible alternative. The concentration of both co-conjugates, CD9 and BSA, were

optimized to maximize the signal-to-noise ratio produced by the assay and minimize bead aggregation. The optimal CD9 concentration was determined to be 0.1 mg/mL and similarly the optimal BSA concentration was 0.2 mg/mL. At these concentrations the particles produced a standard curve that spanned five orders of magnitude and had an LOD of 2.0×10^6 particles/mL. The presence of BSA served a dual purpose - it acted as a potent quenching agent to eliminate any open binding regions that remained post conjugation and it functioned as a molecular spacer to increase bead monomericity. The performance of these silica nanoparticles meets the expected sensitivity required for analyzing clinical plasma samples, suggesting that these particles can accurately simulate the analytical behavior of natural EVs while providing the stability necessary for instrument normalization and reagent lot-to-lot calibration.

Ultimately, the successful implementation of these CD9-BSA silica nanoparticles provides a foundational framework for the standardization of EV-based diagnostic platforms. As the field moves toward regulatory approval for cancer and neurodegeneration screening, the ability to report absolute concentrations rather than arbitrary units will be essential. These biomimetic standards provide the necessary rigor to establish inter-platform comparability, allowing researchers to harmonize data produced across multiple platforms and timepoints.

6.6 Acknowledgements

6.6.1 Author Contributions

J.M., J.P., and A.T. contributed to the conceptualization, supervision, and administration of the project. J.P and J.M. contributed to the investigation and formal analysis. J.P. and J.M. designed methodology and contributed to the validation, curation, and visualization of the data. A.T. acquired the funding. J.P. and A.T. wrote the manuscript.

CHAPTER 7:

Conclusions

7.1 Summary

This dissertation details the development of high-sensitivity analytical frameworks designed to overcome the technical limitations of traditional liquid biopsies, specifically for detecting low-abundance biomarkers like extracellular vesicles (EVs) and amyloid-beta (Aβ). To bypass the poor recovery and lack of standardization inherent in conventional isolation-based workflows, we have developed direct, digital quantification methods. This includes a dual-functionalized microparticle interface coupled with qPCR that achieved a femtomolar limit of detection for Aβ (1-42), providing a powerful tool for early Alzheimer's detection.

Furthermore, the research established a robust Single Molecule Array (SiMoA) platform for the direct detection of intact EVs in human plasma and serum. By implementing a novel mathematical model to handle EV polyvalency, the platform achieved superior sensitivity and dynamic range compared to commercial assays. Finally, the work extended into neuro-diagnostics by identifying ATP1A3 and NCAM as alternative markers for brain-derived EVs compared to L1CAM. These findings suggest that targeting specific EV subtypes, such as $NCAM^+$ populations, significantly enhances the signal-to-noise ratio for neurodegenerative biomarkers. Collectively, these scalable, isolation-free tools provide a standardized path for early disease detection and longitudinal monitoring in both oncology and neurology.

7.2 Conclusions

Chapter 7.2.1 Important Considerations for Assay Development

Assay development is the backbone of modern medicine, ecology, and biotechnology as it enables scientists and clinicians to measure critical variables throughout their research. It is the process of creating reliable and robust tools to measure chemical and biological substances. Assay development requires a meticulous balance of biochemical precision and engineering. The work discussed as part of this thesis places an emphasis on the design, optimization, and implementation of proteomic immunoassays. Chapters 2-4 focused on the development and validation of ultrasensitive immunoassays for the quantification of Aβ (1-42) and EVs in blood.

The foundation of assay sensitivity and specificity relies on the choice of capture and detector probes. In the case of proteomic assays, this often involves choosing the most effective pair of antibody clones. Clones must generally recognize distinct, non-overlapping epitopes. After clone selection, the sample buffers must be optimized to minimize non-specific binding, protect analyte stability, neutralize matrix effects, and ensure high linearity and recovery. Proper sample dilution and preparation can make or break an assay, as improper preparation increases variability and can lead to false positive or negative results. Similarly, incubation times and conditions must also be optimized to balance sensitivity and background signals. Finally, the choice of signal generation has a significant impact on the sensitivity and dynamic range of the assay. Analyte concentration can be determined via fluorescent, colorimetric, or electro-chemilumiescent readouts.

Statistical analysis (like the 4-parameter logistic curve used in this work) of these readouts allows for an accurate interpolation of signal readout to analyte concentration.

In this work we explored the challenges presented by EVs as targets for quantification. Because they are lipid-bound nanoparticles, assays must account for their size and potential polyvalency. Total EV and bdEV specific quantification assays were developed utilizing a digital ELISA platform that relies on fluorescent signal generation. The resulting work established an analytical framework for quantifying EVs in blood across four orders of magnitude with a lower limit of detection of approximately 1 x 10^7 particles/mL. The operable dynamic range of the assay is capable of capturing most naturally occurring concentrations of EVs in humans. Here we also proposed methods for quantifying EV loading density and normalizing surface marker expression in order to identify unique tetraspanin phenotypes for both breast cancer and glioblastoma-derived EVs. Future improvements upon this work would be the implementation of multiplexing in order to capture more nuances between individual vesicles.

7.2.2 Signal Amplification Strategies for Ultrasensitive Analyte Detection

Ultrasensitive detection is achieved through optimizing three key pillars: background suppression, digital compartmentalization, and high-gain signal amplification. At least one, or more, of these methods must be employed to achieve femtomolar and attamolar sensitivity. Simply increasing the brightness of the label is not always enough. Chapters 2 and 3 both place a large emphasis on signal generation for the positive detection of analytes. They explore 2 unique methods for signal generation: (1) immuno-PCR and (2) digital

compartmentalization. Both are bead-based sandwich immunoassays but rely on two different mechanisms to translate that binding event into a measurable signal. The use of immuno-PCR in chapter 2 highlights the ability of DNA amplification to increase assay sensitivity by turning a single DNA strand into millions of copies. This method falls under the pillar of high-gain signal amplification. A single binding event results in the amplification of multiple DNA strands that in return incorporate fluorescent probes during generation. This enables a 140-fold increase in sensitivity compared to a commercial plate-based ELISA using the same antibody clones. Additionally, this method is capable of single bead resolution. The qPCR readout democratizes the assay because most biological research laboratories have a qPCR machine readily available, negating the need for expensive specialized equipment. The SiMoA assays described utilizing a traditional enzymatic reaction to generate fluorescent product that is concentrated within femto-liter sized microwells. Due to the small volume of the reaction chamber, the product concentration quickly accumulates to detectable levels. Alternative amplification and signal generation strategies that can enhance the sensitivity of biomarker detection assays include proximity ligation and extension, electrochemiluminescence, and bio-barcoding. Each method has its own benefits and limitations that make them fit for different uses. In particular, the microarray makes SiMoA a reliable and robust method for absolute quantification. Methods that use DNA amplification, such as proximity ligation and extension assays, are often better suited for high-plex "fishing" studies that may rely more on relative quantification. All strategies are useful and play a specific role the target discovery to validation pipeline.

7.2.3 Benefits and Limitations of Microwell Assay Technology for EV Detection

SiMoA has established itself as the gold standard for absolute protein quantification and high-throughput target validation due to its novel digital detection logic. By isolating individual immunocomplexes within femtoliter-sized microwells, the platform is capable of detecting single enzyme labels. This has allowed for a 1000-fold increase in sensitivity compared to conventional assays. Its ability to provide an absolute, quantifiable concentration bridges the gap between discovery and clinical translation as researchers must transition from "relative" discovery data to precise, absolute concentrations (i.e. pg/mL). The small reaction chamber volume maximizes the signal-to-noise ratio to allow for highly reproducible measurements. Such precision ensures that clinical cut-off values for biomarkers can remain consistent across different patient cohorts, longitudinal studies, and across geographical barriers. However, the physical and optical constraints of the automated platform limit its use for high-plex discovery studies when compared to other assay formats (such as proximity ligation and extension). The SiMoA platform's optical system is currently limited to a maximum 4-plex capability as it uses one laser light source to excite fluorescently dyed beads and a second to excite the fluorescent product. These attributes make it best suited to bridge the gap between initial discovery and clinical diagnostic implementation. There are also some technical limitations within the context of EV assay development, such as at high EV concentrations the beads are subject to "chaining", a phenomenon in which multiple beads bind to a single vesicle. This artifact can result in false negatives and insufficient bead loading. The binding of multiple large

vesicles may also sterically hinder proper bead loading into the microwells. Lastly, SiMoA's inability to multi-plex detectors (as it only uses a 488 nm laser for signal excitation) also reduces its ability to distinguish between different antibody detectors that may bind the different epitopes on the vesicle. Thus, for EV research capture and detector pairs must be carefully chosen.

7.3 Future Directions

During the development and implementation of these assays, even more novel and potential applications were revealed. Numerous other directions could be explored utilizing the assays presented here in combination with other biomarkers to further increase their clinical utility.

7.3.1 Multiplex Assay Development

This work focused on developing and validating single-plex EV detection assays for general EV and bdEV specific quantification. Future work would benefit from the development of multiplex panels to quantify multiple distinct EV subpopulations within a sample. Potential examples include combining CD44 and CD133 to develop targeted panels to identify aggressive-resistant tumor cells and evaluate the potential for recurrence. Another extremely powerful panel for identifying breast cancer would be a 4-plex assay using CD44, MUC1, EpCAM, and HER2 for capture and CD63 for detection as this would help to capture different molecular subtypes and metastatic potential. Additionally, neurology panels that look at the ratio of CNS specific EVs compared to the total population may also be useful for monitoring overall neurological health. Overall,

multiplex panels utilizing the markers presented in this work and others would enable researchers to further elucidate unique molecular fingerprints via liquid biopsies to improve future patient outcomes.

7.3.2 A Targeted Direct Comparison of Plasma and CSF EV Composition

Due to their ability to bypass the blood-brain-barrier, there is significant interest in directly comparing the cargo and general presentation of bdEVs in plasma and CSF. As CSF is a direct "window" into the brain, it is the best source for CNS derived EVs. In contrast, CNS derived EVs make up a much smaller percentage of total EVs circulating in peripheral blood. A direct comparison of EVs and their associated cargo between these two biofluids will help to evaluate how efficiently the blood-brain-barrier filters EVs and other molecules. In particular, a direct comparison of how the AT(N)I framework changes from CSF to plasma would help researchers to better understand how the brain clears plaques and other "trash" from the brain.

7.3.3 Co-conjugating Tetraspanins and other Molecules to Biomimetic Nanoparticles

Due to the promising results shown in Chapter 6, further work should be done to continue to develop biomimetic standards for assay standardization, as these standards provide the necessary rigor to establish platform comparability. In particular, further work should be done to co-conjugate multiple tetraspanins (CD63 and CD81) and other surface markers (NCAM, ATP1A3, CD44, etc) to the surface to produce additional standards that can be used for quantifying specific EV subpopulations. The expansion of this modular

conjugation strategy would solidify the role of synthetic mimics as a good alternative to naturally derived EVs. Long term stability studies should also be performed to determine the best storage practices.

7.3.4 Integration of Machine Learning for Predictive Diagnostic Modeling

As multiplex digital assays generate increasingly complex, high-dimensional multi-omic datasets, future frameworks should integrate machine learning algorithms to identify non-linear diagnostic signatures. Training predictive models on the relative expression levels of multiple tetraspanins (e.g., CD44, CD133, CD63) alongside CNS-specific markers will significantly enhance the prognostic capabilities of these EV-based liquid biopsies. Implementing these computational techniques alongside ultra-sensitive SiMoA quantification offers a highly scalable pathway for the precise stratification of patient populations in both oncology and neurodegenerative diseases.

7.4 Contributions of this Dissertation

7.4.1 Contributions to the scientific community

To summarize, this thesis has had multiple impacts, with the following list highlighting key contributions made to the field and scientific community:

- Developed a decentralized method for quantifying femtomolar concentrations of amyloid-beta to reduce time and cost per sample.
- Developed and validated a configurable SiMoA EV Assay for the quantification of total EVs in biofluids using CD9, CD63, and CD81.
- Assessed changes in tetraspanin phenotypes across normal and diseased populations

- Developed and validated three brain-derived EV assays for the quantification of bdEV specific subpopulations in plasma and serum.
- Compared the expression rate of three different bdEV surface markers and their associated yield of amyloid-beta, NfL, and GFAP.
- Presented a framework for isolating and analyzing the cargo of specific EV subpopulations present in normal and glioblastoma-derived EVs.

7.4.2 Contributions to the Brown Community

Additionally, during the progression of this thesis multiple contributions were made to the Brown Community and beyond:

- Presented my work and findings at numerous national and international conferences as oral and poster presentations
- Mentored and trained multiple undergraduate, master's, and Ph.D. students for research
- Won the Zimmerman Innovation Award from the Carney Institute for Brain Science to develop bdEV assays.
- Mentored students as a Teaching Assistant in ENGN 0930L and assisted students with understanding and applying the fundamentals of engineering to real life projects.
- Engaged in creating intellectual property, contributing to advancing scientific and technological innovations.
- Partnered with industry leaders to apply research findings in practical settings in order to bridge the gap between academia and industry.

- Mentored high school students outside of Brown at Burke's Martial Arts to promote discipline and hard work.

References

1. Mohr, A. E.; Ortega-Santos, C. P.; Whisner, C. M.; Klein-Seetharaman, J.; Paniz Jasbi. Navigating Challenges and Opportunities in Multi-Omics Integration for Personalized Healthcare. Biomedicines 2024, 12 (7), 1496–1496. https://doi.org/10.3390/biomedicines12071496.
2. Efstathios Iason Vlachavas; Bohn, J.; Ückert, F.; Nürnberg, S. A Detailed Catalogue of Multi-Omics Methodologies for Identification of Putative Biomarkers and Causal Molecular Networks in Translational Cancer Research. International Journal of Molecular Sciences 2021, 22 (6), 2822–2822. https://doi.org/10.3390/ijms22062822
3. Krassowski, M.; Das, V.; Sahu, S. K.; Misra, B. B. State of the Field in Multi-Omics Research: From Computational Needs to Data Mining and Sharing. Frontiers in Genetics 2020, 11. https://doi.org/10.3389/fgene.2020.610798.
4. Agache, I.; Akdis, C. A. Precision Medicine and Phenotypes, Endotypes, Genotypes, Regiotypes, and Theratypes of Allergic Diseases. Journal of Clinical Investigation 2019, 129 (4), 1493–1503. https://doi.org/10.1172/jci124611.
5. Duarte, T.; Spencer, C. Personalized Proteomics: The Future of Precision Medicine. Proteomes 2016, 4 (4), 29. https://doi.org/10.3390/proteomes4040029.
6. Alberts, B. (2017). Molecular Biology of the Cell. United States: W.W. Norton.
7. Molla, G.; Bitew, M. Revolutionizing Personalized Medicine: Synergy with Multi-Omics Data Generation, Main Hurdles, and Future Perspectives. Biomedicines 2024, 12 (12), 2750. https://doi.org/10.3390/biomedicines12122750.
8. Jiang, Y.; Wang, J.; Sun, A.; Zhang, H.; Yu, X.; Qin, W.; Ying, W.; Li, Y.; Chang, C.; Wang, X.; Xie, L.; Liu, W.; Liu, J.; Zhang, X.; Yan, Q.; Zou, Y.; Zhao, C.; Sun, H.; Zhang, J.; Su, S. The Coming Era of Proteomics-Driven Precision Medicine. National Science Review 2025. https://doi.org/10.1093/nsr/nwaf278.
9. Santos, R.; Ursu, O.; Gaulton, A.; Bento, A. P.; Donadi, R. S.; Bologa, C. G.; Karlsson, A.; Al-Lazikani, B.; Hersey, A.; Oprea, T. I.; Overington, J. P. A Comprehensive Map of Molecular Drug Targets. Nature Reviews Drug Discovery 2016, 16 (1), 19–34. https://doi.org/10.1038/nrd.2016.230.
10. Liu, T.; Altman, R. Identifying Druggable Targets by Protein Microenvironments Matching: Application to Transcription Factors. CPT: Pharmacometrics & Systems Pharmacology 2014, 3 (1), 93. https://doi.org/10.1038/psp.2013.66.

11. Yáñez-Mó, M.; Siljander, P. R.-M. .; Andreu, Z.; Bedina Zavec, A.; Borràs, F. E.; Buzas, E. I.; Buzas, K.; Casal, E.; Cappello, F.; Carvalho, J.; Colás, E.; Cordeiro-da Silva, A.; Fais, S.; Falcon-Perez, J. M.; Ghobrial, I. M.; Giebel, B.; Gimona, M.; Graner, M.; Gursel, I.; Gursel, M. Biological Properties of Extracellular Vesicles and Their Physiological Functions. Journal of Extracellular Vesicles 2015, 4 (1), 27066. https://doi.org/10.3402/jev.v4.27066.
12. Tran, H. L.; Zheng, W.; Issadore, D. A.; Im, H.; Cho, Y.-K.; Zhang, Y.; Liu, D.; Liu, Y.; Li, B.; Liu, F.; Tai, D.; Sun, J.; Qian, K.; He, M.; Wan, M.; Zeng, Y.; Cheng, K.; Huang, T. J.; Chiu, D. T.; Lee, L. P. Extracellular Vesicles for Clinical Diagnostics: From Bulk Measurements to Single-Vesicle Analysis. ACS Nano 2025. https://doi.org/10.1021/acsnano.5c00706.
13. Ramirez, S. H.; Andrews, A. M.; Paul, D.; Pachter, J. S. Extracellular Vesicles: Mediators and Biomarkers of Pathology along CNS Barriers. Fluids and barriers of the CNS 2018, 15 (1), 19. https://doi.org/10.1186/s12987-018-0104-7.
14. Heidrich, I.; Ačkar, L.; Mossahebi Mohammadi, P.; Pantel, K. Liquid Biopsies: Potential and Challenges. International Journal of Cancer 2020, 148 (3), 528–545. https://doi.org/10.1002/ijc.33217.
15. Nikanjam, M.; Kato, S.; Kurzrock, R. Liquid Biopsy: Current Technology and Clinical Applications. Journal of Hematology & Oncology 2022, 15 (1). https://doi.org/10.1186/s13045-022-01351-y.
16. Lianidou, E.; Pantel, K. Liquid Biopsies. Genes, Chromosomes and Cancer 2019, 58 (4), 219–232. https://doi.org/10.1002/gcc.22695.
17. Escudero, L.; Martínez-Ricarte, F.; Seoane, J. CtDNA-Based Liquid Biopsy of Cerebrospinal Fluid in Brain Cancer. Cancers 2021, 13 (9), 1989. https://doi.org/10.3390/cancers13091989.
18. Seoane, J.; Leticia De Mattos-Arruda; Émilie Le Rhun; Bardelli, A.; Weller, M. Cerebrospinal Fluid Cell-Free Tumour DNA as a Liquid Biopsy for Primary Brain Tumours and Central Nervous System Metastases. Annals of Oncology 2019, 30 (2), 211–218. https://doi.org/10.1093/annonc/mdy544.
19. Malhotra, S.; Miras, M. C. M.; Pappolla, A.; Montalban, X.; Comabella, M. Liquid Biopsy in Neurological Diseases. Cells 2023, 12 (14), 1911. https://doi.org/10.3390/cells12141911.
20. Hansson, O.; Blennow, K.; Zetterberg, H.; Dage, J. Blood Biomarkers for Alzheimer's Disease in Clinical Practice and Trials. Nature Aging 2023, 3 (5), 506–519. https://doi.org/10.1038/s43587-023-00403-3.
21. Pacoova, V.; Roveta, F.; Bonino, L.; Boschi, S.; Rainero, I.; Rubino, E. The Role of Blood-Based Biomarkers in Transforming Alzheimer's Disease Research

and Clinical Management: A Review. International Journal of Molecular Sciences 2025, 26 (17), 8564–8564. https://doi.org/10.3390/ijms26178564.

22. Mizenko, R. R.; Feaver, M.; Bozkurt, B. T.; Lowe, N.; Nguyen, B.; Huang, K.; Wang, A.; Carney, R. P. A Critical Systematic Review of Extracellular Vesicle Clinical Trials. Journal of Extracellular Vesicles 2024, 13 (10). https://doi.org/10.1002/jev2.12510.
23. De Toro, J.; Herschlik, L.; Waldner, C.; Mongini, C. Emerging Roles of Exosomes in Normal and Pathological Conditions: New Insights for Diagnosis and Therapeutic Applications. Frontiers in Immunology 2015, 6. https://doi.org/10.3389/fimmu.2015.00203.
24. Sangiliyandi Gurunathan; Min Hee Kang; Qasim, M.; Khan, K. M.; Kim, J.-H. Biogenesis, Membrane Trafficking, Functions, and next Generation Nanotherapeutics Medicine of Extracellular Vesicles. 2021, Volume 16, 3357–3383. https://doi.org/10.2147/ijn.s310357.
25. H Rashed, M.; Bayraktar, E.; K Helal, G.; Abd-Ellah, M. F.; Amero, P.; Chavez-Reyes, A.; Rodriguez-Aguayo, C. Exosomes: From Garbage Bins to Promising Therapeutic Targets. International journal of molecular sciences 2017, 18 (3), 538. https://doi.org/10.3390/ijms18030538
26. Cheng, C.; Hou, K.; Hsu, C.; Chiang, L. Ultrasensitive and High-Resolution Protein Spatially Decoding Framework for Tumor Extracellular Vesicles. Advanced Science 2023, 11 (3). https://doi.org/10.1002/advs.202304926.
27. Liu, D.; Saikam, V.; Skrada, K. A.; Merlin, D.; Iyer, S. S. Inflammatory Bowel Disease Biomarkers. Medicinal Research Reviews 2022, 42 (5), 1856–1887. https://doi.org/10.1002/med.21893.
28. Shegekar, T.; Vodithala, S.; Juganavar, A. The Emerging Role of Liquid Biopsies in Revolutionising Cancer Diagnosis and Therapy. Cureus 2023, 15 (8), e43650. https://doi.org/10.7759/cureus.43650
29. Koga, H.; Sugiyama, S.; Kugiyama, K.; Watanabe, K.; Fukushima, H.; Tanaka, T.; Sakamoto, T.; Yoshimura, M.; Jinnouchi, H.; Ogawa, H. Elevated Levels of VE-Cadherin-Positive Endothelial Microparticles in Patients with Type 2 Diabetes Mellitus and Coronary Artery Disease. Journal of the American College of Cardiology 2005, 45 (10), 1622–1630. https://doi.org/10.1016/j.jacc.2005.02.047.
30. Zhang, C.; Qin, C.; Dewanjee, S.; Bhattacharya, H.; Chakraborty, P.; Jha, N. K.; Gangopadhyay, M.; Jha, S. K.; Liu, Q. Tumor-Derived Small Extracellular Vesicles in Cancer Invasion and Metastasis: Molecular Mechanisms, and Clinical Significance. Molecular Cancer 2024, 23, 18. https://doi.org/10.1186/s12943-024-01932-0.

31. Rastogi, S.; Rani, K.; Rai, S.; Singh, R.; Prahalad Singh Bharti; Sharma, V.; Sahu, J.; Kapoor, V.; Poorvi Vishwakarma; Garg, S.; Shivajirao Lahu Gholap; Krishna Kishore Inampudi; Gyan Prakash Modi; Rani, N.; Tripathi, M.; Srivastava, A.; Rajan, R.; Fredrik Nikolajeff; Kumar, S. Fluorescence-Tagged Salivary Small Extracellular Vesicles as a Nanotool in Early Diagnosis of Parkinson's Disease. BMC medicine 2023, 21 (1). https://doi.org/10.1186/s12916-023-03031-1.
32. Francheska Delgado-Peraza; Nogueras-Ortiz, C.; Anja Hviid Simonsen; De'Larrian DeAnté Knight; Yao, P. J.; Goetzl, E. J.; Jensen, C.; Høgh, P.; Hanne Gottrup; Karsten Vestergaard; Steen Gregers Hasselbalch; Dimitrios Kapogiannis. Neuron-Derived Extracellular Vesicles in Blood Reveal Effects of Exercise in Alzheimer's Disease. Alzheimer's Research & Therapy 2023, 15 (1). https://doi.org/10.1186/s13195-023-01303-9.
33. Ding, N.; Daci, A.; Krasniqi, V.; Butler, R.; Goddard, A.; Guo, Q.; Zhang, Y.; Zhong, J.; Chan, K. L. A.; Thanou, M.; Vllasaliu, D. Engineered Extracellular Vesicles Demonstrate Altered Endocytosis and Biodistribution and Have Superior Oral SiRNA Delivery Efficiency Compared to Lipid Nanoparticles. International Journal of Pharmaceutics: X 2025, 10, 100428. https://doi.org/10.1016/j.ijpx.2025.100428.
34. El-Badawy, A.; Amer, M.; Abdelbaset, R.; Sherif, S. N.; Abo-Elela, M.; Ghallab, Y. H.; Abdelhamid, H.; Ismail, Y.; El-Badri, N. Adipose Stem Cells Display Higher Regenerative Capacities and More Adaptable Electro-Kinetic Properties Compared to Bone Marrow-Derived Mesenchymal Stromal Cells. Scientific Reports 2016, 6 (1). https://doi.org/10.1038/srep37801.
35. Zou, Y.; Zhou, Y.; Li, G.; Dong, Y.; Hu, S. Clinical Applications of Extracellular Vesicles: Recent Advances and Emerging Trends. Frontiers in Bioengineering and Biotechnology 2025, 13. https://doi.org/10.3389/fbioe.2025.1671963.
36. Rudge, C.; McClelland, R.; Chrzanowski, W.; Davis, R. L. The Regulatory Landscape for Extracellular Vesicle Therapies: Australian Context and Future Directions. Extracellular Vesicles and Circulating Nucleic Acids 2026, 7 (1), 292–301. https://doi.org/10.20517/evcna.2025.129.
37. Wang, Y.; Zhu, J.; Ma, Q.; Zhou, W.; Yang, L.; Sheng, S.; Zhu, F.; Xia, Z. Trends in Mesenchymal Stem Cell-Derived Extracellular Vesicles Clinical Trials 2014–2024: Is Efficacy Optimal in a Narrow Dose Range? Frontiers in Medicine 2025, 12. https://doi.org/10.3389/fmed.2025.1625787.
38. Xu, G.; Jin, J.; Fu, Z.; Wang, G.; Lei, X.; Xu, J.; Wang, J. Extracellular Vesicle-Based Drug Overview: Research Landscape, Quality Control and

Nonclinical Evaluation Strategies. Signal Transduction and Targeted Therapy 2025, 10 (1). https://doi.org/10.1038/s41392-025-02312-w.

39. Welsh, J. A.; Goberdhan, D. C. I.; O'Driscoll, L.; Buzas, E. I.; Blenkiron, C.; Bussolati, B.; Cai, H.; Di Vizio, D.; Driedonks, T. A. P.; Erdbrügger, U.; Falcon-Perez, J. M.; Fu, Q.-L.; Hill, A. F.; Lenassi, M.; Lim, S. K.; Mahoney, M. G.; Mohanty, S.; Möller, A.; Nieuwland, R.; Ochiya, T. Minimal Information for Studies of Extracellular Vesicles (MISEV2023): From Basic to Advanced Approaches. Journal of Extracellular Vesicles 2024, 13 (2), e12404. https://doi.org/10.1002/jev2.12404.
40. Wang, Z.; Zhou, X.; Kong, Q.; He, H.; Sun, J.; Qiu, W.; Zhang, L.; Yang, M. Extracellular Vesicle Preparation and Analysis: A State-Of-The-Art Review. Advanced Science 2024, 11 (30). https://doi.org/10.1002/advs.202401069.
41. Lucchetti, D.; Battaglia, A.; Ricciardi-Tenore, C.; Colella, F.; Perelli, L.; De Maria, R.; Scambia, G.; Sgambato, A.; Fattorossi, A. Measuring Extracellular Vesicles by Conventional Flow Cytometry: Dream or Reality? International Journal of Molecular Sciences 2020, 21 (17), 6257. https://doi.org/10.3390/ijms21176257.
42. Kwon, Y.; Park, J. Methods to Analyze Extracellular Vesicles at Single Particle Level. Micro and Nano Systems Letters 2022, 10 (1). https://doi.org/10.1186/s40486-022-00156-5.
43. Vaiaki, E. M.; Falasca, M. Comparative Analysis of the Minimal Information for Studies of Extracellular Vesicles Guidelines: Advancements and Implications for Extracellular Vesicle Research. Seminars in Cancer Biology 2024, 101, 12–24. https://doi.org/10.1016/j.semcancer.2024.04.002.
44. Théry, C.; Witwer, K. W.; Aikawa, E.; Alcaraz, M. J.; Anderson, J. D.; Andriantsitohaina, R.; Antoniou, A.; Arab, T.; Archer, F.; Atkin-Smith, G. K.; Ayre, D. C.; Bach, J.-M.; Bachurski, D.; Baharvand, H.; Balaj, L.; Baldacchino, S.; Bauer, N. N.; Baxter, A. A.; Bebawy, M.; Beckham, C. Minimal Information for Studies of Extracellular Vesicles 2018 (MISEV2018): A Position Statement of the International Society for Extracellular Vesicles and Update of the MISEV2014 Guidelines. Journal of Extracellular Vesicles 2018, 7 (1), 1535750. https://doi.org/10.1080/20013078.2018.1535750.
45. Colombo, M.; Raposo, G.; Théry, C. Biogenesis, Secretion, and Intercellular Interactions of Exosomes and Other Extracellular Vesicles. Annual Review of Cell and Developmental Biology 2014, 30 (1), 255–289. https://doi.org/10.1146/annurev-cellbio-101512-122326.
46. Lucchetti, D.; Battaglia, A.; Ricciardi-Tenore, C.; Colella, F.; Perelli, L.; De Maria, R.; Scambia, G.; Sgambato, A.; Fattorossi, A. Measuring Extracellular

Vesicles by Conventional Flow Cytometry: Dream or Reality? International Journal of Molecular Sciences 2020, 21 (17), 6257. https://doi.org/10.3390/ijms21176257.
47. Kwon, Y.; Park, J. Methods to Analyze Extracellular Vesicles at Single Particle Level. Micro and Nano Systems Letters 2022, 10 (1). https://doi.org/10.1186/s40486-022-00156-5.
48. Vaiaki, E. M.; Falasca, M. Comparative Analysis of the Minimal Information for Studies of Extracellular Vesicles Guidelines: Advancements and Implications for Extracellular Vesicle Research. Seminars in Cancer Biology 2024, 101, 12–24. https://doi.org/10.1016/j.semcancer.2024.04.002.
49. Yuana, Y.; Koning, R. I.; Kuil, M. E.; Rensen, P. C. N.; Koster, A. J.; Bertina, R. M.; Osanto, S. Cryo-Electron Microscopy of Extracellular Vesicles in Fresh Plasma. Journal of Extracellular Vesicles 2013, 2 (1), 21494. https://doi.org/10.3402/jev.v2i0.21494
50. Thomas Lars Andresen. What Are We Looking At? Extracellular Vesicles, Lipoproteins, or Both? 2017, 121 (8), 920–922. https://doi.org/10.1161/circresaha.117.311767.
51. Chuo, S. T.-Y.; Chien, J. C.-Y.; Lai, C. P.-K. Imaging Extracellular Vesicles: Current and Emerging Methods. Journal of Biomedical Science 2018, 25 (1). https://doi.org/10.1186/s12929-018-0494-5.
52. Filipe, V.; Hawe, A.; Jiskoot, W. Critical Evaluation of Nanoparticle Tracking Analysis (NTA) by NanoSight for the Measurement of Nanoparticles and Protein Aggregates. Pharmaceutical Research 2010, 27 (5), 796–810. https://doi.org/10.1007/s11095-010-0073-2.
53. Gardiner, C.; Vizio, D. D.; Sahoo, S.; Théry, C.; Witwer, K. W.; Wauben, M.; Hill, A. F. Techniques Used for the Isolation and Characterization of Extracellular Vesicles: Results of a Worldwide Survey. Journal of Extracellular Vesicles 2016, 5 (1), 32945. https://doi.org/10.3402/jev.v5.32945.
54. Thamara Dayarathna; Roseborough, A. D.; Gomes, J.; Reza Khazaee; Carolina; Borron, K.; Yu, S.; Coleman, K.; Jesso, S.; Finger, E.; MacDonald, P.; Borrie, M.; Wells, J.; Bartha, R.; Zou, G.; Whitehead, S. N.; Leong, H. S.; Pasternak, S. H. Nanoscale Flow Cytometry-Based Quantification of Blood-Based Extracellular Vesicle Biomarkers Distinguishes MCI and Alzheimer's Disease. Alzheimer s & Dementia 2024. https://doi.org/10.1002/alz.14087.
55. Ho, K.; Krzyzaniak, O.; Ala'a Al Hrout; Peacock, B.; Chahwan, R. Assessing Extracellular Vesicles in Human Biofluids Using Flow-Based Analyzers. Advanced Healthcare Materials 2023, 12 (32). https://doi.org/10.1002/adhm.202301706.

56. Edwin van Der Pol Detection of Extracellular Vesicles: Size Does Matter. https://www.edwinvanderpol.com/downloads/PhD_Thesis_Edwin_van_der_Pol.pdf (accessed 2026-03-31).
57. Welsh, J. A.; Holloway, J. A.; Wilkinson, J. S.; Englyst, N. A. Extracellular Vesicle Flow Cytometry Analysis and Standardization. Frontiers in Cell and Developmental Biology 2017, 5. https://doi.org/10.3389/fcell.2017.00078.
58. Rissin, D. M.; Walt, D. R. Digital Concentration Readout of Single Enzyme Molecules Using Femtoliter Arrays and Poisson Statistics. Nano letters 2006, 6 (3), 520–523. https://doi.org/10.1021/nl060227d.
59. Cohen, L.; Walt, D. R. Single-Molecule Arrays for Protein and Nucleic Acid Analysis. Annual Review of Analytical Chemistry 2017, 10 (1), 345–363. https://doi.org/10.1146/annurev-anchem-061516-045340.
60. Rissin, D. M.; Walt, D. R. Digital Readout of Target Binding with Attomole Detection Limits via Enzyme Amplification in Femtoliter Arrays. Journal of the American Chemical Society 2006, 128 (19), 6286–6287. https://doi.org/10.1021/ja058425e.
61. Dong, R.; Ning, Y.; Jiang, D. Advances in Single Molecule Arrays (SIMOA) for Ultra-Sensitive Detection of Biomolecules. Talanta 2023, 125529–125529. https://doi.org/10.1016/j.talanta.2023.125529.
62. Thompson, W. J. Poisson Distributions. Computing in Science & Engineering 2001, 3 (3), 78–82. https://doi.org/10.1109/5992.919271.
63. Zhang, J.; Wiener, A. D.; Meyer, R. E.; Kan, C. W.; Rissin, D. M.; Kolluru, B.; George, C.; Tobos, C. I.; Shan, D.; Duffy, D. C. Improving the Accuracy, Robustness, and Dynamic Range of Digital Bead Assays. Analytical Chemistry 2023, 95 (22), 8613–8620. https://doi.org/10.1021/acs.analchem.3c00918.
64. Sahrai, H.; Norouzi, A.; Hamzehzadeh, S.; Majdi, A.; Kahfi-Ghaneh, R.; Sadigh-Eteghad, S. SIMOA-Based Analysis of Plasma NFL Levels in MCI and AD Patients: A Systematic Review and Meta-Analysis. *BMC Neurology* 2023, *23*, 331. https://doi.org/10.1186/s12883-023-03377-2.
65. Bayoumy, S.; Verberk, I. M. W.; den Dulk, B.; Hussainali, Z.; Zwan, M.; van der Flier, W. M.; Ashton, N. J.; Zetterberg, H.; Blennow, K.; Vanbrabant, J.; Stoops, E.; Vanmechelen, E.; Dage, J. L.; Teunissen, C. E. Clinical and Analytical Comparison of Six Simoa Assays for Plasma P-Tau Isoforms P-Tau181, P-Tau217, and P-Tau231. Alzheimer's Research & Therapy 2021, 13 (1). https://doi.org/10.1186/s13195-021-00939-9.
66. Schubert, S. M.; Arendt, L. M.; Zhou, W.; Baig, S.; Walter, S. R.; Buchsbaum, R. J.; Kuperwasser, C.; Walt, D. R. Ultra-Sensitive Protein Detection via Single

Molecule Arrays towards Early Stage Cancer Monitoring. Scientific Reports 2015, 5 (1). https://doi.org/10.1038/srep11034.

67. Karikari, T. K.; Pascoal, T. A.; Ashton, N. J.; Janelidze, S.; Benedet, A. L.; Rodriguez, J. L.; Chamoun, M.; Savard, M.; Kang, M. S.; Therriault, J.; Schöll, M.; Massarweh, G.; Soucy, J.-P.; Höglund, K.; Brinkmalm, G.; Mattsson, N.; Palmqvist, S.; Gauthier, S.; Stomrud, E.; Zetterberg, H. Blood Phosphorylated Tau 181 as a Biomarker for Alzheimer's Disease: A Diagnostic Performance and Prediction Modelling Study Using Data from Four Prospective Cohorts. The Lancet Neurology 2020, 19 (5), 422–433. https://doi.org/10.1016/s1474-4422(20)30071-5.
68. Pilotto, A.; Quaresima, V.; Chiara Trasciatti; Chiara Tolassi; Bertoli, D.; Mordenti, C.; Galli, A.; Rizzardi, A.; Caratozzolo, S.; Zancanaro, A.; José Contador; Hansson, O.; Palmqvist, S.; Santis, G. D.; Zetterberg, H.; Kaj Blennow; Duilio Brugnoni; Suárez-Calvet, M.; Ashton, N. J.; Padovani, A. Plasma P-Tau217 in Alzheimer's Disease: Lumipulse and ALZpath SIMOA Head-To-Head Comparison. bioRxiv (Cold Spring Harbor Laboratory) 2024. https://doi.org/10.1101/2024.05.02.24306780.
69. Zhang, Y.; Bi, K.; Zhou, L.; Wang, J.; Huang, L.; Sun, Y.; Peng, G.; Wu, W. Advances in Blood Biomarkers for Alzheimer's Disease: Ultra-Sensitive Detection Technologies and Impact on Clinical Diagnosis. Degenerative Neurological and Neuromuscular Disease 2024, Volume 14, 85–102. https://doi.org/10.2147/dnnd.s471174.
70. Kobayashi, G.; Hirata, K.; Ono, M.; Kasuga, K.; Takado, Y. The 2024 NIA-AA Biological Definition of Alzheimer's Disease: Linking Biomarkers to Clinical Practice. Frontiers in Dementia 2026, 5. https://doi.org/10.3389/frdem.2026.1736297.
71. Five markers are better than one for testing blood for signs of Alzheimer's. Nature.com. https://www.nature.com/articles/d42473-024-00129-9 (accessed 2026-03-31).
72. Wilson, D.; Khare, M.; Gallen Triana-Baltzer; Wolfe, M.; Sheehy, P.; Copeland, K.; Hesterberg, L.; Vasko, A.-J.; van; Inge; Teunissen, C. E.; Miller, M. Analytical and Clinical Validation of a High Accuracy Fully Automated Digital Immunoassay for Plasma Phospho-Tau 217 for Clinical Use in Detecting Amyloid Pathology. Frontiers in Neurology 2025, 16, 1568971–1568971. https://doi.org/10.3389/fneur.2025.1568971.
73. Xiong, X.; He, H.; Ye, Q.; Qian, S.; Zhou, S.; Feng, F.; Fang, E. F.; Xie, C. Alzheimer's Disease Diagnostic Accuracy by Fluid and Neuroimaging ATN

Framework. CNS Neuroscience & Therapeutics 2023. https://doi.org/10.1111/cns.14357.
74. Cummings, J. The National Institute on Aging-Alzheimer's Association Framework on Alzheimer's Disease: Application to Clinical Trials. Alzheimer's & Dementia 2018, 15 (1), 172–178. https://doi.org/10.1016/j.jalz.2018.05.006.
75. Yousuf, A.; Wu, X.; Bony, A. R.; Sadeghi, M.; Huang, Y.; Craik, D. J.; Adams, D. J. ⍺O-Conotoxin GeXIVA Isomers Modulate N-Type Calcium (caV2.2) Channels and Inwardly-Rectifying Potassium (GIRK) Channels via GABAB Receptor Activation. Journal of Neurochemistry 2021, 160 (2), 154–171. https://doi.org/10.1111/jnc.15535.
76. Kluge, A.; Bunk, J.; Schaeffer, E.; Drobny, A.; Xiang, W.; Knacke, H.; Bub, S.; Lückstädt, W.; Arnold, P.; Lucius, R.; Berg, D.; Zunke, F. Detection of Neuron-Derived Pathological α-Synuclein in Blood. Brain 2022, 145 (9), 3058–3071. https://doi.org/10.1093/brain/awac115.
77. Liu, R.; Yang, Y.; Hu, Z.; Fu, Y. Circulating Tumor DNA–Guided Early Detection and Minimal Residual Disease Monitoring in Pancreatic and Biliary Cancers: Evidence, Barriers, and Opportunities. World Journal of Surgical Oncology 2026, 24 (1). https://doi.org/10.1186/s12957-026-04238-1.
78. Walter, N.; Groth, J.; Zwerger, B. von und zu. Evaluation of an Innovative Multi-Cancer Early Detection Test: High Sensitivity and Specificity in Differentiating Cancer, Inflammatory Conditions, and Healthy Individuals. Frontiers in Oncology 2025, 15. https://doi.org/10.3389/fonc.2025.1520869.
79. Hoshino, A.; Kim, H. S.; Bojmar, L.; Gyan, K. E.; Cioffi, M.; Hernandez, J.; Zambirinis, C. P.; Rodrigues, G.; Molina, H.; Heissel, S.; Mark, M. T.; Steiner, L.; Benito-Martin, A.; Lucotti, S.; Di Giannatale, A.; Offer, K.; Nakajima, M.; Williams, C.; Nogués, L.; Pelissier Vatter, F. A. Extracellular Vesicle and Particle Biomarkers Define Multiple Human Cancers. Cell 2020, 182 (4), 1044-1061.e18. https://doi.org/10.1016/j.cell.2020.07.009.
80. Chen, G.; Huang, A. C.; Zhang, W.; Zhang, G.; Wu, M.; Xu, W.; Yu, Z.; Yang, J.; Wang, B.; Sun, H.; Xia, H.; Man, Q.; Zhong, W.; Antelo, L. F.; Wu, B.; Xiong, X.; Liu, X.; Guan, L.; Li, T.; Liu, S. Exosomal PD-L1 Contributes to Immunosuppression and Is Associated with Anti-PD-1 Response. Nature 2018, 560 (7718), 382–386. https://doi.org/10.1038/s41586-018-0392-8.
81. Alzheimer's Association. 2020 Alzheimer's Disease Facts and Figures. *Alzheimer's & Dementia* 2020, *16* (3), 391–460. https://doi.org/10.1002/alz.12068.
82. Jack, C. R.; Bennett, D. A.; Blennow, K.; Carrillo, M. C.; Dunn, B.; Haeberlein, S. B.; Holtzman, D. M.; Jagust, W.; Jessen, F.; Karlawish, J.; Liu, E.;

Molinuevo, J. L.; Montine, T.; Phelps, C.; Rankin, K. P.; Rowe, C. C.; Scheltens, P.; Siemers, E.; Snyder, H. M.; Sperling, R. NIA-AA Research Framework: Toward a Biological Definition of Alzheimer's Disease. *Alzheimer's & Dementia : the Journal of the Alzheimer's Association* 2018, *14* (4), 535–562. https://doi.org/10.1016/j.jalz.2018.02.018.

83. Porsteinsson, A. P.; Isaacson, R. S.; Knox, S.; Sabbagh, M. N.; Rubino, I. Diagnosis of Early Alzheimer's Disease: Clinical Practice in 2021. *The Journal of Prevention of Alzheimer's Disease* 2021, *8* (3), 1–16. https://doi.org/10.14283/jpad.2021.23.
84. Scheltens, P., de Strooper, B., Kivipelto, M., Holstege, H., Chételat, G., Teunissen, C. E., Cummings, J., & van der Flier, W. M.. Alzheimer's disease. In *The Lancet* 2021, (Vol. 397, Issue 10284, pp. 1577–1590). Elsevier B.V. https://doi.org/10.1016/S0140-6736(20)32205-4
85. Hansson, O. Biomarkers for Neurodegenerative Diseases. *Nature Medicine* 2021, *27* (6), 954–963. https://doi.org/10.1038/s41591-021-01382-x.
86. Weller, J.; Budson, A. Current Understanding of Alzheimer's Disease Diagnosis and Treatment. *F1000Research* 2018, *7* (1), 1161. https://doi.org/10.12688/f1000research.14506.1.
87. Iaccarino, L.; Burnham, S. C.; G. Dell'Agnello; Dowsett, S. A.; Epelbaum, S. Diagnostic Biomarkers of Amyloid and Tau Pathology in Alzheimer's Disease: An Overview of Tests for Clinical Practice in the United States and Europe. 2023. https://doi.org/10.14283/jpad.2023.43.
88. Hanseeuw, B. J.; Betensky, R. A.; Jacobs, H. I. L.; Schultz, A. P.; Sepulcre, J.; Becker, J. A.; Cosio, D. M. O.; Farrell, M.; Quiroz, Y. T.; Mormino, E. C.; Buckley, R. F.; Papp, K. V.; Amariglio, R. A.; Dewachter, I.; Ivanoiu, A.; Huijbers, W.; Hedden, T.; Marshall, G. A.; Chhatwal, J. P.; Rentz, D. M. Association of Amyloid and Tau with Cognition in Preclinical Alzheimer Disease: A Longitudinal Study. *JAMA neurology* 2019, *76* (8), 10.1001/jamaneurol.2019.1424. https://doi.org/10.1001/jamaneurol.2019.1424.
89. Selkoe, D. J.; Hardy, J. The Amyloid Hypothesis of Alzheimer's Disease at 25 Years. *EMBO molecular medicine* 2016, *8* (6), 595–608. https://doi.org/10.15252/emmm.201606210.
90. Hampel, H.; O'Bryant, S. E.; Molinuevo, J. L.; Zetterberg, H.; Masters, C. L.; Lista, S.; Kiddle, S. J.; Batrla, R.; Blennow, K. Blood-Based Biomarkers for Alzheimer Disease: Mapping the Road to the Clinic. *Nature Reviews Neurology* 2018, *14* (11), 639–652. https://doi.org/10.1038/s41582-018-0079-7.
91. Brand, A. L.; Lawler, P. E.; Bollinger, J. G.; Li, Y.; Schindler, S. E.; Li, M.; Lopez, S.; Ovod, V.; Nakamura, A.; Shaw, L. M.; Zetterberg, H.; Hansson, O.;

Bateman, R. J. The Performance of Plasma Amyloid Beta Measurements in Identifying Amyloid Plaques in Alzheimer's Disease: A Literature Review. *Alzheimer's Research & Therapy* 2022, *14* (1). https://doi.org/10.1186/s13195-022-01117-1.

92. Artika, I. M.; Dewi, Y. P.; Nainggolan, I. M.; Siregar, J. E.; Antonjaya, U. Real-Time Polymerase Chain Reaction: Current Techniques, Applications, and Role in COVID-19 Diagnosis. *Genes* 2022, *13* (12), 2387. https://doi.org/10.3390/genes13122387.
93. Georganopoulou, D. G.; Chang, L.; Nam, J.-M. .; Thaxton, C. S.; Mufson, E. J.; Klein, W. L.; Mirkin, C. A. From the Cover: Nanoparticle-Based Detection in Cerebral Spinal Fluid of a Soluble Pathogenic Biomarker for Alzheimer's Disease. *Proceedings of the National Academy of Sciences* 2005, *102* (7), 2273–2276. https://doi.org/10.1073/pnas.0409336102.
94. Gagni, P.; Sola, L.; Cretich, M.; Chiari, M. Development of a High-Sensitivity Immunoassay for Amyloid-Beta 1–42 Using a Silicon Microarray Platform. *Biosensors and Bioelectronics* 2013, *47*, 490–495. https://doi.org/10.1016/j.bios.2013.03.077.
95. IUPAC, Compendium of Chemical Terminology, 2nd ed. (the "Gold Book") 1997, Online corrected version: (2006–) "detection limit". doi:10.1351/goldbook.L03540
96. Li, Z.; Chen, G.-Y. Current Conjugation Methods for Immunosensors. *Nanomaterials* 2018, *8* (5), 278. https://doi.org/10.3390/nano8050278.
97. Jamerlan, A.; An, S. S. A.; Hulme, J. Advances in Amyloid Beta Oligomer Detection Applications in Alzheimer's Disease. *TrAC Trends in Analytical Chemistry* 2020, *129*, 115919. https://doi.org/10.1016/j.trac.2020.115919.
98. Xing, Y.; Xia, N. Biosensors for the Determination of Amyloid-Beta Peptides and Their Aggregates with Application to Alzheimer's Disease. *Analytical Letters* 2015, *48* (6), 879–893. https://doi.org/10.1080/00032719.2014.968925.
99. Mehta, P. D.; Patrick, B. A.; Miller, D. L.; Coyle, P. K.; Wisniewski, T. A Sensitive and Cost-Effective Chemiluminescence ELISA for Measurement of Amyloid-β 1-42 Peptide in Human Plasma. *Journal of Alzheimer's Disease* 2020, *78* (3), 1237–1244. https://doi.org/10.3233/jad-200861.
100. Wang, B.-Y.; Gu, B.-C.; Wang, G.-J.; Yang, Y.-H.; Wu, C.-C. Detection of Amyloid-β(1–42) Aggregation with a Nanostructured Electrochemical Sandwich Immunoassay Biosensor. *Frontiers in Bioengineering and Biotechnology* 2022, *10*. https://doi.org/10.3389/fbioe.2022.853947.
101. Wongta, A.; Hongsibsong, S.; Chantara, S.; Pattarawarapan, M.; Sapbamrer, R.; Sringarm, K.; Xu, Z.-L.; Wang, H. Development of an

Immunoassay for the Detection of Amyloid Beta 1-42 and Its Application in Urine Samples. *Journal of Immunology Research* 2020. https://doi.org/10.1155/2020/8821181.

102. Liu, L.; He, Q.; Zhao, F.; Xia, N.; Liu, H.; Li, S.; Liu, R.; Zhang, H. Competitive Electrochemical Immunoassay for Detection of β-Amyloid (1–42) and Total β-Amyloid Peptides Using P-Aminophenol Redox Cycling. *Biosensors and Bioelectronics* 2014, *51*, 208–212. https://doi.org/10.1016/j.bios.2013.07.047.
103. Walker, J. M.; Pollard, J. W.; Murray, E. J. *Methods in Molecular Biology*; Humana Press: Clifton, N.J., 1984.
104. Cohen, L.; Walt, D. R. Single-Molecule Arrays for Protein and Nucleic Acid Analysis. *Annual Review of Analytical Chemistry* 2017, *10* (1), 345–363. https://doi.org/10.1146/annurev-anchem-061516-045340.
105. Jennings, T. L.; Rahman, K. S.; S. Fournier-Bidoz; Chan. Effects of Microbead Surface Chemistry on DNA Loading and Hybridization Efficiency. *Analytical Chemistry* 2008, *80* (8), 2849–2856. https://doi.org/10.1021/ac7026035.
106. Calmo, R.; Alessandro Chiadò; Fiorilli, S.; Ricciardi, C. Advanced ELISA-like Biosensing Based on Ultralarge-Pore Silica Microbeads. *ACS Applied Bio Materials* 2020, *3* (9), 5787–5795. https://doi.org/10.1021/acsabm.0c00533.
107. Atkins, P.; de Paula, J. Physical Chemistry, 9th ed.; W. H. Freeman Publishers: New York. 2009.
108. Connors, K. A. Chemical Kinetics: The Study of Reaction Rates in Solution; VCH Publishers: New York. 1991.
109. Wlad Kusnezow; Syagailo, Y. V.; Igor Goychuk; Hoheisel, J. D.; Wild, D. J. Antibody Microarrays: The Crucial Impact of Mass Transport on Assay Kinetics and Sensitivity. *Expert Review of Molecular Diagnostics* 2006, *6* (1), 111–124. https://doi.org/10.1586/14737159.6.1.111.
110. Myszka, D. G. Kinetic, Equilibrium, and Thermodynamic Analysis of Macromolecular Interactions with BIACORE. *Methods in enzymology on CD-ROM/Methods in enzymology* 2000, 325–340. https://doi.org/10.1016/s0076-6879(00)23372-7.
111. Wlad Kusnezow; Syagailo, Y. V.; Sven Rüffer; Konstantin Klenin; Sebald, W.; Hoheisel, J. D.; Gauer, C.; Igor Goychuk. Kinetics of Antigen Binding to Antibody Microspots: Strong Limitation by Mass Transport to the Surface. *Proteomics* 2006, *6* (3), 794–803. https://doi.org/10.1002/pmic.200500149.

112. Liang, Y.; Lehrich, B. M.; Zheng, S.; Lu, M. Emerging Methods in Biomarker Identification for Extracellular Vesicle-Based Liquid Biopsy. Journal of Extracellular Vesicles 2021, 10 (7). https://doi.org/10.1002/jev2.12090.
113. Gorini, F.; Coada, C. A.; Monesmith, S.; Leo, A. D.; Biase, D. de; Giulia Dondi; Costanzo, S. D.; Mezzapesa, F.; Vannini, I.; Melloni, M.; Bandini, S.; Guerra, F.; Riccardo Di Corato; Pierandrea De Iaco; Patrizia Hrelia; Perrone, A. M.; Angelini, S.; Ravegnini, G. Distinctive Features of Blood- and Ascitic Fluid-Derived Extracellular Vesicles in Ovarian Cancer Patients. Molecular Medicine 2025, 31 (1), 143–143. https://doi.org/10.1186/s10020-025-01177-7.
114. Da Conceicao, A. R. R.; Marinatto, J.; Pinheiro, L. S.; Rody, T.; De Felice, F. G. The Multifaceted Role of Extracellular Vesicles in Alzheimer's Disease. Journal of Neurochemistry 2025, 169 (8). https://doi.org/10.1111/jnc.70209.
115. Webber, J.; Yeung, V.; Clayton, A. Extracellular Vesicles as Modulators of the Cancer Microenvironment. Seminars in Cell & Developmental Biology 2015, 40, 27–34. https://doi.org/10.1016/j.semcdb.2015.01.013.
116. Hiroaki Tateno; Hiemori, K.; Shimoda, A.; Akiyoshi, K.; Hiroaki Tateno. CD63-Positive Extracellular Vesicles Are Potential Diagnostic Biomarkers of Pancreatic Ductal Adenocarcinoma. 2022, 22 (1). https://doi.org/10.1186/s12876-022-02228-7.
117. Morasso, C.; Ricciardi, A.; Sproviero, D.; Truffi, M.; Albasini, S.; Piccotti, F.; Sottotetti, F.; Mollica, L.; Cereda, C.; Sorrentino, L.; Corsi, F. Fast Quantification of Extracellular Vesicles Levels in Early Breast Cancer Patients by Single Molecule Detection Array (SiMoA). Breast Cancer Research and Treatment 2021, 192 (1), 65–74. https://doi.org/10.1007/s10549-021-06474-3.
118. Konoshenko, M. Yu.; Lekchnov, E. A.; Vlassov, A. V.; Laktionov, P. P. Isolation of Extracellular Vesicles: General Methodologies and Latest Trends. BioMed Research International 2018, 2018, 1–27. https://doi.org/10.1155/2018/8545347.
119. Sidhom, K.; Obi, P. O.; Saleem, A. A Review of Exosomal Isolation Methods: Is Size Exclusion Chromatography the Best Option? International Journal of Molecular Sciences 2020, 21 (18), 6466. https://doi.org/10.3390/ijms21186466.
120. Ströhle, G.; Misra, M.; Li, H. Advancing Cancer Diagnostics: Technologies for Quantifying the Particle Concentration of Extracellular Vesicles in Complex Biological Samples. Advanced Healthcare Materials 2025, 15 (7). https://doi.org/10.1002/adhm.202503002.

121. Arab, T.; Mallick, E. R.; Huang, Y.; Dong, L.; Liao, Z.; Zhao, Z.; Olesia Gololobova; Smith, B.; Haughey, N. J.; Pienta, K. J.; Slusher, B. S.; Tarwater, P. M.; Juan Pablo Tosar; Zivkovic, A. M.; Vreeland, W. N.; Paulaitis, M. E.; Witwer, K. W. Characterization of Extracellular Vesicles and Synthetic Nanoparticles with Four Orthogonal Single-Particle Analysis Platforms. Journal of extracellular vesicles 2021, 10 (6). https://doi.org/10.1002/jev2.12079.
122. Rissin, D. M.; Kan, C. W.; Campbell, T. G.; Howes, S. C.; Fournier, D. R.; Song, L.; Piech, T.; Patel, P. P.; Chang, L.; Rivnak, A. J.; Ferrell, E. P.; Randall, J. D.; Provuncher, G. K.; Walt, D. R.; Duffy, D. C. Single-Molecule Enzyme-Linked Immunosorbent Assay Detects Serum Proteins at Subfemtomolar Concentrations. Nature Biotechnology 2010, 28 (6), 595–599. https://doi.org/10.1038/nbt.1641.
123. Rissin, D. M.; Fournier, D. R.; Piech, T.; Kan, C. W.; Campbell, T. G.; Song, L.; Chang, L.; Rivnak, A. J.; Patel, P. P.; Provuncher, G. K.; Ferrell, E. P.; Howes, S. C.; Pink, B. A.; Minnehan, K. A.; Wilson, D. H.; Duffy, D. C. Simultaneous Detection of Single Molecules and Singulated Ensembles of Molecules Enables Immunoassays with Broad Dynamic Range. Analytical Chemistry 2011, 83 (6), 2279–2285. https://doi.org/10.1021/ac103161b.
124. You, Y.; Zhang, Z.; Sultana, N.; Ericsson, M.; Martens, Y. A.; Sun, M.; Takahisa Kanekiyo; Seiko Ikezu; Shaffer, S. A.; Tsuneya Ikezu. ATP1A3 as a Target for Isolating Neuron-Specific Extracellular Vesicles from Human Brain and Biofluids. Science Advances 2023, 9 (37), eadi3647–eadi3647. https://doi.org/10.1126/sciadv.adi3647.
125. Momen-Heravi, F. Isolation of Extracellular Vesicles by Ultracentrifugation. Methods in Molecular Biology 2017, 25–32. https://doi.org/10.1007/978-1-4939-7253-1_3.
126. Thomas Lars Andresen. What Are We Looking At? Extracellular Vesicles, Lipoproteins, or Both? 2017, 121 (8), 920–922. https://doi.org/10.1161/circresaha.117.311767.
127. Gori, A.; Frigerio, R.; Gagni, P.; Jacopo Burrello; Panella, S.; Raimondi, A.; Bergamaschi, G.; Giulia Lodigiani; Romano, M.; Zendrini, A.; Radeghieri, A.; Barile, L.; Cretich, M. Addressing Heterogeneity in Direct Analysis of Extracellular Vesicles and Their Analogs by Membrane Sensing Peptides as Pan-Vesicular Affinity Probes. Advanced Science 2024, 11 (29), e2400533–e2400533. https://doi.org/10.1002/advs.202400533.
128. Jørgensen, M.; Bæk, R.; Pedersen, S.; Søndergaard, E. K. L.; Kristensen, S. R.; Varming, K. Extracellular Vesicle (EV) Array: Microarray Capturing of Exosomes and Other Extracellular Vesicles for Multiplexed Phenotyping. Journal

of Extracellular Vesicles 2013, 2 (1), 20920. https://doi.org/10.3402/jev.v2i0.20920.
129. Tominaga, N.; Hagiwara, K.; Kosaka, N.; Honma, K.; Nakagama, H.; Ochiya, T. RPN2-Mediated Glycosylation of Tetraspanin CD63 Regulates Breast Cancer Cell Malignancy. Molecular Cancer 2014, 13 (1), 134. https://doi.org/10.1186/1476-4598-13-134.
130. Saint-Pol, J.; Fenart, L. CD63, a New Therapeutical Candidate for Cholesterol Homeostasis Regulation through Extracellular Vesicles? Extracellular Vesicles and Circulating Nucleic Acids 2025, 6 (1), 166–170. https://doi.org/10.20517/evcna.2024.92.
131. Iwabuchi, E.; Miki, Y.; Xu, J.; Kanai, A.; Ishida, T.; Suzuki, T. Tetraspanins CD63 and CD81 as Potential Prognostic Biomarkers in Breast Cancer. Breast Cancer 2025, 32 (2), 393–403. https://doi.org/10.1007/s12282-025-01666-x.
132. Buzas, E. I. (2023). The roles of extracellular vesicles in the immune system. In Nature Reviews Immunology (Vol. 23, Issue 4, pp. 236–250). Nature Research. https://doi.org/10.1038/s41577-022-00763-8
133. Bano, R.; Ahmad, F.; Mohsin, M. A Perspective on the Isolation and Characterization of Extracellular Vesicles from Different Biofluids. *RSC Advances* 2021, *11* (32), 19598–19615. https://doi.org/10.1039/D1RA01576A.
134. Li, F.; Wu, L.; Feng, X.; Li, Y.; Fan, H. Extracellular Vesicles in Alzheimer's Disease: Dual Roles in Pathogenesis, Promising Avenues for Diagnosis and Therapy. Pharmaceutics 2026, 18 (1), 70. https://doi.org/10.3390/pharmaceutics18010070.
135. Wang, L.; Zhang, X.; Yang, Z.; Wang, B.; Gong, H.; Zhang, K.; Lin, Y.; Sun, M. Extracellular Vesicles: Biological Mechanisms and Emerging Therapeutic Opportunities in Neurodegenerative Diseases. Translational Neurodegeneration 2024, 13 (1). https://doi.org/10.1186/s40035-024-00453-6.
136. Alzheimer's Association. *2025 Alzheimer's Disease Facts and Figures*; 2025. https://www.alz.org/getmedia/ef8f48f9-ad36-48ea-87f9-b74034635c1e/alzheimers-facts-and-figures.pdf.
137. Kapogiannis, D.; Mustapic, M.; Shardell, M. D.; Berkowitz, S. T.; Diehl, T. C.; Spangler, R. D.; Tran, J.; Lazaropoulos, M. P.; Chawla, S.; Gulyani, S.; Eitan, E.; An, Y.; Huang, C.-W.; Oh, E. S.; Lyketsos, C. G.; Resnick, S. M.; Goetzl, E. J.; Ferrucci, L. Association of Extracellular Vesicle Biomarkers with Alzheimer Disease in the Baltimore Longitudinal Study of Aging. *JAMA Neurology* 2019, *76* (11), 1340. https://doi.org/10.1001/jamaneurol.2019.2462.

138. De Sousa, K. P.; Rossi, I.; Abdullahi, M.; Ramirez, M. I.; Stratton, D.; Inal, J. M. Isolation and Characterization of Extracellular Vesicles and Future Directions in Diagnosis and Therapy. *WIREs Nanomedicine and Nanobiotechnology* 2022. https://doi.org/10.1002/wnan.1835.
139. Eitan, E.; Thornton-Wells, T.; Elgart, K.; Erden, E.; Gershun, E.; Levine, A.; Volpert, O.; Azadeh, M.; Smith, D. G.; Kapogiannis, D. Synaptic Proteins in Neuron-Derived Extracellular Vesicles as Biomarkers for Alzheimer's Disease: Novel Methodology and Clinical Proof of Concept. Extracellular Vesicles and Circulating Nucleic Acids 2023, 4 (1), 133–150. https://doi.org/10.20517/evcna.2023.13.
140. Evtushenko, E. G.; Bagrov, D. V.; Lazarev, V. N.; Livshits, M. A.; Khomyakova, E. Adsorption of Extracellular Vesicles onto the Tube Walls during Storage in Solution. *PLOS ONE* 2020, *15* (12), e0243738. https://doi.org/10.1371/journal.pone.0243738.
141. Görgens, A.; Corso, G.; Hagey, D. W.; Jawad Wiklander, R.; Gustafsson, M. O.; Felldin, U.; Lee, Y.; Bostancioglu, R. B.; Sork, H.; Liang, X.; Zheng, W.; Mohammad, D. K.; van de Wakker, S. I.; Vader, P.; Zickler, A. M.; Mamand, D. R.; Ma, L.; Holme, M. N.; Stevens, M. M.; Wiklander, O. P. B. Identification of Storage Conditions Stabilizing Extracellular Vesicles Preparations. *Journal of Extracellular Vesicles* 2022, *11* (6). https://doi.org/10.1002/jev2.12238.
142. Kawai-Harada, Y.; Hanine El Itawi; Hiroaki Komuro; Harada, M. Evaluation of EV Storage Buffer for Efficient Preservation of Engineered Extracellular Vesicles. *International Journal of Molecular Sciences* 2023, *24* (16), 12841–12841. https://doi.org/10.3390/ijms241612841.
143. Castañeda Ruiz, A. J.; Shetab Boushehri, M. A.; Phan, T.; Carle, S.; Garidel, P.; Buske, J.; Lamprecht, A. Alternative Excipients for Protein Stabilization in Protein Therapeutics: Overcoming the Limitations of Polysorbates. *Pharmaceutics* 2022, *14* (12), 2575. https://doi.org/10.3390/pharmaceutics14122575.
144. Wachowiak, R.; Fiegel, H. C.; Kaifi, J. T.; Quaas, A.; Krickhahn, A.; Schurr, P. G.; Erttmann, R.; Schachner, M.; Kluth, D.; Sauter, G.; Izbicki, J. R. L1 Is Associated with Favorable Outcome in Neuroblastomas in Contrast to Adult Tumors. Annals of surgical oncology 2007, 14 (12), 3575–3580. https://doi.org/10.1245/s10434-007-9608-0.
145. Valentiner, U. Expression of the Neural Cell Adhesion Molecule and Polysialic Acid in Human Neuroblastoma Cell Lines. International Journal of Oncology 2011. https://doi.org/10.3892/ijo.2011.1038.

146. Welsh, J. A.; Pol, E.; Bettin, B. A.; Carter, D. R. F.; Hendrix, A.; Lenassi, M.; Langlois, M.; Llorente, A.; Nes, A. S.; Nieuwland, R.; Tang, V.; Wang, L.; Witwer, K. W.; Jones, J. C. Towards Defining Reference Materials for Measuring Extracellular Vesicle Refractive Index, Epitope Abundance, Size and Concentration. *Journal of Extracellular Vesicles* 2020, *9* (1), 1816641. https://doi.org/10.1080/20013078.2020.1816641.
147. Mustapic, M.; Eitan, E.; Werner, J. K.; Berkowitz, S. T.; Lazaropoulos, M. P.; Tran, J.; Goetzl, E. J.; Kapogiannis, D. Plasma Extracellular Vesicles Enriched for Neuronal Origin: A Potential Window into Brain Pathologic Processes. Frontiers in Neuroscience 2017, 11. https://doi.org/10.3389/fnins.2017.00278.
148. Fiandaca, M. S.; Kapogiannis, D.; Mapstone, M.; Boxer, A.; Eitan, E.; Schwartz, J. B.; Abner, E. L.; Petersen, R. C.; Federoff, H. J.; Miller, B. L.; Goetzl, E. J. Identification of Preclinical Alzheimer's Disease by a Profile of Pathogenic Proteins in Neurally Derived Blood Exosomes: A Case-Control Study. *Alzheimer's & Dementia* 2014, *11* (6), 600-607.e1. https://doi.org/10.1016/j.jalz.2014.06.008.
149. Nogueras-Ortiz, C. J.; Eren, E.; Yao, P.; Calzada, E.; Dunn, C.; Volpert, O.; Francheska Delgado-Peraza; Maja Mustapic; Alexey Lyashkov; Rubio, F. J.; Vreones, M.; Cheng, L.; You, Y.; Hill, A. F.; Tsuneya Ikezu; Erez Eitan; Goetzl, E. J.; Dimitrios Kapogiannis. Single-Extracellular Vesicle (EV) Analyses Validate the Use of L1 Cell Adhesion Molecule (L1CAM) as a Reliable Biomarker of Neuron-Derived EVs. *Journal of Extracellular Vesicles* 2024, *13* (6). https://doi.org/10.1002/jev2.12459.
150. Little, T. Method Validation Essentials, Limit of Blank, Limit of Detection, and Limit of Quantitation. BioPharm International 2015, 28 (4).
151. Norman, M.; Ter-Ovanesyan, D.; Trieu, W.; Lazarovits, R.; Kowal, E. J. K.; Lee, J. H.; Chen-Plotkin, A. S.; Regev, A.; Church, G. M.; Walt, D. R. L1CAM Is Not Associated with Extracellular Vesicles in Human Cerebrospinal Fluid or Plasma. *Nature Methods* 2021, *18* (6), 631–634. https://doi.org/10.1038/s41592-021-01174-8.
152. Angiolini, F.; Belloni, E.; Giordano, M.; Campioni, M.; Forneris, F.; Paronetto, M. P.; Lupia, M.; Brandas, C.; Pradella, D.; Di Matteo, A.; Giampietro, C.; Jodice, G.; Luise, C.; Bertalot, G.; Freddi, S.; Malinverno, M.; Irimia, M.; Moulton, J. D.; Summerton, J.; Chiapparino, A. A Novel L1CAM Isoform with Angiogenic Activity Generated by NOVA2-Mediated Alternative Splicing. eLife 2019, 8. https://doi.org/10.7554/elife.44305.
153. Balestrini, S.; Mikati, M. A.; Álvarez-García-Rovés, R.; Carboni, M. P.; Arsen Hunanyan; Bassil Kherallah; McLean, M.; Prange, L.; Elisa De Grandis;

Gagliardi, A.; Pisciotta, L.; Stagnaro, M.; Edvige Veneselli; Jaume Campistol; Fons, C.; Pías-Peleteiro, L.; Brashear, A.; Miller, C.; Samões, R.; Vesna Branković. Cardiac Phenotype in *ATP1A3*-Related Syndromes. *Neurology* 2020, *95* (21), e2866–e2879. https://doi.org/10.1212/wnl.0000000000010794.

154. György, B., Szabó, T. G., Pásztói, M., Pál, Z., Misják, P., Aradi, B., László, V., Pállinger, É., Pap, E., Kittel, Á., Nagy, G., Falus, A., & Buzás, E. I. (2011). Membrane vesicles, current state-of-the-art: Emerging role of extracellular vesicles. In Cellular and Molecular Life Sciences (Vol. 68, Issue 16, pp. 2667–2688). https://doi.org/10.1007/s00018-011-0689-3

155. Yáñez-Mó, M., Siljander, P. R. M., Andreu, Z., Zavec, A. B., Borràs, F. E., Buzas, E. I., Buzas, K., Casal, E., Cappello, F., Carvalho, J., Colás, E., Cordeiro-Da Silva, A., Fais, S., Falcon-Perez, J. M., Ghobrial, I. M., Giebel, B., Gimona, M., Graner, M., Gursel, I., … de Wever, O. (2015). Biological properties of extracellular vesicles and their physiological functions. In Journal of Extracellular Vesicles (Vol. 4, Issue 2015, pp. 1–60). Co-Action Publishing. https://doi.org/10.3402/jev.v4.27066

156. Kodam, S. P., & Ullah, M. (2021). Diagnostic and Therapeutic Potential of Extracellular Vesicles. In Technology in Cancer Research and Treatment (Vol. 20). SAGE Publications Inc. https://doi.org/10.1177/15330338211041203

157. Carney, R. P., Mizenko, R. R., Bozkurt, B. T., Lowe, N., Henson, T., Arizzi, A., Wang, A., Tan, C., & George, S. C. (2025). Harnessing extracellular vesicle heterogeneity for diagnostic and therapeutic applications. In Nature Nanotechnology (Vol. 20, Issue 1, pp. 14–25). Nature Research. https://doi.org/10.1038/s41565-024-01774-3

158. Asleh, K., Dery, V., Taylor, C., Davey, M., Djeungoue-Petga, M. A., & Ouellette, R. J. (2023). Extracellular vesicle-based liquid biopsy biomarkers and their application in precision immuno-oncology. In Biomarker Research (Vol. 11, Issue 1). BioMed Central Ltd. https://doi.org/10.1186/s40364-023-00540-2

159. Gomes, P., Tzouanou, F., Skolariki, K., Vamvaka-Iakovou, A., Noguera-Ortiz, C., Tsirtsaki, K., Waites, C. L., Vlamos, P., Sousa, N., Costa-Silva, B., Kapogiannis, D., & Sotiropoulos, I. (2022). Extracellular vesicles and Alzheimer's disease in the novel era of Precision Medicine: implications for disease progression, diagnosis and treatment. Experimental Neurology, 358. https://doi.org/10.1016/j.expneurol.2022.114183

160. Budnik, V., Ruiz-Cañada, C., & Wendler, F. (2016). Extracellular vesicles round off communication in the nervous system. In Nature Reviews Neuroscience (Vol. 17, Issue 3, pp. 160–172). Nature Publishing Group. https://doi.org/10.1038/nrn.2015.29

161. Hill, A. F. (2019). Extracellular vesicles and neurodegenerative diseases. In Journal of Neuroscience (Vol. 39, Issue 47, pp. 9269–9273). Society for Neuroscience. https://doi.org/10.1523/JNEUROSCI.0147-18.2019
162. Ter-Ovanesyan, D., Norman, M., Lazarovits, R., Trieu, W., Lee, J.-H., Church, G. M., & Walt, D. R. (2021). Framework for rapid comparison of extracellular vesicle isolation methods. *ELife*, *10*. https://doi.org/10.7554/elife.70725
163. del Bene, M., Osti, D., Faletti, S., Beznoussenko, G. v., DiMeco, F., & Pelicci, G. (2022). Extracellular vesicles: The key for precision medicine in glioblastoma. Neuro-Oncology, 24(2), 184–196. https://doi.org/10.1093/neuonc/noab229
164. Ricklefs, F. L., Alayo, Q., Krenzlin, H., Mahmoud, A. B., Speranza, M. C., Nakashima, H., Hayes, J. L., Lee, K., Balaj, L., Passaro, C., Rooj, A. K., Krasemann, S., Carter, B. S., Chen, C. C., Steed, T., Treiber, J., Rodig, † Scott, Yang, K., Nakano, I., … Chiocca, ‡ E Antonio. (2018). C A N C E R Immune evasion mediated by PD-L1 on glioblastoma-derived extracellular vesicles. https://www.science.org
165. Stupp, R., Mason, W. P., van den Bent, M. J., Weller, M., Fisher, B., Taphoorn, M. J. B., Belanger, K., Brandes, A. A., Marosi, C., Bogdahn, U., Curschmann, J., Janzer, R. C., Ludwin, S. K., Gorlia, T., Allgeier, A., Lacombe, D., Cairncross, J. G., Eisenhauer, E., & Mirimanoff, R. O. (n.d.). Radiotherapy plus Concomitant and Adjuvant Temozolomide for Glioblastoma. www.nejm.org
166. Brown, N. F., Ottaviani, D., Tazare, J., Gregson, J., Kitchen, N., Brandner, S., Fersht, N., & Mulholland, P. (2022). Survival Outcomes and Prognostic Factors in Glioblastoma. Cancers, 14(13). https://doi.org/10.3390/cancers14133161
167. Simon, T., Jackson, E., & Giamas, G. (2020). Breaking through the glioblastoma micro-environment via extracellular vesicles. In Oncogene (Vol. 39, Issue 23, pp. 4477–4490). Springer Nature. https://doi.org/10.1038/s41388-020-1308-2
168. Skog, J., Würdinger, T., van Rijn, S., Meijer, D. H., Gainche, L., Curry, W. T., Carter, B. S., Krichevsky, A. M., & Breakefield, X. O. (2008). Glioblastoma microvesicles transport RNA and proteins that promote tumour growth and provide diagnostic biomarkers. Nature Cell Biology, 10(12), 1470–1476. https://doi.org/10.1038/ncb1800
169. Clayton, A., Mitchell, J. P., Court, J., Mason, M. D., & Tabi, Z. (2007). Human tumor-derived exosomes selectively impair lymphocyte responses to

interleukin-2. Cancer Research, 67(15), 7458–7466. https://doi.org/10.1158/0008-5472.CAN-06-3456

170. Cohen, L., Cui, N., Cai, Y., Garden, P. M., Li, X., Weitz, D. A., & Walt, D. R. (2020). Single Molecule Protein Detection with Attomolar Sensitivity Using Droplet Digital Enzyme-Linked Immunosorbent Assay. *ACS Nano*, *14*(8), 9491–9501. https://doi.org/10.1021/acsnano.0c02378

171. Wei, P., Wu, F., Kang, B., Sun, X., Heskia, F., Pachot, A., Liang, J., & Li, D. (2020). Plasma extracellular vesicles detected by Single Molecule array technology as a liquid biopsy for colorectal cancer. Journal of Extracellular Vesicles, 9(1). https://doi.org/10.1080/20013078.2020.1809765

172. Hunter, T. R., Santos, L. E., Tovar-Moll, F., & de Felice, F. G. (2025). Alzheimer's disease biomarkers and their current use in clinical research and practice. In Molecular Psychiatry (Vol. 30, Issue 1, pp. 272–284). Springer Nature. https://doi.org/10.1038/s41380-024-02709-z

173. Li, T. R., Yao, Y. X., Jiang, X. Y., Dong, Q. Y., Yu, X. F., Wang, T., Cai, Y. N., & Han, Y. (2022). β-Amyloid in blood neuronal-derived extracellular vesicles is elevated in cognitively normal adults at risk of Alzheimer's disease and predicts cerebral amyloidosis. Alzheimer's Research and Therapy, 14(1). https://doi.org/10.1186/s13195-022-01010-x

174. Ruan, Z., Pathak, D., Venkatesan Kalavai, S., Yoshii-Kitahara, A., Muraoka, S., Bhatt, N., Takamatsu-Yukawa, K., Hu, J., Wang, Y., Hersh, S., Ericsson, M., Gorantla, S., Gendelman, H. E., Kayed, R., Ikezu, S., Luebke, J. I., & Ikezu, T. (2021). Alzheimer's disease brain-derived extracellular vesicles spread tau pathology in interneurons. Brain, 144(1), 288–309. https://doi.org/10.1093/brain/awaa376

175. Odaka, H., Hiemori, K., Shimoda, A., Akiyoshi, K., & Tateno, H. (2022). CD63-positive extracellular vesicles are potential diagnostic biomarkers of pancreatic ductal adenocarcinoma. BMC Gastroenterology, 22(1). https://doi.org/10.1186/s12876-022-02228-7

176. Miki, Y., Yashiro, M., Okuno, T., Kuroda, K., Togano, S., Hirakawa, K., & Ohira, M. (2018). Clinico-pathological significance of exosome marker CD63 expression on cancer cells and stromal cells in gastric cancer. PLoS ONE, 13(9). https://doi.org/10.1371/journal.pone.0202956

177. Aaberg-Jessen, C., Sørensen, M. D., Matos, A. L. S. A., Moreira, J. M., Brünner, N., Knudsen, A., & Kristensen, B. W. (2018). Co-expression of TIMP-1 and its cell surface binding partner CD63 in glioblastomas. BMC Cancer, 18(1). https://doi.org/10.1186/s12885-018-4179-y

178. Mizenko, R. R., Brostoff, T., Rojalin, T., Koster, H. J., Swindell, H. S., Leiserowitz, G. S., Wang, A., & Carney, R. P. (2021). Tetraspanins are unevenly distributed across single extracellular vesicles and bias sensitivity to multiplexed cancer biomarkers. Journal of Nanobiotechnology, 19(1). https://doi.org/10.1186/s12951-021-00987-1
179. Huang, Y., Arab, T., Russell, A. E., Mallick, E. R., Nagaraj, R., Gizzie, E., Redding-Ochoa, J., Troncoso, J. C., Pletnikova, O., Turchinovich, A., Routenberg, D. A., & Witwer, K. W. (2023). Towards a human brain EV atlas: Characteristics of EVs from different brain regions, including small RNA and protein profiles. https://doi.org/10.1101/2023.05.06.539665
180. Middeldorp, J., & Hol, E. M. (2011). GFAP in health and disease. In Progress in Neurobiology (Vol. 93, Issue 3, pp. 421–443). https://doi.org/10.1016/j.pneurobio.2011.01.005
181. Hepner, A., Porter, J., Hare, F., Nasir, S. S., Zetterberg, H., Blennow, K., & Martin, M. G. (2019). Serum Neurofilament Light, Glial Fibrillary Acidic Protein and Tau Are Possible Serum Biomarkers for Activity of Brain Metastases and Gliomas. World Journal of Oncology, 10(4–5), 169–175. https://doi.org/10.14740/wjon1228
182. Zayas-Santiago, A., Díaz-García, A., Nuñez-Rodríguez, R., & Inyushin, M. (2020). Accumulation of amyloid beta in human glioblastomas. Clinical and Experimental Immunology, 202(3), 325–334. https://doi.org/10.1111/cei.13493
183. Fan, Y., Pionneau, C., Cocozza, F., Boëlle, P. Y., Chardonnet, S., Charrin, S., Théry, C., Zimmermann, P., & Rubinstein, E. (2023). Differential proteomics argues against a general role for CD9, CD81 or CD63 in the sorting of proteins into extracellular vesicles. *Journal of Extracellular Vesicles*, *12*(8). https://doi.org/10.1002/jev2.12352
184. Mesrati, M. H., Behrooz, A. B., Abuhamad, A. Y., & Syahir, A. (2020). Understanding glioblastoma biomarkers: Knocking a mountain with a hammer. Cells, 9(5). https://doi.org/10.3390/cells9051236
185. Nieland, L., Mahjoum, S., Grandell, E., Breyne, K., & Breakefield, X. O. (2023). Engineered EVs designed to target diseases of the CNS. Journal of Controlled Release, 356, 493–506. https://doi.org/10.1016/j.jconrel.2023.03.009
186. Chen, Y., Douanne, N., Wu, T., Kaur, I., Tsering, T., Erzingatzian, A., et al. (2025). Leveraging nature's nanocarriers: Translating insights from extracellular vesicles to biomimetic synthetic vesicles for biomedical applications. Science Advances, 11. https://doi.org/10.1126/sciadv.ads5249
187. Choi, S.-J.; Choi, J.; Kim, J.; Kim, S.-H.; Cho, H.-G.; Lim, M.-Y.; Chae, S.; Lim, K. S.; Ha, S.-J.; Kim, H.-O. Advanced Technologies in Extracellular

Vesicle Biosensing: Platforms, Standardization, and Clinical Translation. *Molecules (Basel, Switzerland)* 2026, *31* (2), 227. https://doi.org/10.3390/molecules31020227.

188. Patel, D. B.; Gray, K. M.; Santharam, Y.; Lamichhane, T. N.; Stroka, K. M.; Jay, S. M. Impact of Cell Culture Parameters on Production and Vascularization Bioactivity of Mesenchymal Stem Cell-Derived Extracellular Vesicles. *Bioengineering & Translational Medicine* 2017, *2* (2), 170–179. https://doi.org/10.1002/btm2.10065.

189. Tóth, E. Á.; Turiák, L.; Visnovitz, T.; Cserép, C.; Mázló, A.; Sódar, B. W.; Försönits, A. I.; Petővári, G.; Sebestyén, A.; Komlósi, Z.; Drahos, L.; Kittel, Á.; Nagy, G.; Bácsi, A.; Dénes, Á.; Gho, Y. S.; Szabó-Taylor, K. É.; Buzás, E. I. Formation of a Protein Corona on the Surface of Extracellular Vesicles in Blood Plasma. *Journal of Extracellular Vesicles* 2021, *10* (11). https://doi.org/10.1002/jev2.12140.

190. Dooley, K.; McConnell, R. E.; Xu, K.; Lewis, N. D.; Haupt, S.; Youniss, M. R.; Martin, S.; Sia, C. L.; McCoy, C.; Moniz, R. J.; Burenkova, O.; Sanchez-Salazar, J.; Jang, S. C.; Choi, B.; Harrison, R. A.; Houde, D.; Burzyn, D.; Leng, C.; Kirwin, K.; Ross, N. L. A Versatile Platform for Generating Engineered Extracellular Vesicles with Defined Therapeutic Properties. *Molecular Therapy* 2021, *29* (5), 1729–1743. https://doi.org/10.1016/j.ymthe.2021.01.020.

191. Watson, D. C.; Yung, B. C.; Bergamaschi, C.; Chowdhury, B.; Bear, J.; Stellas, D.; Morales-Kastresana, A.; Jones, J. C.; Felber, B. K.; Chen, X.; Pavlakis, G. N. Scalable, CGMP-Compatible Purification of Extracellular Vesicles Carrying Bioactive Human Heterodimeric IL-15/Lactadherin Complexes. *Journal of Extracellular Vesicles* 2018, *7* (1), 1442088. https://doi.org/10.1080/20013078.2018.1442088.